



Title	New cylindrical gamma-veto detector for the J-PARC KOTO experiment
Author(s)	村山, 理恵
Citation	大阪大学, 2017, 博士論文
Version Type	VoR
URL	https://doi.org/10.18910/61493
rights	
Note	

The University of Osaka Institutional Knowledge Archive : OUKA

<https://ir.library.osaka-u.ac.jp/>

The University of Osaka

New cylindrical gamma-veto detector for the J-PARC KOTO experiment

Rie MURAYAMA

Department of Physics, Graduate School of Science
Osaka University

January, 2017

Abstract

The KOTO experiment searches for new physics beyond the Standard Model that breaks the CP symmetry by observing the $K_L \rightarrow \pi^0 \nu \bar{\nu}$ decay and measuring its branching ratio. The $K_L \rightarrow \pi^0 \nu \bar{\nu}$ decay is identified by detecting only two gammas from the π^0 with a finite π^0 transverse momentum. A set of hermetic veto detectors is used to confirm that there are no other observable particles.

We developed a new cylindrical gamma veto detector called Inner Barrel to improve the overall gamma veto efficiency to further suppress background from the $K_L \rightarrow \pi^0 \pi^0$.

The Inner Barrel also aimed at good timing resolution to reduce acceptance loss due to accidental hits. The Inner Barrel is placed inside an existing cylindrical gamma veto detector called Main Barrel. We evaluated the timing resolution for both the Inner Barrel and the Main Barrel and improved analysis methods to recover acceptance.

By installing the Inner Barrel and improving the analysis for both the Inner Barrel and the Main Barrel, the $K_L \rightarrow \pi^0 \pi^0$ background was estimated to be suppressed by a factor of 3, and the total number of background events was estimated to be reduced to less than the number of signal events predicted by the Standard Model.

Contents

1	Introduction	1
1.1	CP violation in the Standard Model	1
1.2	$K_L \rightarrow \pi^0 \nu \bar{\nu}$ decay	2
1.2.1	$K_L \rightarrow \pi^0 \nu \bar{\nu}$ decay in the Standard Model	2
1.2.2	$K_L \rightarrow \pi^0 \nu \bar{\nu}$ decay beyond the Standard Model	4
1.2.3	History of $K_L \rightarrow \pi^0 \nu \bar{\nu}$ search	4
1.2.4	Techniques at the E391a experiment	6
1.3	The KOTO experiment	7
1.3.1	Improvements from E391a to the KOTO	7
1.3.2	New barrel veto detector to be added to the Main Barrel	7
1.4	Purpose and outline of this thesis	11
2	The KOTO experiment	12
2.1	Method for signal identification	12
2.1.1	Signal reconstruction	12
2.1.2	Background suppression	13
2.2	Beam line	15
2.3	Detector	17
2.3.1	CsI calorimeter	18
2.3.2	Structures and detectors near the CsI calorimeter	18
2.3.3	Front Barrel	19
2.3.4	Main Barrel	20
2.4	Readout system	23
3	Performance of the idealistic Inner Barrel	25
3.1	Simulation study method	25
3.1.1	Monte Carlo method	26
3.1.2	$K_L \rightarrow \pi^0 \pi^0$ simulation	27
3.1.3	Monochromatic gamma simulation	29
3.2	Cause of inefficiency and features of background gamma with the original detector design	30
3.3	Energy threshold dependence of background reduction	31
3.4	Extent of further improvement for background reduction	31
3.5	Strategy for acceptance recovery	33
3.5.1	Comparison between back splash and $\pi^0 \pi^0$ background	33
3.5.2	Reduction of effect of beam accidental activity	35

4 Design of detector and requirements for materials	36
4.1 Strategy for designing the detector	36
4.2 Selection of detector type	37
4.2.1 CsI	38
4.2.2 Sampling detector	39
4.2.3 Selection of detector type	39
4.3 Layer structure of sampling detector	40
4.3.1 Absorber material	40
4.3.2 Sampling ratio and frequency	41
4.4 Support structure	43
4.4.1 Amount of structure material	43
4.4.2 Gap between modules	44
4.5 Energy threshold dependence of sampling detector	44
4.6 Criterea for deciding material requirements	44
4.6.1 Criteria for studying light yield	45
4.6.2 Criteria for studying timing resolution	45
4.6.3 Calculation for photon statistics	46
4.7 Relation between background and acceptance recovery	47
4.7.1 Back splash and $\pi^0\pi^0$ background	47
4.7.2 Beam accidental activity	50
4.8 Decision of detector type and requirements for detector material	50
5 Design for production	52
5.1 Materials for the active part	52
5.1.1 Candidate materials	52
5.1.2 Combination of materials	56
5.1.3 Examination of larger-diameter fiber	59
5.1.4 Selection of extrusion-molding scintillator	60
5.1.5 Light yield of module	60
5.2 Mass production process of active part	60
5.3 Concept for assembling modules	61
5.3.1 Rigid module	61
5.3.2 Module length and readout	63
5.4 Material of non-active part in module	64
5.5 Production process of assembling modules	66
5.6 Design of cylindrical structure	66
6 Light yield and timing resolution obtained by the Inner Barrel and the Main Barrel	68
6.1 Relation between detector response and resolution	68
6.2 Parameters of the Inner Barrel	69
6.2.1 Parameters measured with 500 MHz FADC	70
6.2.2 Waveform of cosmic ray signal	70
6.2.3 Waveform of single photon signal	70
6.3 Parameters of the Main Barrel	72
6.3.1 Light yield	72
6.3.2 Noise level	72

6.3.3	Waveform of cosmic ray signals	74
6.4	Estimation of timing resolution	75
6.4.1	Timing PDF extraction	75
6.4.2	Waveform simulation	76
6.4.3	Time defining method	79
6.4.4	Timing resolution of candidate detectors	81
6.5	Result of light yield and timing resolution of the Inner Barrel and the Main Barrel	83
7	Confirmation of timing resolution with the Main Barrel	84
7.1	Data set for the analysis	84
7.2	5-gamma pointing method	89
7.3	Contamination of accidental hits	90
7.4	Measured timing resolution	91
8	Optimization of veto window and threshold	94
8.1	$K_L \rightarrow \pi^0 \nu \bar{\nu}$ analysis	94
8.1.1	Analysis method	94
8.1.2	Number of signal events	95
8.1.3	Timing and z position distribution of back-splash	95
8.2	Beam accidental event	96
8.2.1	Requirement for acceptance	96
8.2.2	Beam Monte Carlo	97
8.2.3	Event loss expectation	97
8.3	MC method for background estimation	99
8.3.1	Feature and merit of mapping method	99
8.3.2	approach of mapping method	100
8.3.3	Evaluation of inefficiency in mapping method	101
8.4	$K_L \rightarrow \pi^0 \pi^0$ background	103
8.4.1	Timing, z position distribution	103
8.4.2	Vertex mis-reconstruction	104
8.4.3	Late shower events	106
8.4.4	Veto window dependence	106
8.5	S/B ratio related with back splash loss	108
8.6	Decision on veto window and threshold and estimation of significance	109
9	Discussion	111
9.1	Improvement of sensitivity	111
9.2	Advices for module production in further	112
10	Conclusion	114
A	Cut conditions	115
A.1	Cut conditions for 5 gamma analysis	115
A.2	Cut conditions for 2 gamma analysis	116

List of Figures

1.1	Examples of Feynman diagrams of the $K_L \rightarrow \pi^0 \nu \bar{\nu}$ decay [10].	3
1.2	Correlation between the branching ratios of $K_L \rightarrow \pi^0 \nu \bar{\nu}$ and $K^+ \rightarrow \pi^+ \nu \bar{\nu}$ with various physics models [9]. SM4: Standard Model with a sequential 4th generation, RSc: Randall-Sundrum model with custodial protection, LHT: Little Higgs Model with T-parity, and MFV: Minimal Flavor Violation. The Standard Model (SM) prediction is marked by a star. The gray area is ruled out experimentally or by the Grossman-Nir limit.	5
1.3	History of $K_L \rightarrow \pi^0 \nu \bar{\nu}$ search [10, 11]. The green point shows the first study performed by Littenberg. Blue (Red) points in the figure show results of the analysis using $\pi^0 \rightarrow e^+ e^- \gamma$ ($\pi^0 \rightarrow \gamma \gamma$) decay to identify the K_L decay. The green line shows the Grossman-Nir limit. The pink line shows the branching ratio of the $K_L \rightarrow \pi^0 \nu \bar{\nu}$ decay predicted by the Standard Model.	5
1.4	E391a detector system. The Main Barrel (MB) surrounds the decay volume.	6
1.5	Comparison of the gamma detection inefficiency of the E391a Main Barrel (black) and the barrel detectors designed in the proposal of the KOTO (red) [15] as a function of gamma energy [GeV]. Vertical incident gamma at each incident energy were generated by Geant 3 Monte Carlo.	8
1.6	Gamma detection inefficiencies for proposed Main Barrel as a function of incident photon energy [15]. The open black circles show experimental data for photo-nuclear interactions[17]. Geant 3 Monte Carlo results for the inefficiencies due to punch-through and sampling fluctuations are shown by colored points. Different colors indicate different incident angles on the detector. The solid curves show the model inefficiency functions obtained by fitting the data and Monte Carlo results.	8
1.7	Energy distribution of the two gammas that enter the veto counters in the events missing two gammas from the same π^0 ; such events are called “even-pairing background” [15]. The 90 % of $K_L \rightarrow \pi^0 \pi^0$ background is caused by even-pairing background.	9
1.8	Schematic view of a shower and back-splash.	10

1.9	Distribution of the mean timing (horizontal axis) and the timing difference (vertical axis) of phototubes on the both ends of the MB taken in the E391a experiment [15]. The mean timing represents incident time of the gammas. The timing difference represents effective incident position considering the light propagating time in the MB module. The gammas from decays (black) and the back-splash (red) in events which had 4 gammas detected in the calorimeter were caused by the $K_L \rightarrow \pi^0\pi^0\pi^0$ and $K_L \rightarrow \pi^0\pi^0$ modes, respectively. Timing of the back-splash is later for upstream hits.	10
2.1	Schematic view of the π^0 reconstruction.	13
2.2	Bird eye's view of the J-PARC site [20].	15
2.3	The proton transport line after extraction from the Main Ring and the layout of Hadron hall [20]. The K_L beam line is marked as "KL".	16
2.4	Plan view of the KL beam line [21]. Two stages of collimators are placed downstream of the T1 target, a sweeping magnet is located between them, and a photon absorber is located upstream of the collimators.	16
2.5	Setup of the KOTO detector. CsI calorimeter is the main detector and all others are veto detectors for photons or charged-particles. The photon veto detectors are Front Barrel (FB), Neutron Collar Counter (NCC), Main Barrel (MB), Outer Edge Veto (OEV), collar counters (CC03, CC04, CC05, CC06), and Beam Hole Photon Veto (BHPV). Charged-particle veto detectors are HINEMOS, Barrel Charged Veto (BCV), the Charged Veto (CV), Liner Charged Veto (LCV), and Beam Hole Charged Veto (BHCV). The most outside black line shows vacuum vessel. Multi-layer film called "membrane" is drawn with a pink line. Membrane separates a 5×10^{-5} Pa high vacuum region, and a 0.1 Pa low vacuum region where detectors in the vessel are placed.	17
2.6	Cross-section of the CsI calorimeter and other detectors in the cylindrical support structure [24]. Modules with numbers labeled at the edge are the Outer Edge Veto (OEV).	18
2.7	Front view (left) and side view (right) of cylinder.	19
2.8	Cross-sections of the Front Barrel. Each module is connected together behind of the module [22].	20
2.9	Cross-section of the Main Barrel under construction. Each module is supported independently by three support rings aligned in the vacuum vessel. The support ring and the backbone plate are connected by 36-mm-diameter bolts [25].	21
2.10	Cross-section of a module of Main Barrel [22]. The 5-mm-diameter 50 stud bolts fixed the laminate structure covering layers to the backbone plate.	22
2.11	Cross-section of a layer of the Main Barrel with WLS fiber setting and light shields. The grooves for the WLS fibers have a cross-section of 1.2 mm (width) \times 1.3 mm (depth).	22
2.12	Position dependence of the light yield for the Main Barrel. The x is the distance from the photo-cathode of left side PMTs [22].	23

2.13	Schematic view of a 14-bit 125-MHz ADC module with a 10-pole Bessel filter in the KOTO data acquisition system [31].	24
3.1	The K_L beam profile and the K_L momentum distribution at the 20 m downstream of the T1 target. Events are generated in Geant4 MC.	27
3.2	Energy distribution of the two missing gammas in even-pairing background, which were generated in Geant4 MC.	28
3.3	The number of gammas hitting the Main Barrel produced by the $K_L \rightarrow \pi^0\pi^0$ simulation (left). The number of gammas missing at the barrel detectors in the KOTO proposal (right). The number was estimated from the $K_L \rightarrow \pi^0\pi^0$ simulation. The x axis shows the angle θ of incident gamma, and the y axis shows incident energy. The θ is defined as the angle between gamma momentum and the z axis.	28
3.4	Left: Inefficiencies of the Main Barrel. Energy threshold was set to 0.5 MeV. Right: The number of gammas missing at the Main Barrel with inefficiencies in left figure. The number was estimated from the $K_L \rightarrow \pi^0\pi^0$ simulation. The x axis in the right figure shows the angle θ of incident gamma, and the y axis shows incident energy. The θ is defined as the angle between gamma momentum and the z axis.	29
3.5	The inefficiency of the barrel detectors in proposal is shown for each source as a function of incident gamma energy. Each color shows the sources as; black: total inefficiency, blue: punch through in which a gamma deposits the full energy on the virtual detector outside the barrel detectors, pink: leakage in which a gamma deposits enough energy on the virtual upstream or downstream detector, red: photo-nuclear in which a event includes neutron in secondary particles in the rest events, and green: sampling effect which is the rest events.	31
3.6	Kinetic energies of secondary particles in an event. The secondary particles which deposit the energy under (left) or over (right) threshold are created by photo-nuclear interaction. The X axis shows the radius from the beam center and the Y axis shows deposit energy of secondary particles. The barrel detectors were located from 750 mm to 1350 mm in radius. Position of the detector and structure are colored by yellow and green, respectively. Incident energy and angle of generated gamma were 600 MeV and 45 degree. Points connected with a line show initial to final conditions of the particles created by the photo-nuclear and the secondary interactions. Each color of the line shows the kind of particle, neutron, proton and heavy ions drawn in black, red, and magenta, respectively. The case without (with) secondary neutron interaction generates small (large) number of charged particle as shown in left (right) plot. Although some charged particles only interact in absorber, the case of many charged particles tends to be over threshold.	32
3.7	The number of the $\pi^0\pi^0$ background events as a function of energy threshold for the barrel detectors designed in the KOTO proposal.	32
3.8	The number of the $\pi^0\pi^0$ background events shown as a function of CsI cylinder thickness. Green line shows the $\pi^0\pi^0$ background due to other detectors. Energy threshold on the CsI cylinder was set to 0.5 MeV.	33

3.9	The Main Barrel hit timing and z position distribution of backsplash events (left) and the $\pi^0\pi^0$ background events (right) in MC. The position $Z=6148$ mm corresponds to the surface of the CsI calorimeter. The red lines show the mean of the timing and z position relation (t-z line) of back splash events ($t = -0.00320z + 21.2$) and that of the $\pi^0\pi^0$ background events ($t = 0.00231z - 12.8$)	34
3.10	Deposit energy distribution in Main Barrel for back splash events (left) and $\pi^0\pi^0$ background events (right) obtained with the full simulation. A total 10^5 signal events were generated for the left plot, and $6 \times 10^8 \pi^0\pi^0$ events were generated for the right plot. The $\pi^0\pi^0$ plot shows remaining events after event selection.	34
3.11	Timing distribution hitting the barrel detectors without timing resolution caused by timing response of the Main Barrel.	35
4.1	Front view of position assignment in case of E391a CsI crystal (left) and KTeV CsI crystal (right).	38
4.2	Inefficiencies of 7 cm (left) and 5 cm (right) thick CsI detector are shown as a function of incident energy.	38
4.3	Inefficiency of $5-X_0$ -thick sampling detector shown as a function of incident gamma energy.	39
4.4	The number of $\pi^0\pi^0$ background events, at the sensitivity where 3.5 signal events are expected, are shown for Inner Barrel made of CsI (black circles) and sampling detector (red triangles). Solid circle and solid triangle were estimated with the same MC version. Open circle and open triangle were estimated later with another MC with a more realistic detector setup.	40
4.5	The distribution of energy deposit in sampling detectors with iron (left) and lead (right) absorbers. The energy of incident gammas were 30, 100, 300 MeV from the top. The thickness of each absorber plate was 1.5 mm for iron and 1.0 mm for lead. The number of layers were 300 for the detector with iron ($26X_0$) and 200 for the detector with lead ($35X_0$). Black line shows all the events, red line shows events without signal in the BCV, blue line shows events whose secondary particle contain photo-nuclear particles (neutron, proton or heavy ion). Magenta line shows the events in which photo-nuclear particles were created directly from the incident gamma. The numbers shown on the magenta events in the figures are the fractions [%] of these events.	41
4.6	Ratios of inefficiencies between detectors with different layer configurations shown as a function of incident energy of gamma. Left figure shows the ratio for the 42 layers of 3-mm-thick scintillator configuration. Right figure shows the ratio for the 13 layers of 0.6-mm-thick lead configuration. Each color of the points shows 45 (black) and 85 degree gamma incident angles.	42
4.7	The number of the $K_L \rightarrow \pi^0\pi^0$ background events as a function of the areal density of the Inner Barrel support structure. The amount of material is normalized by the area of the Inner Barrel's total outside surface. Cut-out plate is a thicker Back Plate with holes.	43

4.8	The number of the $\pi^0\pi^0$ background events as a function of the energy threshold are shown for sampling detectors with different support structures. Sample0 (magenta reverse triangle) has no support structure, Sample2 (green open circle) is the final design, and Sample1 (black square) has 85 % of the support material of the final design. Design of the KOTO proposal (red circle) and the Main Barrel only (blue triangle) are also shown.	45
4.9	The probability $P(a, x)$ that signals are not observed is shown as a function of the expected number of p.e.s. The black solid line shows the probability for the threshold $a = 1$, the red solid line shows that for $a = 2$, the black dashed line shows that for $a = 3$, and red dashed line shows that for $a = 5$	47
4.10	Timing distribution hitting the barrel detectors with timing resolution caused by timing response of the Main Barrel (red) and a sample detector (black) listed in Table 4.7.	51
5.1	The recorded shapes for different WLS fibers: 1 - BCF-92; 2 - BCF-99-29A; 3 - Pol.Hi.Tech.(S250); 4 - Y-11(MS250); 5 - Y-11(M200); 6 - BCF-91A [38].	53
5.2	Absorption and emission wavelength of Y11-M fiber [28] (left) and BCF-92 fiber [39] (right).	53
5.3	The quantum efficiencies of R329, R329EG and R329EGPX PMTs (left) [29] and R7724 PMT (right) [30]. (“P” and “X” in “EGPX” mean “prism-shaped photocathode” and “developing version”, respectively.)	55
5.4	Relative light yield v.s. the distance from PMT for various combinations of scintillators and fibers. The EJ-200 (magenta), EJ-204(black), EJ-228(red), EJ-232(blue), and the MS-resin used for the Main Barrel (green) were read out by BCF-92 (left) and Y11 (right) fibers.	56
5.5	Timing resolution measured at 2 and 5 m distance for 2 and 5 photo-electron outputs of Y11 and BCF-92 fibers. The curves are estimated values for Y11 and BCF-92 fibers from Eq. (4.6).	57
5.6	Setup to measure light yield in combination of EJ-200 or EJ-204 scintillator and BCF-92 fibers.	57
5.7	Left: The distribution light yield of EJ-200 scintillator and BCF-92 fiber glued with BC600 at 1 m from a PMT. Right: The mean light yield as a function of the position of the ^{90}Sr source on a moving stage. The ADC count is converted to the absolute light yield by one photo-electron count calibrated for PMTs. Combination of EJ-200 scintillator glued with BCF-92 fiber by adhesive BC600 was read out from both ends at 1 m distance. In left plot, the other side PMT signal was required additionally (black line). In right plot, PMT1, 2, means each end readout. Charge of the signal is normalized by that of 1-photoelectron signal measured independently. Difference between PMTs was caused by the difference of PMT quantum efficiency.	58
5.8	Fiber attenuation length about 1.5 mm ϕ (black) and 1.0 mm ϕ (red) BCF-92 fiber irradiated by 405 nm wavelength LED.	59
5.9	Three methods to make rigid module.	62

5.10	Module deformation and compressing force.	62
5.11	Side view of the Inner Barrel. Each size and position was measured value except the calculated position from the upstream edge of the Front Barrel written in parenthesis.	63
5.12	Fiber curvature.	64
5.13	Band guide plastic.	65
5.14	A sample of Cut-out back plate (left) and flat Back Plate at final design (right).	65
5.15	Inner Barrel supported by 8 rings (left figure) and design of ring (right two drawings).	67
5.16	Front view of the Inner Barrel.	67
6.1	Method of timing PDF extraction and combining to realistic waveform. .	69
6.2	Light yield (left) and timing resolution (right) for the Inner Barrel obtained from cosmic ray data taken with 500 MHz FADC [43].	70
6.3	Setup of waveform measurement for cosmic ray data. Top figure shows the front view and bottom figure shows the side view. Trigger counters were placed above and below the Inner Barrel.	71
6.4	Left: Waveform of a cosmic ray event fitted. Right: Overlaid waveforms after matching the fitted peak timing and fitted peak heights. Black points in the right figure show the averaged typical waveform.	71
6.5	Waveform of 1-photoelectron signal measured with R329EGP PMT (left) and R7724 PMT (right). Waveforms were shifted in time to match the fitted peak timing and normalized by the fitted peak height with an gaussian function. Black points show the obtained typical waveform.	72
6.6	Light yields in the units of the number of photoelectrons per MeV for all the channels of the Main Barrel and the Barrel Charged Veto. The light yield is normalized to the value at the center of z direction of modules. .	73
6.7	Pedestal value defined event by event (left) and the sigma of pedestal distribution at each readout channel (right).	73
6.8	Setup to measure the timing PDF of the Main Barrel with cosmic rays. Top view (left) and side view (right) of 4 modules of the Main Barrel and trigger counters are shown. Waveform were taken at the positions of trigger counters A, B, C and D.	74
6.9	Waveform of the Main Barrel taken with a scope. Waveforms were normalized at peak position and overlaid. Black points show the defined typical waveform.	74
6.10	Left: The reduced χ^2 used for fitting the timing PDF is shown for asymmetric gaussian width σ (horizontal axis) and asymmetric parameter a (vertical axis). Top right: Waveform at best fit with $\sigma = 8.47$, $a = 0.382$. Bottom right: Difference of the waveform height between data and MC in the top figure.	76

6.11 Hit position dependence of the timing PDF parameters σ (left) and a (right) for the Main Barrel (top) and the Inner Barrel (bottom). The position 0 mm shows the upstream edge of the detector. Error bar at each point indicates the range of reduced $\chi^2 < 1.1$. Colors in the top two plots show the Inner or Outer module, and the upstream or downstream readout PMT: inner and upstream (black), outer and upstream (red), inner and downstream (blue), and outer and downstream (magenta). Colors in the bottom two plots show the upstream or downstream readout PMT for two modules: upstream (black and blue), and downstream (red and magenta).	77
6.12 Samples of generated waveforms for 5, 10, 100 photoelectrons in the Main Barrel (left) and the Inner Barrel (right). Pedestal was set to 500 counts.	78
6.13 An example of defining constant fraction time (left) and parabola fitting time (right). Sampling points are shown in black points. The base lines are shown in green horizontal lines. Red vertical arrows show the decided timings. In the right figure, purple points show moving averages of neighboring 5 sampling points. These figures are taken from [44].	79
6.14 The fraction of events that signal is not detected in the Main Barrel.	80
6.15 Fit parameters of “asymmetric gaussian fitting method” (black, red, blue, and magenta) and “fixed parameter fitting method” (green). The left plots show σ , and the right plots show a , for the Main Barrel (top) and the Inner Barrel (bottom).	81
6.16 The timing resolution of each detector component and readout system evaluated with “asymmetric gaussian fitting method” (black), “parabola fitting method” (red), “constant fraction method” (blue), and “fixed parameter fitting method” (magenta). Each plot shows the combination of fiber types and FADC frequencies: Y11 fiber and 125 MHz FADC (top left), Y11 fiber and 500 MHz FADC (top right), BCF-92 fiber and 125 MHz FADC (bottom left), and BCF-92 fiber and 500 MHz FADC (bottom right).	82
7.1 The conceptual view of the KOTO analysis scheme. (Some data partially include two types of contents expressed as “data unit”. For instance, Raw data includes not only FADC samples but also integrated ADC.)	85
7.2 The z-position dependence of ADC output at the Main Barrel [11].	88
7.3 Left: Signal counting rate at each Main Barrel module. Center: The largest energy deposit in the modules of the Main Barrel for TMON trigger data. Right: The deposit energy distribution of 6th gamma hitting the Main Barrel for data and MC with accidental overlay. Module ID shown in the bottom left figure was numbered in a clockwise direction viewed from upstream from the near primary beam side for inner 32 modules and later outer 32 modules. Therefore, ID 0 and 31 for the inner modules, 32 and 63 for the outer modules were placed near the primary beam line.	90
7.4 Detected and reconstructed z-positions. The $Z = 0$ mm is defined as the center of the Main Barrel.	92
7.5 The width σ_T (left) and σ_Z (right) at each deposit energy region. Each color shows data (black) and MC with (blue) and without (magenta) resolution caused by waveform.	92

8.1	Timing and z-position distributions of the largest energy deposit of the backsplash particles hitting the barrel detectors in the $K_L \rightarrow \pi^0 \nu \bar{\nu}$ mode. Full simulation without timing and z-position smearing (left), that with smearing for the Main Barrel (center), and that with smearing for the middle-stream Barrel detectors (right). The flat line ($vetoT = 40.7$) shows the veto timing. The black shallow line ($vetoT = -5.67 \times 10^{-3}z + 53.93$) shows the mean timing of back-splash events.	95
8.2	Factor of acceptance and signal yield as a function of beam intensity for 10 % (red) and 3% (black) acceptance loss at 24 kW beam intensity. Signal yield is normalized by that at 24 kW beam intensity. Beam cycle is assumed to be 2 sec spill and 6 sec beam cycle as in May 2013.	97
8.3	Generated particle id (left) and deposit energy on the Main Barrel for each source particle (right).	98
8.4	A_{sig} as a function of width of veto window for 24 kW 6-second beam cycle (green), 100 kW 4-second beam cycle (red), and a factor 3 higher accidental hit rate in 100 kW 4-second beam cycle (blue). Each line style shows the acceptance for thresholds at 2 MeV (dotted line), 1 MeV (dashed line), and 0.5 (solid line), respectively.	99
8.5	Left: The deposit energy distribution in the Main Barrel estimated with loose kinematic cuts. Red points show the result of Full MC. Blue points show the mapping method result assuming that only the 6th gamma hit the Main Barrel. Black points show the mapping method result assuming not only 6th gamma but also back splash of 5 gammas in the calorimeter hit the Main Barrel. Right: The probability of not observing backsplash in the Main Barrel when 2 (red), 4 (black), and 6 (magenta) gammas entered the calorimeter from the $K_L \rightarrow \pi^0 \nu \bar{\nu}$, $K_L \rightarrow \pi^0 \pi^0$ and $K_L \rightarrow \pi^0 \pi^0 \pi^0$ modes, respectively. Inefficiency thus includes events which do not have backsplash particle hitting the Main Barrel. In addition, 3 (blue) (5 (green)) gamma incident in the calorimeter was approximated as the mean of 2 and 4 (4 and 6) gamma incidence.	102
8.6	The number of the $K_L \rightarrow \pi^0 \pi^0$ background events as a function of threshold at limited hitting z-position $-4000 < z < 1800$ (left) and $2050 < z < 2200$ (right) with loose cuts (only fiducial and z-vertex position cuts). The position of the center of the Main Barrel is $z = 0$, and that of the surface of the CsI calorimeter is $z=2048$ mm. The numbers of background events were estimated by mapping method (black) and Full MC (red).	103
8.7	Timing and z-position distribution of the $K_L \rightarrow \pi^0 \pi^0$ decay mode generated in original full simulation (left), and events hitting the region excluding CsI edge region after applying energy deposit probability, and timing and z position resolution based on the mapping method for the Main Barrel (middle) and the middle-stream Barrel detectors (right). The x-axis is defined as $z = 0$ to be the center of the Main Barrel. The events in the left plot were generated with the number of K_L decays which would give a signal S.E.S of 5.2×10^{-11} . The region between a solid black line and a solid black curve shows an example of veto window.	104

8.8 Timing and z-position distribution of the $K_L \rightarrow \pi^0\pi^0$ events which have gammas hitting the CsI edge region. Top two figures show the case with the Main Barrel, and the bottom two figures show the case with the middle-stream Barrel detectors. The plots on the left show hits with the maximum energy, and the plots on the right show the hits with the timing nearest to the veto timing. The number of generated events for the middle-stream Barrel detectors was 3.8 times that of the Main Barrel. Distributions were created by recycling original full simulation events 100 times, which was equivalent to generating the number of the K_L that would give S.E.S = 5.2×10^{-13} for the signal. The $z = 0$ in these plots corresponds to the center of the Main Barrel. The region between a solid black line and a solid black curve shows an example of veto window. 105

8.9 The fastest limit of the mis-reconstructed timing is shown at the largest difference of the length L_3 and L_4 . If the CsI calorimeter mis-measures the gamma energy lower, the vertex is reconstructed downstream rather than the true vertex. 106

8.10 Event display (left) and deposit energy and timing of the Main Barrel (right) for a $K_L \rightarrow \pi^0\pi^0$ event which created a late shower. Another module has an energy deposit near the veto timing. 107

8.11 The number of the $K_L \rightarrow \pi^0\pi^0$ background events is shown as a function of the veto window width for the Main Barrel (left) and the middle-stream Barrel detectors (right). Each line shows the events with the energy threshold 2 MeV (black), 1 MeV (red), and 0.5 MeV (blue). Veto window was moved for all events (dashed line) and for only < 5 MeV deposit events (solid line). The veto window for > 5 MeV deposit events in solid line was fixed at 60 ns width to detect late shower events caused by photo-nuclear interaction. 107

8.12 A S/B ratio but scaled with 5×10^7 over S/B for 100×100 bins plotting points based on the signal shown in Fig. 8.1 and the background events shown in Fig. 8.7 and Fig. 8.8. The z-axis thus gives better S/B with the value $> 5 \times 10^3$ for each point. Upper three figures show the case of the Main Barrel, and lower three figures show the case of the middle-stream Barrel detectors for subdivided energy deposits $2 < E_{dep} < 5$ MeV (left), $1 < E_{dep} < 2$ MeV (center) and $0.5 < E_{dep} < 1$ MeV (right). The number drawn in the plots are the recovered signal ratio if the narrower “on time +8 ns” veto window (red line) is applied. The recoveries are 10.2 % for the Main Barrel, and 10.8 % for the Inner Barrel. 108

8.13 The significance S/\sqrt{B} as a function of the veto window for all events with the Main Barrel (top left) and with the middle-stream Barrel detectors (bottom left), and the fixed ± 30 ns veto window for > 5 MeV deposit events and the changed veto window for other events about the Main Barrel (top right) and the middle-stream Barrel detectors (bottom right). Each color shows the beam condition: 24 kW 6 seconds cycle (blue), 100 kW 4 seconds cycle (black), and assuming a 3 times higher accidental event rate at 100 kW 4 seconds cycle (red). The line styles represent the veto energy threshold: 2 MeV (solid line), 1 MeV (dashed line), and 0.5 MeV (dotted line). 109

9.1 The branching ratio sensitive to a New Physics with 3σ evidence (solid line) and the $K_L \rightarrow \pi^0 \nu \bar{\nu}$ observation in the Standard Model branching ratio with 3σ evidence (dashed line) without the Inner Barrel (red) and with the Inner Barrel (black). Each point shows the branching ratio at a scale factor α satisfying the expectation $P = 2.7 \times 10^3$ for each observed number of events n in Eq. (9.2) 112

List of Tables

2.1	Branching ratios of K_L decay modes listed in the Particle Data Group [18] and of the $K_L \rightarrow \pi^0 \nu \bar{\nu}$ decay predicted by the Standard Model. The value for $K_L \rightarrow \pi^0 \nu \bar{\nu}$ decay is based on the SM prediction. Major four modes and background source decays are listed. Maximum momentum p_{max} is the kinematic limit of the π^0 momentum in the K_L rest frame. Visible particles in the final states of K_L decays are also listed. The number of visible particles is shown for charged particles (ch) and gammas (γ)	14
2.2	Beam parameters in May 2013 and in the original design.	15
2.3	The design parameters of the barrel detector [22]. (* Confirmed by photo taken in 2012.)	21
4.1	Properties of crystal [18] about decay time (D.T.), light yield (L.Y.), wave length (W.L.), radiation length and appropriateness (bottleneck compared to CsI (pure)) for the new Barrel detector. The light yield shows relative light output, not including the quantum efficiencies of the photodetector. Some crystals have two components of faster (f) and slower (s) decay times.	37
4.2	The number of $\pi^0 \pi^0$ background events with the Inner Barrel made of different sampling conditions.	42
4.3	The number of $\pi^0 \pi^0$ background events with $0 \sim 4$ mm gap between modules. The module was sandwiched between an iron Back Plate and Front Plate, and the sides were covered with 0.5-mm-thick iron plates.	44
4.4	Probability of the signal events having back splash hits on the barrel detectors, the number of the $\pi^0 \pi^0$ background events in Section 4.5, and the α , β and α/β (change of S , B and S/B) compared with those with a 0.5 MeV threshold.	48
4.5	Ratio of the number of the $\pi^0 \pi^0$ background events with to without photon statistics, B_{pstat}/B_0 . Energy distribution of the $\pi^0 \pi^0$ events is approximated as a function $N(E_{dep}) = 10^{0.13E_{dep}+0.5}$ for energy E_{dep} [MeV] based on Fig. 3.10 (right).	49
4.6	Ratio of the number of the accepted signal events with to without photon statistics, $S_{pstat}/S_0 = (S_{tot} - S_{PstatLoss})/(S_{tot} - S_{0Loss})$, where $S_{PstatLoss}$ and S_{0Loss} are the number of back-splash loss events calculated in the same way as N_{pstat} and N_0 in Section 4.6.3, and S_{tot} is the number of signal events detected in the calorimeter. Energy distribution of back-splash is approximated as $S_{loss}(E_{dep})[MeV] = 10^{-0.3E_{dep}+4}$ from Fig. 3.10 (left).	49

4.7	Timing resolution is calculated as a function $\sigma_T = Cb/\sqrt{nE_{ins}}$, where C is the decay time of the light emission in detector material, n is the light yield, b is the factor of the both end readout as $b = 1$ (CsI), $1/\sqrt{2}$ (others), E_{in} is the incident energy, and s is the sampling ratio of the detector as $s = 1$ (CsI), 0.3 (others). Here, the energy E_{in} is set to 100 MeV in this table as the average of incident gamma energy for the $K_L \rightarrow \pi^0\pi^0$ background.	50
5.1	Properties of Y11 (M200) fiber [28] and single and multi cladding BCF-92 fibers [39].	53
5.2	Features of tested scintillators [40].	54
5.3	Properties of glues, BC-600 [39] and NOA61 [41], and grease BC-630 [39]. .	55
5.4	Light yield for different configurations measured by changing only one condition from the basic configuration.	58
8.1	Accidental event rate (n_{acd}) estimated from beam MC for the flux $F_{K_L Full}$. .	98
A.1	Cut values for 5-gamma analysis.	116
A.2	Cut values for signal mode.	117

Chapter 1

Introduction

The Standard Model of particle physics has explained various phenomena observed in many experiments. This model also explained breaking of a symmetry between particles and anti-particles and parity transformation (CP). The CP violation was first observed experimentally in 1964 [1] and explained by the Cabibbo-Kobayashi-Maskawa (CKM) model in 1973 [2]. The CKM model later became a part of the Standard Model. The Standard Model seems to be completed.

However, there are still questions from cosmic observation. One of the greatest questions is the matter dominance in the universe. The amount of matter and anti-matter in the universe should be equal in fundamental understanding based on symmetries. Even though the CP violation in the Standard Model explains a part of the inequality, the magnitude of the inequality is too small to explain the observation. Another mechanism causing the inequality should exist. We thus search for new physics beyond the Standard Model by examining CP violation.

The KOTO experiment is one of the principal experiments searching for the origin of CP violation beyond the Standard Model. The experiment aims to make the first observation of $K_L \rightarrow \pi^0 \nu \bar{\nu}$ decay and to measure its branching ratio. The $K_L \rightarrow \pi^0 \nu \bar{\nu}$ decay has an advantage to probe the discrepancy of the magnitude of CP violation from the Standard Model because of the small branching ratio of the Standard Model contribution and its small theoretical uncertainty.

This thesis describes a major detector improvement to achieve the aim of the KOTO experiment.

1.1 CP violation in the Standard Model

The Standard Model is based on a symmetry combining three discrete symmetries:

- Charge conjugation (C): exchanging particles and anti-particles,
- Parity (P): inverting the space coordinate, $\mathbf{x} \rightarrow -\mathbf{x}$, and
- Time reversal (T): inverting the time coordinate, $t \rightarrow -t$.

The CP symmetry is the combination of C and P symmetries. Today, we know that CP symmetry is slightly broken in weak interaction.

The Lagrangian of the charged current in the weak interaction is given by:

$$\mathcal{L}_{CC} = \frac{-g_w}{2\sqrt{2}} [\bar{u}_i \gamma^\mu (1 - \gamma^5) V_{ij} d_j W_\mu^+ + \bar{d}_j \gamma^\mu (1 - \gamma^5) V_{ij}^* u_i W_\mu^-], \quad (1.1)$$

where subscripts i ($j=1, 2, 3$) denote generations of quarks, $u_i = (u, c, t)$ are up-type quarks, and $d_i = (d, s, b)$ are down-type quarks. The V_{ij} is an element of Cabibbo-Kobayashi-Maskawa (CKM) matrix (V_{CKM}). The CKM matrix connects the up-type quarks with the down-type quarks as:

$$V_{CKM} = \begin{pmatrix} V_{ud} & V_{us} & V_{ub} \\ V_{cd} & V_{cs} & V_{cb} \\ V_{td} & V_{ts} & V_{tb} \end{pmatrix}. \quad (1.2)$$

By transforming CP state, the Lagrangian changes as:

$$\mathcal{L}_{CC} \xrightarrow{CP} \frac{-g_w}{2\sqrt{2}} [\bar{u}_i \gamma^\mu (1 - \gamma^5) V_{ij}^* d_j W_\mu^+ + \bar{d}_j \gamma^\mu (1 - \gamma^5) V_{ij} u_i W_\mu^-]. \quad (1.3)$$

If a CP symmetry is always conserved, two Lagrangians expressed in Eq. (1.1) and Eq. (1.3) should be equal. It thus means $V_{ij} = V_{ij}^*$.

The CKM matrix expressed in Wolfenstein parameterization [3] by setting $\lambda = |V_{us}| = 0.22$ is:

$$V_{CKM} = \begin{pmatrix} 1 - \lambda^2/2 & \lambda & A\lambda^3(\rho - i\eta) \\ -\lambda & 1 - \lambda^2/2 & A\lambda^2 \\ A\lambda^3(1 - \rho - i\eta) & -A\lambda^2 & 1 \end{pmatrix} + \mathcal{O}(\lambda^4), \quad (1.4)$$

where A , λ , ρ and η are real-number coefficients independent of each other. The η represents the imaginary part of the CKM matrix and thus represents the scale of CP violation.

1.2 $K_L \rightarrow \pi^0 \nu \bar{\nu}$ decay

The $K_L \rightarrow \pi^0 \nu \bar{\nu}$ decay occurs only if CP is violated. We describe its relation to the CP violation, its predicted branching ratio and theoretical uncertainty, and experiments that searched for the decay in the past.

1.2.1 $K_L \rightarrow \pi^0 \nu \bar{\nu}$ decay in the Standard Model

The long-lived neutral kaon, K_L , is a mass eigenstate of a meson composed of d quark and s quark.

The longer life time of this kaon is explained by the fact that CP is mostly conserved in weak interaction. Neutral kaon has the $\pi\pi$ and $\pi\pi\pi$ final states. The $\pi\pi$ is in a CP-even state, and the $\pi\pi\pi$ is in a CP-odd state. Therefore, neutral kaon in CP-odd state, historically named K_2 , decays into $\pi\pi\pi$ and has a longer lifetime than kaon in CP-even state K_1 , because the Q value ($m_K - \Sigma m_\pi$) for $K \rightarrow \pi\pi\pi$ is smaller than that for $K \rightarrow \pi\pi$. Although the K_L is not strictly equal to the K_2 due to the existence of CP violation, the K_L can be approximately represented as K_2 .

Neutral kaon is categorized also on the basis of flavor eigenstate as $K^0 = (d, \bar{s})$ and its anti-particle \bar{K}^0 ($|\bar{K}^0\rangle = CP|K^0\rangle$). The K_L state is expressed as:

$$|K_L\rangle \sim |K_2\rangle = \frac{1}{\sqrt{2}}(|K^0\rangle - |\bar{K}^0\rangle). \quad (1.5)$$

The Feynman diagrams for the $K_L \rightarrow \pi^0 \nu \bar{\nu}$ decay are shown in Fig. 1.1. The tran-

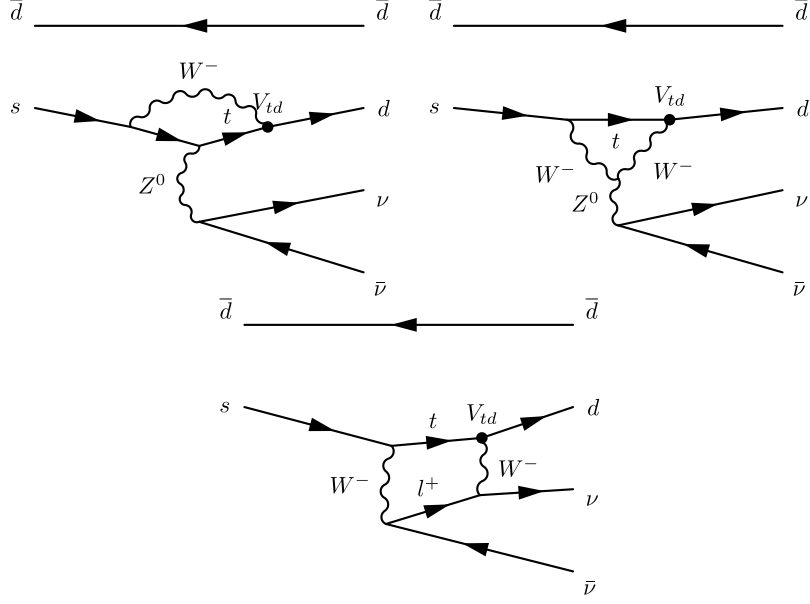


Figure 1.1: Examples of Feynman diagrams of the $K_L \rightarrow \pi^0 \nu \bar{\nu}$ decay [10].

sition from s quark to d quark involves a loop in the diagrams. The t quark dominates the contribution in the loop because the mass of the t quark is 100 times larger than that of the c quark [4]. The decay amplitude of the $K_L \rightarrow \pi^0 \nu \bar{\nu}$ decay is expressed as:

$$\begin{aligned} A(K_L \rightarrow \pi^0 \nu \bar{\nu}) &\sim \frac{1}{\sqrt{2}}(A(K^0 \rightarrow \pi^0 \nu \bar{\nu}) - A(\bar{K}^0 \rightarrow \pi^0 \nu \bar{\nu})) \\ &\propto V_{td}^* V_{ts} - V_{ts}^* V_{td} \\ &\propto 2i\eta. \end{aligned} \quad (1.6)$$

In this decay amplitude, the contribution from the real part is canceled, and only the imaginary part remains.

In a quantitative calculation [6], the branching ratio is written as:

$$Br(K_L \rightarrow \pi^0 \nu \bar{\nu}) = \kappa_L \left(\frac{\text{Im} \lambda_t}{\lambda^5} X_t \right)^2, \quad (1.7)$$

$$\kappa_L = (2.231 \pm 0.013) \times 10^{-10} \left[\frac{\lambda}{0.225} \right]^8, \quad (1.8)$$

where κ_L is a factor of the hadronic matrix element, $\lambda_t = V_{ts}^* V_{td}$, and X_t is a function relevant to internal t quark loops, which was originally presented as the Inami-Lim loop

function [5], with higher-order QCD corrections and electroweak two-loop corrections. The κ_L is extracted from the $K_L \rightarrow \pi e \nu$ branching ratio which was measured precisely by experiments.

With the calculated value $X_t = 1.469 \pm 0.017 \pm 0.002$ based on measured parameters, the branching ratio of the $K_L \rightarrow \pi^0 \nu \bar{\nu}$ decay is predicted [6] as:

$$Br(K_L \rightarrow \pi^0 \nu \bar{\nu}) = (2.43_{-0.37}^{+0.40} \pm 0.06) \times 10^{-11}. \quad (1.9)$$

The first error is related to uncertainties in the input parameters. Its main contributions come from V_{cb} (54%), η (39%) and t -quark mass (6%). The second error shows the remaining theoretical uncertainty. The theoretical uncertainty in the branching ratio of the decay is only 2 %.

1.2.2 $K_L \rightarrow \pi^0 \nu \bar{\nu}$ decay beyond the Standard Model

An upper limit of the $K_L \rightarrow \pi^0 \nu \bar{\nu}$ branching ratio called Grossman-Nir (GN) limit [7] is given by its isospin partner, $K^+ \rightarrow \pi^+ \nu \bar{\nu}$ mode as:

$$Br(K_L \rightarrow \pi^0 \nu \bar{\nu}) < 4.4 \times Br(K^+ \rightarrow \pi^+ \nu \bar{\nu}). \quad (1.10)$$

The measured branching ratio of the $K^+ \rightarrow \pi^+ \nu \bar{\nu}$ decay [8] is:

$$Br(K^+ \rightarrow \pi^+ \nu \bar{\nu}) = (1.73_{-1.05}^{+1.15}) \times 10^{-10}. \quad (1.11)$$

From these two, the current upper limit of the $K_L \rightarrow \pi^0 \nu \bar{\nu}$ branching ratio is:

$$Br(K_L \rightarrow \pi^0 \nu \bar{\nu}) < 1.2 \times 10^{-9} \text{ (68\% C.L.)}. \quad (1.12)$$

Figure 1.2 shows the correlation between the branching ratios of $K^+ \rightarrow \pi^+ \nu \bar{\nu}$ and $K_L \rightarrow \pi^0 \nu \bar{\nu}$ with various models for new physics. These two branching ratios show different correlation between the physics models. Basically, discrepancy from the Standard Model observed in either mode becomes the evidence of new physics. Moreover, the correlation of these two modes can limit individual models.

1.2.3 History of $K_L \rightarrow \pi^0 \nu \bar{\nu}$ search

Several experiments were carried out to search for the $K_L \rightarrow \pi^0 \nu \bar{\nu}$ decay. Figure 1.3 shows the progress of the search.

The first upper limit on the branching ratio of $K_L \rightarrow \pi^0 \nu \bar{\nu}$ decay was set by analyzing the data taken for the $K_L \rightarrow \pi^0 \pi^0$ study [12].

Following studies are classified into two types. One type used the $\pi^0 \rightarrow e^+ e^- \gamma$ decay to identify π^0 [13]. Although, there was a merit of reconstructing π^0 cleanly by using e^+ and e^- tracks, the sensitivity was lowered by more than 3 orders of magnitude due to the small branching ratio of the $\pi^0 \rightarrow e^+ e^- \gamma$ decay, 1.2%, and small acceptance due to a small opening angle between e^+ and e^- .

The other type of experiments uses the $\pi^0 \rightarrow \gamma \gamma$ decay. This decay has an advantage that its branching ratio is large (99 %). KEK PS E391a experiment, which was the first dedicated experiment for the $K_L \rightarrow \pi^0 \nu \bar{\nu}$ decay, used this decay mode. This experiment gave the current best upper limit on the branching ratio [14],

$$Br(K_L \rightarrow \pi^0 \nu \bar{\nu}) < 2.6 \times 10^{-8} \text{ (90\% C.L.)}. \quad (1.13)$$

The KOTO experiment is a successor of the E391a experiment. Techniques developed in the E391a experiment was further improved for the KOTO experiment.

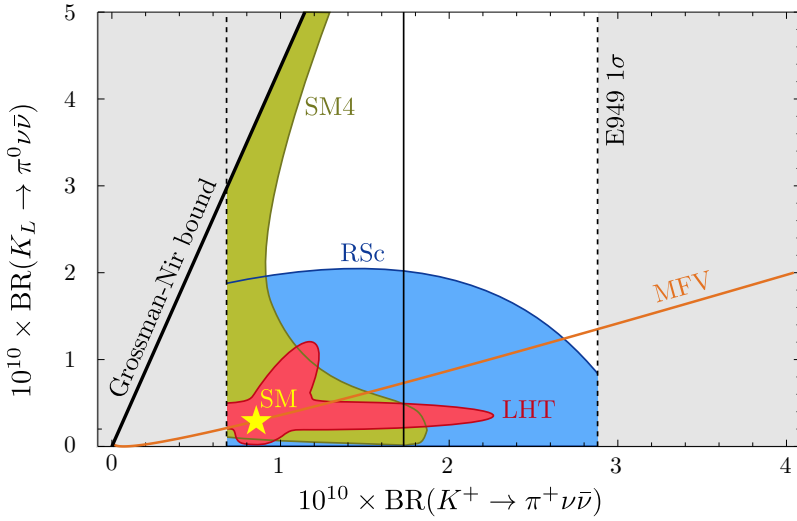


Figure 1.2: Correlation between the branching ratios of $K_L \rightarrow \pi^0 \nu \bar{\nu}$ and $K^+ \rightarrow \pi^+ \nu \bar{\nu}$ with various physics models [9]. SM4: Standard Model with a sequential 4th generation, RSc: Randall-Sundrum model with custodial protection, LHT: Little Higgs Model with T-parity, and MFV: Minimal Flavor Violation. The Standard Model (SM) prediction is marked by a star. The gray area is ruled out experimentally or by the Grossman-Nir limit.

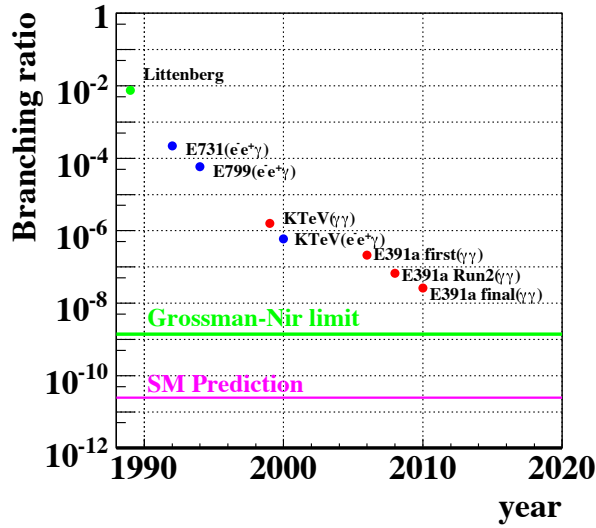


Figure 1.3: History of $K_L \rightarrow \pi^0 \nu \bar{\nu}$ search [10, 11]. The green point shows the first study performed by Littenberg. Blue (Red) points in the figure show results of the analysis using $\pi^0 \rightarrow e^+ e^- \gamma$ ($\pi^0 \rightarrow \gamma \gamma$) decay to identify the K_L decay. The green line shows the Grossman-Nir limit. The pink line shows the branching ratio of the $K_L \rightarrow \pi^0 \nu \bar{\nu}$ decay predicted by the Standard Model.

1.2.4 Techniques at the E391a experiment

The KEK E391a experiment searched for the $K_L \rightarrow \pi^0 \nu \bar{\nu}$ decay signal by requiring only two gammas from the π^0 with a finite transverse momentum (P_T). Requiring a high P_T suppressed the contamination of other K_L decays, for instance, the $K_L \rightarrow \gamma\gamma$ decay. For this method, the E391a experiment used several techniques.

First, an intense and narrow K_L beam was constructed. Proton beam was extracted from the 12-GeV Proton Synchrotron at KEK. The K_L 's produced at a target passed through bending magnets and collimators located in the beam line. The K_L yield at the upstream end of the E391a detectors was 3.3×10^5 per beam cycle (spill) [15].

Second, a detector system was developed to detect only two gammas with a finite P_T . The energy and position of the two gammas needed to be accurately measured to reconstruct π^0 mass and to require a finite P_T . Figure 1.4 shows the detector system. CsI crystals with $7 \times 7 \text{ cm}^2$ cross-section were placed downstream of decay volume for

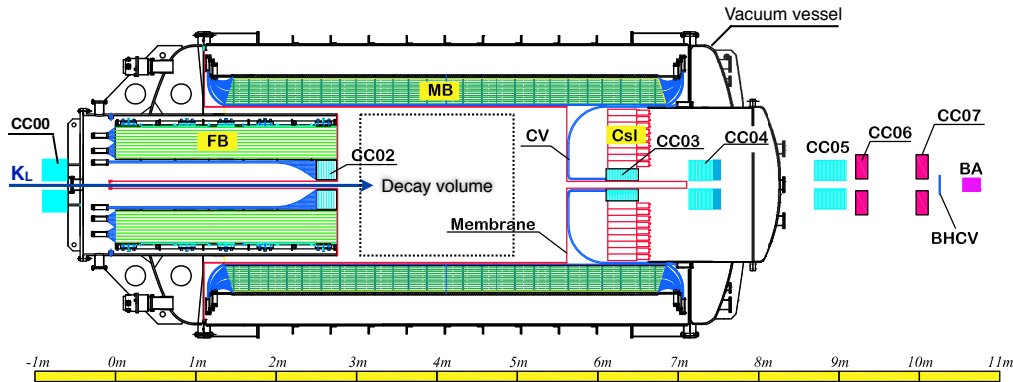


Figure 1.4: E391a detector system. The Main Barrel (MB) surrounds the decay volume.

the gamma measurement.

The CsI crystals and veto detectors surrounding other directions proved that no other particles were in the decay. The veto detector surrounding the decay volume was the Main Barrel. It was a sampling detector made of plastic scintillator and lead with the total thickness of 14 radiation lengths (X_0). The Main Barrel detected additional gammas from other K_L decays such as the $K_L \rightarrow \pi^0 \pi^0$ decay.

Last, high vacuum of 10^{-4} Pa was required to reduce the interaction between gas and beam. Beam pipe to keep high vacuum was removed in the decay volume to reduce the interaction between material of beam pipe and decay particles. The E391a detector was thus placed inside vacuum and high vacuum region is separated from the detectors by membrane to suppress outgassing from detector material.

With these techniques, the experiment gave the upper limit described in Section 1.2.3. Although no events were observed, 0.41 ± 0.11 background events were expected because few events remained near the signal region. The E391a collaboration concluded that those few events were caused by neutrons coming along the beam interacting with inactive materials near the beam.

1.3 The KOTO experiment

By improving the techniques developed in the E391a experiment, the KOTO experiment was designed to study the $K_L \rightarrow \pi^0 \nu \bar{\nu}$ decay in two steps. The KOTO Step 1 [15] aims to make the first observation of $K_L \rightarrow \pi^0 \nu \bar{\nu}$ decay. Step 2 [15] aims to measure the $K_L \rightarrow \pi^0 \nu \bar{\nu}$ branching ratio with a < 10 % accuracy.

The KOTO collaboration started its physics run of Step 1 in 2013, and plans to run for several years. This thesis focuses on Step 1. In this thesis, unless noticed, the KOTO means the KOTO Step1. In this section, improvements from the E391a experiment to achieve the goal of the KOTO are described.

1.3.1 Improvements from E391a to the KOTO

To reach the sensitivity capable of observing the decay with a branching ratio predicted by the Standard Model, 2.4×10^{-11} , the sensitivity of the KOTO experiment has to be improved by three orders of magnitude from the E391a experiment.

We developed a higher intensity beam line, a higher resolution gamma calorimeter, and a more sensitive veto system.

The new beam line was constructed at the Japan Proton Accelerator Research Complex (J-PARC). The measured normalized K_L yield at the upstream end of the KOTO detector was 1.94×10^7 for Ni target and 4.19×10^7 for Pt target per 2×10^{14} photons on the target [16]. These yields were equivalent to 60 and 130 times higher than that of the E391a experiment per beam cycle.

Crystals of the gamma calorimeter were replaced with smaller crystals. The cross-section of the crystals were changed from 7 cm square to 2.5 cm square for the central region and 5.0 cm square for the outer region. Using smaller crystals improved separating multiple gammas.

Veto detectors were also upgraded. Charged veto counter in front of the CsI calorimeter was replaced with a new counter with small inactive materials near the beam. Photon veto detectors located downstream of the calorimeter were also replaced to match the KOTO beam shape and intensity.

We inherited the vacuum vessel and barrel veto detectors from the E391a experiment. Because the thickness of the Main Barrel was not sufficient for KOTO, we planned to add $5-X_0$ thick sampling detector outside the Main Barrel.

According to the KOTO proposal [15], the expected number of signal events was 3.5 and the number of the $K_L \rightarrow \pi^0 \pi^0$ background events was 1.8. The major background was the $K_L \rightarrow \pi^0 \pi^0$ decay whose gammas were not detected by the Main Barrel.

We thus decided to build a more effective detector to be added to the Main Barrel.

Next subsection describes the possibility of further background reduction. In addition, a possibility to increase the signal acceptance is described.

1.3.2 New barrel veto detector to be added to the Main Barrel

We planned to make a new barrel detector to be added to the Main Barrel to improve two major aspects. One was the background reduction brought by additional detector thickness and more efficient detector materials, and the other was acceptance recovery brought by a better timing resolution.

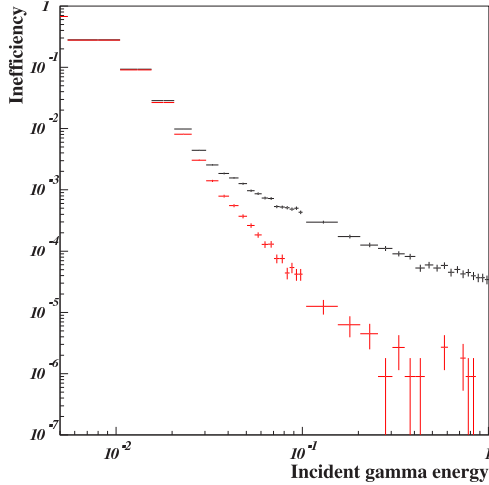


Figure 1.5: Comparison of the gamma detection inefficiency of the E391a Main Barrel (black) and the barrel detectors designed in the proposal of the KOTO (red) [15] as a function of gamma energy [GeV]. Vertical incident gamma at each incident energy were generated by Geant 3 Monte Carlo.

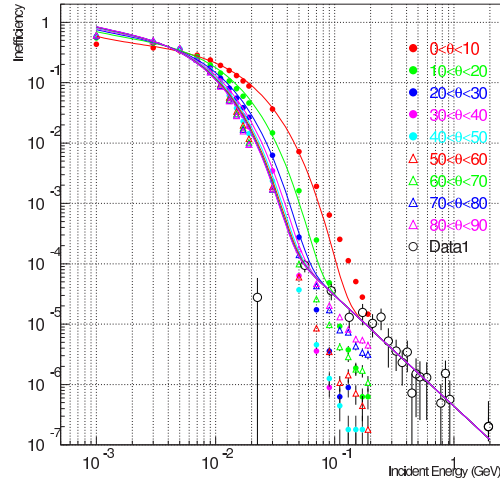


Figure 1.6: Gamma detection inefficiencies for proposed Main Barrel as a function of incident photon energy [15]. The open black circles show experimental data for photo-nuclear interactions[17]. Geant 3 Monte Carlo results for the inefficiencies due to punch-through and sampling fluctuations are shown by colored points. Different colors indicate different incident angles on the detector. The solid curves show the model inefficiency functions obtained by fitting the data and Monte Carlo results.

Background reduction

The original motivation for adding a new detector was to suppress background. When we proposed the KOTO experiment, we planned to add a new detector outside the E391a Main Barrel. The assumed new detector was a $5-X_0$ thick sampling detector consisting of 5 layers of 5-mm-thick plastic scintillator and 5-mm-thick lead. The inefficiency of the Main Barrel with the new detector was calculated for vertical incident gammas as shown in Fig. 1.5. The detection efficiency drastically improved by reducing the probability of punching-through gammas.

In addition to the punching-through, other two sources had the possibility to cause an inefficiency. These two were sampling effect and photo-nuclear interaction.

The sampling effect is caused by low energy electromagnetic shower contained in radiators of the detector, and thus dominant for low energy photons. Thick radiators lowers the probability of detecting showers because radiators are dead material.

The photo-nuclear interaction is caused by gamma kicking nucleus in detector material. If a gamma kicks only neutrons and the neutrons do not kick charged particles, the interaction is not detected. The interaction is also not detected if a gamma kicks low energy charged nucleons. Such charged particles, mostly protons, often deposit their energies only in radiators, because low energy charged particles are mainly created in

the radiators and stop immediately in the material. Inefficiency caused by photo-nuclear interaction measured by a dedicated experiment [17] was directly applied for the background estimation in the KOTO proposal as shown in Fig 1.6 because the photo-nuclear interaction was not available in the Monte Carlo then.

If we add a detector outside the Main Barrel, we cannot reduce the inefficiencies caused by sampling effect and photo-nuclear interaction because most gammas interact in the Main Barrel. With the additional detector outside the Main Barrel, most $K_L \rightarrow \pi^0\pi^0$ background events have at least one gamma with the energy larger than 70 MeV as shown in Fig. 1.7.

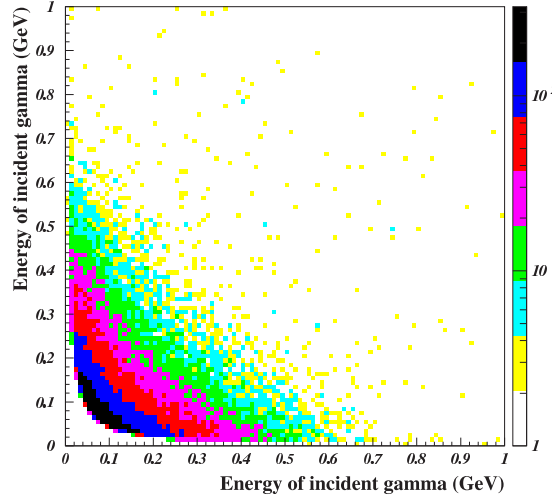


Figure 1.7: Energy distribution of the two gammas that enter the veto counters in the events missing two gammas from the same π^0 ; such events are called “even-pairing background” [15]. The 90 % of $K_L \rightarrow \pi^0\pi^0$ background is caused by even-pairing background.

One method to further suppress the $K_L \rightarrow \pi^0\pi^0$ background was to detect gammas with energies > 70 MeV. The detection efficiency in this energy region was dominated by photo-nuclear interactions in the estimation. We should thus reduce photo-nuclear interaction background.

The other method was to reduce the sampling effect by reducing the amount of dead material. Lower ratio of dead material is required near the detector surface on the beam side because most gammas interact immediately after entering the detector.

If we add a more active detector inside the E391a Main Barrel instead of outside, we can reduce not only the punch-through backgrounds but also backgrounds caused by sampling effect. We named this new detector the Inner Barrel. With the Inner Barrel, the inefficiency caused by photo-nuclear interaction can also be reduced, because low energy charged particles are more visible in the detector with low dead material.

In the process of deciding the design of the Inner Barrel, we had to understand not only the inefficiency sources but also the number of background events. In addition, the amount of dead material, such as the support structure, should be minimized because it affects the sensitivities of the Main Barrel located outside.

Acceptance recovery

Let us next discuss how to recover signal acceptance with the Inner Barrel. The Main Barrel had a high rate of accidental hits and back-splash events due to its large detector size. Accidental hits were caused by some particles hitting the Main Barrel accidentally. Back-splash is a backward shower leakage from the CsI calorimeter as shown in Fig. 1.8. The Back-splash has a correlation between its timing and hit position. This correlation

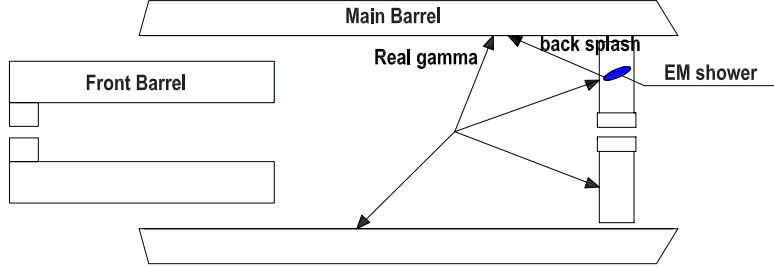


Figure 1.8: Schematic view of a shower and back-splash.

is different from that of K_L decay particles because the backsplash particles arrive later than the K_L decay particles. These correlations were observed in the E391a experiment as shown in Fig. 1.9.

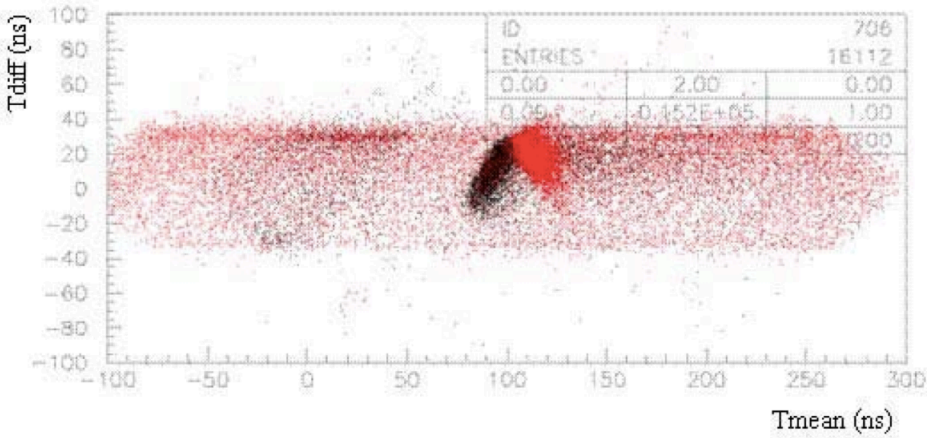


Figure 1.9: Distribution of the mean timing (horizontal axis) and the timing difference (vertical axis) of phototubes on the both ends of the MB taken in the E391a experiment [15]. The mean timing represents incident time of the gammas. The timing difference represents effective incident position considering the light propagating time in the MB module. The gammas from decays (black) and the back-splash (red) in events which had 4 gammas detected in the calorimeter were caused by the $K_L \rightarrow \pi^0 \pi^0 \pi^0$ and $K_L \rightarrow \pi^0 \pi^0$ modes, respectively. Timing of the back-splash is later for upstream hits.

In the E391a experiment, the signal timing was sometimes mis-measured because the timing was recorded only at the rising edge of pulses, and two pulses which came close

in time could not be separated. Therefore, tight separation could not be applied, and back-splash loss remained. If we can separate each pulse clearly, such mis-measurements can be reduced.

In the KOTO experiment, we planned to read out pulse shapes with waveform digitizers. By recording waveforms, we can measure multiple hit timings separately and apply a tight timing cut. There was another possibility to obtain a better timing decision. If we use material with better timing response, we can define accurate timing with narrower pulses.

1.4 Purpose and outline of this thesis

The purpose of this thesis is to design a new gamma veto detector called the Inner Barrel to be installed inside the Main Barrel and to make a path for its realization. To achieve this purpose, we had to solve various issues in the following process.

First, we studied the relation between the design and performance of gamma detecting with Monte Carlo simulation. Next, we investigated the production process for the realization. At the same time, we began data taking for the KOTO experiment without the Inner Barrel. We compared the measured performance of the Main Barrel and the performance estimated with Monte Carlo simulation. Finally, we estimated the total performance of the Inner Barrel.

The outline of this thesis is as follows. Apparatus of the KOTO experiment is described in Chapter 2. In Chapter 3 and 4, the effect of an idealistic detector and realistic detectors are compared. In Chapter 5, we describe the selection of detector elements and the decision of the construction method. We investigated the detector response using a realistic module and estimated the expected performance in Chapter 6. After that, in Chapter 7, we compared the simulated performance with the realistic performance taken in the early period of the KOTO experiment. We reestimated the expected number of signal and background events in Chapter 8. We discuss the experimental sensitivities and the possibility of further improvements, in Chapter 9. Finally, we conclude this thesis in Chapter 10.

Chapter 2

The KOTO experiment

The purpose of the KOTO experiment is to make the first observation of $K_L \rightarrow \pi^0 \nu \bar{\nu}$ decay. In this chapter, we first explain the methods to observe the $K_L \rightarrow \pi^0 \nu \bar{\nu}$ signal, and then describe experimental apparatus of the KOTO experiment.

Beforehand, we define the coordinate system. The origin is defined on the K_L beam at the upstream edge of the KOTO detector system. The z axis points in the K_L beam direction toward downstream. The y axis points vertically up, and the x axis points in the direction to satisfy the right-handed system. We adopt this coordinate system unless otherwise stated.

2.1 Method for signal identification

The $K_L \rightarrow \pi^0 \nu \bar{\nu}$ decay is identified by detecting only two gammas from the π^0 with a finite π^0 transverse momentum (P_T). The initial K_L is not observed because it is neutral. Two neutrinos are not observed because of their extremely small cross-section. The π^0 has a high P_T to balance momentum carried away by the missing neutrinos.

This identification, called “ $\pi^0 + \text{nothing}$ ”, is realized by a gamma calorimeter and hermetic veto detectors. The experiment is designed to detect events decayed in a certain z range, called decay region. The gamma calorimeter is located downstream of the region to observe K_L decays, and all other directions are covered by veto detectors.

The method to detect “ π^0 ” with P_T is described in Section 2.1.1, and the method to confirm ”nothing” is described in Section 2.1.2.

2.1.1 Signal reconstruction

The energies and hit positions of gammas were measured with the calorimeter as shown in Fig. 2.1. To clarify event kinematics, the following three conditions were assumed. First, the invariant mass of the two gammas agrees with the π^0 mass. Second, the vertex position is upstream of the calorimeter. Third, the π^0 decay point is on the z axis. The π^0 decay point is effectively the same as the K_L decay point because of the short π^0 life time ($(8.52 \pm 0.18) \times 10^{-17}$ sec [18]). To assume the π^0 to be on the z axis, the K_L beam has to be small.

The assumption on the invariant mass gives:

$$m_{\pi^0}^2 = 2E_1E_2(1 - \cos\theta), \quad (2.1)$$

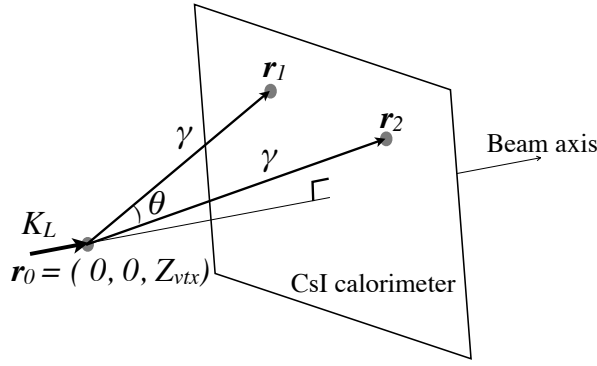


Figure 2.1: Schematic view of the π^0 reconstruction.

where E_1 and E_2 are the energies of the two gammas, and θ is the opening angle between the two gammas. The unknown variable θ is expressed as:

$$\cos \theta = \frac{(\mathbf{r}_1 - \mathbf{r}_0) \cdot (\mathbf{r}_2 - \mathbf{r}_0)}{|\mathbf{r}_1 - \mathbf{r}_0| |\mathbf{r}_2 - \mathbf{r}_0|}. \quad (2.2)$$

where $\mathbf{r}_0 = (0, 0, Z_{vtx})$ is the π^0 decay position, and \mathbf{r}_1 and \mathbf{r}_2 are the gamma hit positions on the calorimeter. After calculating the π^0 decay position Z_{vtx} with Eq. (2.1) and Eq. (2.2), the momentum \mathbf{p}_i of the i -th gamma and the $\pi^0 P_T$ are calculated as:

$$\mathbf{p}_i = (p_{ix}, p_{iy}, p_{iz}) \quad (2.3)$$

$$= E_i \frac{(\mathbf{r}_i - \mathbf{r}_0)}{|\mathbf{r}_i - \mathbf{r}_0|}, \quad (2.4)$$

$$P_T = \sqrt{(p_{1x} + p_{2x})^2 + (p_{1y} + p_{2y})^2}. \quad (2.5)$$

These Z_{vtx} and P_T are basic variables to identify signal events.

2.1.2 Background suppression

There are two background sources; one is K_L decay modes and the other is neutrons in the beam.

K_L decay background

Backgrounds from K_L decay modes are suppressed by detecting hits on veto detectors and extra hits on the CsI calorimeter. Major decay modes are listed in Table 2.1.

Charged modes such as the $K_L \rightarrow \pi^\pm e^\mp \nu$, $K_L \rightarrow \pi^\pm \mu^\mp \nu$, and $K_L \rightarrow \pi^+ \pi^- \pi^0$ are suppressed by vetoing charged particles. The former two decay modes, the $K_L \rightarrow \pi^\pm e^\mp \nu$ and $K_L \rightarrow \pi^\pm \mu^\mp \nu$, are mainly suppressed by Charged Veto (CV) counters [19] placed just upstream of the CsI calorimeter. The π^\pm and the lepton, e^\pm or μ^\pm , often create clusters on the calorimeter, and the clusters are distinguished from gamma clusters by signals in the CV. The $K_L \rightarrow \pi^\pm e^\mp \nu$ decay can become a background if a charge-exchange from π^- to π^0 and the e^+ annihilation occur, and the energy deposits by the π^- and e^+ are smaller than the detection threshold of CV.

Table 2.1: Branching ratios of K_L decay modes listed in the Particle Data Group [18] and of the $K_L \rightarrow \pi^0\nu\bar{\nu}$ decay predicted by the Standard Model. The value for $K_L \rightarrow \pi^0\nu\bar{\nu}$ decay is based on the SM prediction. Major four modes and background source decays are listed. Maximum momentum p_{max} is the kinematic limit of the π^0 momentum in the K_L rest frame. Visible particles in the final states of K_L decays are also listed. The number of visible particles is shown for charged particles (ch) and gammas (γ).

K_L decay modes	Branching ratio	p_{max} [MeV/c]	Visible particles
$K_L \rightarrow \pi^0\nu\bar{\nu}$	$(2.4 \pm 0.4) \times 10^{-11}$	231	2γ
$K_L \rightarrow \pi^\pm e^\mp\nu$	$(40.55 \pm 0.11)\%$	-	2ch
$K_L \rightarrow \pi^\pm \mu^\mp\nu$	$(27.04 \pm 0.07)\%$	-	2ch
$K_L \rightarrow \pi^0\pi^0\pi^0$	$(19.52 \pm 0.12)\%$	139	6γ
$K_L \rightarrow \pi^+\pi^-\pi^0$	$(12.54 \pm 0.05)\%$	133	2ch- 2γ
$K_L \rightarrow \pi^0\pi^0$	$(8.64 \pm 0.06) \times 10^{-4}$	209	4γ
$K_L \rightarrow \gamma\gamma$	$(5.47 \pm 0.04) \times 10^{-4}$	-	2γ

The $K_L \rightarrow \pi^+\pi^-\pi^0$ decay has two gammas in the final state. It can become background if both π^+ and π^- are not detected. In addition to detecting hits on the charged vetoes, selecting high P_T is effective to suppress the $K_L \rightarrow \pi^+\pi^-\pi^0$ background because its maximum P_T is lower than most of signal events.

One of neutral decay modes, $K_L \rightarrow \gamma\gamma$, also has two gammas but $P_T = 0$. Requiring high P_T suppresses this mode.

Other neutral decay modes such as $K_L \rightarrow \pi^0\pi^0\pi^0$ and $K_L \rightarrow \pi^0\pi^0$ have more than two gammas. Requiring high P_T for the π^0 's is not effective for the $K_L \rightarrow \pi^0\pi^0$ decays because P_T of $K_L \rightarrow \pi^0\pi^0$ decay is similar to that of signal mode; the maximum P_T is 209 MeV/c for the $K_L \rightarrow \pi^0\pi^0$ decay and 231 MeV/c for the signal mode. To suppress background from the $K_L \rightarrow \pi^0\pi^0$ decay whose branching ratio is 8 orders of magnitude larger than the branching ratio of the signal mode, the other two gammas should be detected with an inefficiency of $\mathcal{O}(10^{-4})$ for each. This is why we need gamma detectors with high detection efficiencies. The background level of the $K_L \rightarrow \pi^0\pi^0\pi^0$ decay is smaller than that of the $K_L \rightarrow \pi^0\pi^0$ decay because there are 4 extra gammas.

Neutron background

The main background in the E391a experiment was suspected to be caused by neutrons surrounding the beam core interacting with detector materials just upstream of the CsI calorimeter, for instance, the Charged Veto. The π^0 's and η 's were created in the interaction decayed into two gammas. Most events from π^0 could be rejected by a cut on the decay vertex position, but some events had wrong reconstructed vertexes if the energy was mis-measured. Events from η had wrong reconstructed vertex positions because the π^0 mass was assumed. For the KOTO experiment, these events were suppressed by developing new Charged Veto with less dead material [19].

Another possibility of neutron background is that neutrons directly hit the CsI calorimeter and make showers. If we cannot separate such hadronic showers from electromagnetic showers created by gammas, and if secondary neutron from the first interaction

makes another shower, the event can be a background. These hadronic showers are rejected by introducing CsI crystals with a small cross-section to observe the difference in shower shapes.

2.2 Beam line

The beam line for the KOTO experiment was constructed at the Hadron Beam Facility in the Japan Proton Accelerator Research Complex (J-PARC). Protons are accelerated up to 30 GeV through three accelerators: a linear accelerator (Linac), a 3 GeV Rapid Cycle Synchrotron (RCS), and the Main Ring, shown in Fig. 2.2.

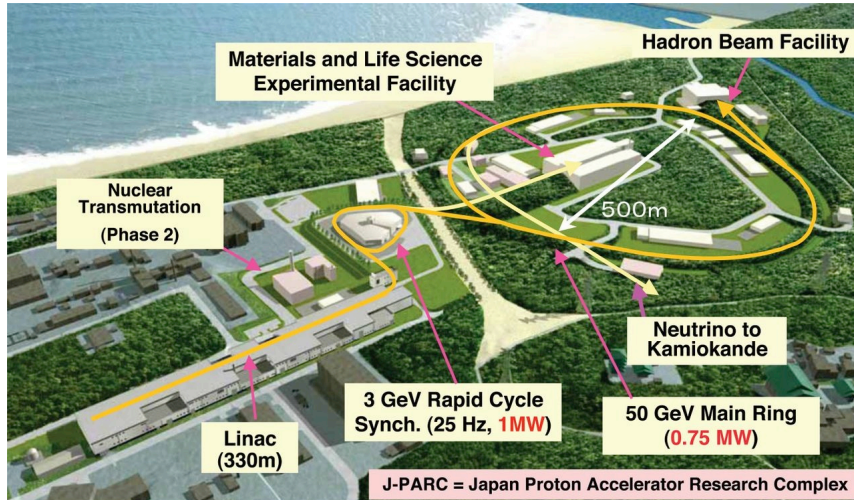


Figure 2.2: Bird eye's view of the J-PARC site [20].

Protons in the Main Ring were extracted to the Hadron Hall for 2 seconds per every 6 seconds in May 2013. This 2 seconds of the extraction period is called “spill”.

Beam parameters in the May 2013 run and the original parameters in the KOTO proposal are listed in Table 2.2.

Table 2.2: Beam parameters in May 2013 and in the original design.

	May2013	Design
Repetition cycle (seconds)	6.0	3.3
Spill length (seconds)	2.0	0.7
Intensity (protons per spill)	3×10^{13}	2.0×10^{14}

The extracted protons hit a production target called “T1 target” in the Hadron hall shown in Fig. 2.3. The T1 target for the run in May 2013 was made of gold.

A new neutral beam line for the KOTO experiment was built in the direction 16° from the primary proton beam line. The beam size is limited by two collimators as shown in Fig. 2.4. Although the number of K_L 's reaching the the KOTO detector is

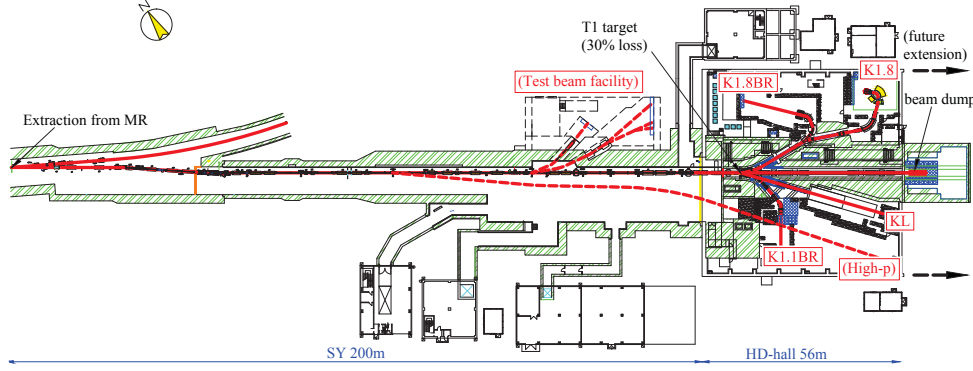


Figure 2.3: The proton transport line after extraction from the Main Ring and the layout of Hadron hall [20]. The K_L beam line is marked as "KL".

proportional to the beam size, the size should be small for the next two reasons. First, a small beam makes the beam hole on the calorimeter small to keep a high acceptance. Second, it keeps the resolutions of the $\pi^0 P_T$ and the π^0 decay vertex small as described in Section 2.1.

The distance between the T1 target and the upstream end of the KOTO detector ($z = 0$) is 21.5 m. This distance is long enough for K_s^0 (life time $c\tau = 2.7$ cm), Λ ($c\tau = 7.9$ cm) [18], and other short-lived hyperons to decay away. Charged particles such as electrons in the beam line are removed by a dipole magnet placed between the two collimators. At the upstream end of the KOTO detector, gammas, neutrons and K_L 's survive in the beam. In the Monte Carlo simulation, the ratio of the number of particles are $N_\gamma/N_{K_L} = 0.7$ and $N_n/N_{K_L} = 3.3$, where N_γ , N_n and N_{K_L} are the number of gammas, neutrons and K_L 's with momentum > 100 MeV/c, respectively.

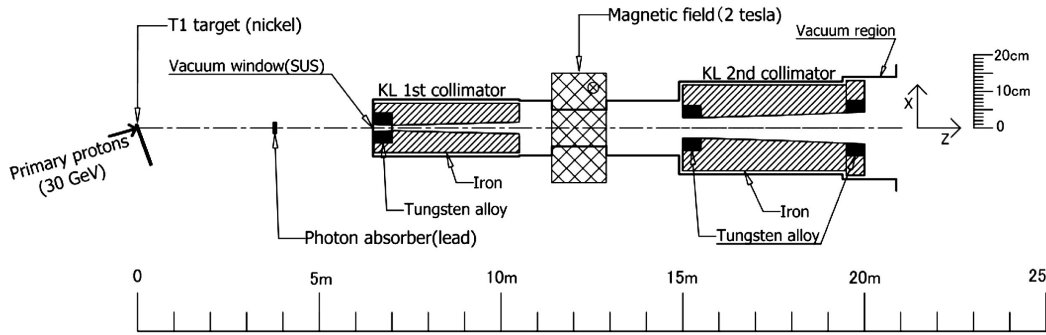


Figure 2.4: Plan view of the KL beam line [21]. Two stages of collimators are placed downstream of the T1 target, a sweeping magnet is located between them, and a photon absorber is located upstream of the collimators.

2.3 Detector

Next, we describe apparatus of the detectors for the KOTO experiment. The layout of detectors before installing the Inner Barrel is shown in Fig. 2.5.

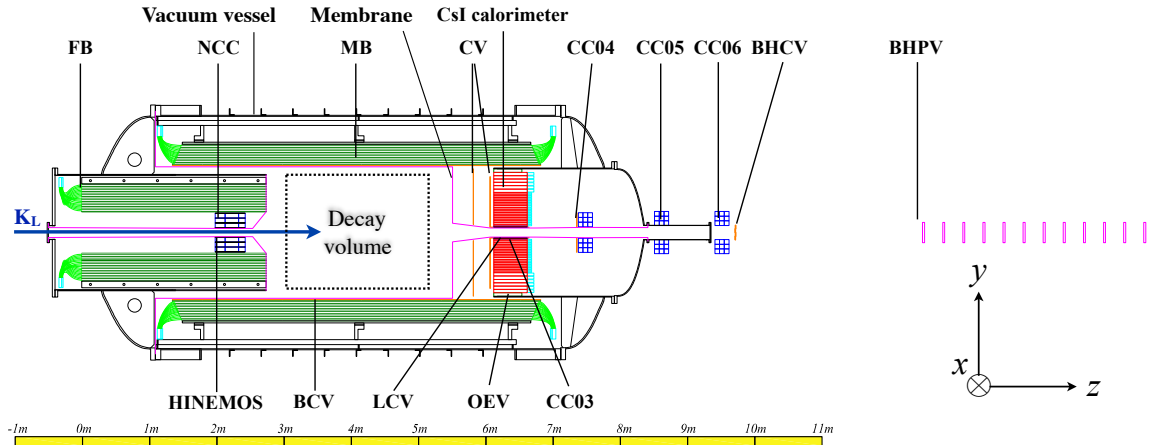


Figure 2.5: Setup of the KOTO detector. CsI calorimeter is the main detector and all others are veto detectors for photons or charged-particles. The photon veto detectors are Front Barrel (FB), Neutron Collar Counter (NCC), Main Barrel (MB), Outer Edge Veto (OEV), collar counters (CC03, CC04, CC05, CC06), and Beam Hole Photon Veto (BHPV). Charged-particle veto detectors are HINEMOS, Barrel Charged Veto (BCV), the Charged Veto (CV), Liner Charged Veto (LCV), and Beam Hole Charged Veto (BHCV). The most outside black line shows vacuum vessel. Multi-layer film called “membrane” is drawn with a pink line. Membrane separates a 5×10^{-5} Pa high vacuum region, and a 0.1 Pa low vacuum region where detectors in the vessel are placed.

The KOTO experiment was designed to observe K_L ’s decaying within a few meters upstream of the calorimeter by detecting two gammas with the calorimeter. Gammas escaping toward outside the calorimeter is detected with the Main Barrel.

The Front Barrel [22] was designed to veto events which decay upstream of the decay region. Gammas with large angles from the z axis in such events are detected by this gamma-veto detector. Neutron Collar Counter (NCC) is located inside the Front Barrel to detect decay particles with small angles from the z axis. The NCC also has a purpose of detecting beam halo neutrons.

Just as NCC, other detectors surrounding the beam called “collar counters”, CC03, CC04, CC05 and CC06 detect particles near the beam. Beam Hole Photon Veto (BHPV) [23] is placed in the beam at the most downstream part of the KOTO detector system. The BHPV detects decay particles remaining in the beam.

Detectors near the Main Barrel are closely related to the design of the Inner Barrel. For example, to evacuate the high vacuum region, a several-cm gap was required between the Front Barrel and Main Barrel. Also, the upstream-outer edge of the CsI calorimeter was closely related to the Inner Barrel because showers in this region leaked to multiple detectors and structures.

In the following, features of the CsI calorimeter, the Main Barrel, and other several

parts closely related to the Inner Barrel are described.

2.3.1 CsI calorimeter

The CsI calorimeter consists of two sizes of undoped CsI crystals as shown in Fig. 2.6. The central $1.2 \times 1.2 \text{ m}^2$ region consists of 2,240 “small crystals” with a $25 \times 25 \text{ mm}^2$ cross-section. Because the Moliere radius of CsI, 35.7 mm [18], is larger than the 25 mm, electro-magnetic showers spread in multiple crystals. We can thus judge from the shower shape whether the shower was made by one or multiple gammas, or by a neutron. The outer region consists of 476 “large crystals” with a $50 \times 50 \text{ mm}^2$ cross-section. The lengths of the both types of crystals are 500 mm ($27 X_0$).

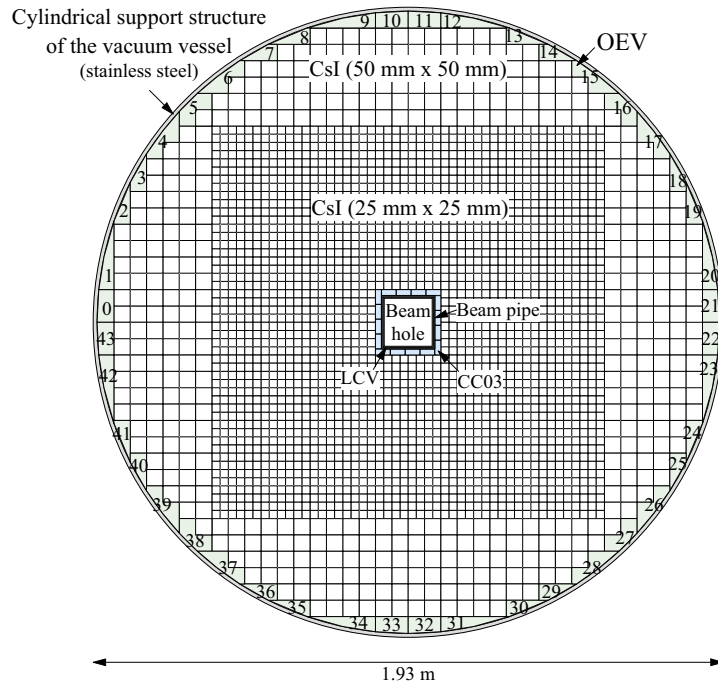


Figure 2.6: Cross-section of the CsI calorimeter and other detectors in the cylindrical support structure [24]. Modules with numbers labeled at the edge are the Outer Edge Veto (OEV).

2.3.2 Structures and detectors near the CsI calorimeter

The CsI crystals were stacked inside a 12-mm-thick stainless-steel cylinder. The gap between the cylinder and the crystals was filled with Outer Edge Veto (OEV). Outside the cylinder, there are structures to support Charged Veto (CV) and “CsI Cover” as shown in Fig. 2.7.

Outer Edge Veto (OEV)

The Outer Edge Veto (OEV) [24] consists of 44 counters with different cross-sectional shapes as shown in Fig. 2.6. All counters are sampling detectors made of 1.5 mm-

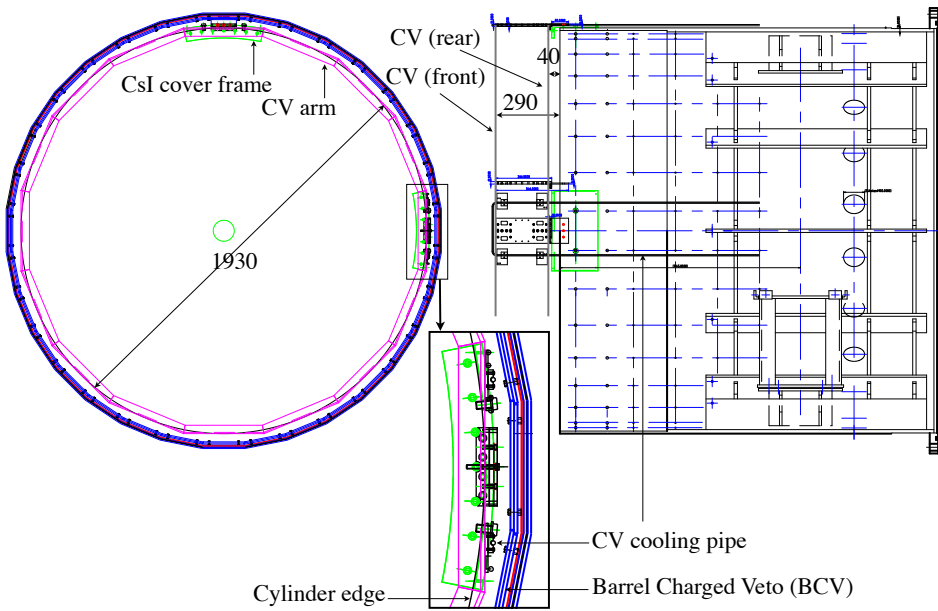


Figure 2.7: Front view (left) and side view (right) of cylinder.

thick lead and 5-mm-thick scintillator layers, and scintillation light is read out through wavelength-shifting fibers. The layers are placed parallel to the beam axis and the length along the beam direction is 420 mm.

Charged Veto (CV)

The Charged Veto [19] is located upstream of the CsI calorimeter. The detector consisted of 2 layers of 3-mm-thick plastic scintillators located 5 cm and 30 cm from the CsI calorimeter, respectively. Each layer is supported by aluminum support structure extended from the edge of the cylinder. The structure consists of 12-mm-thick flat aluminum plates called “CV arm” supporting the edge of total CV counters at 4 positions. The CV arm was attached to the frame of the CsI Cover.

CsI Cover

Just upstream of the CsI calorimeter is covered by a plate made of aluminum-honeycomb sandwiched between CFRP plates. It is designed to hold crystals in the cylinder in an event of strong earthquake. This structure called “CsI Cover” is supported by iron frames attached at the edge of the cylinder. The frame consists of 12-mm-thick L-shaped iron angles supporting around the edge of the CsI Cover.

2.3.3 Front Barrel

The Front Barrel [22] covers the upstream of the decay region. It consists of 16 modules of lead and scintillator sandwich detectors and is formed cylindrically in a 1.66 m diameter as shown in Fig. 2.8.

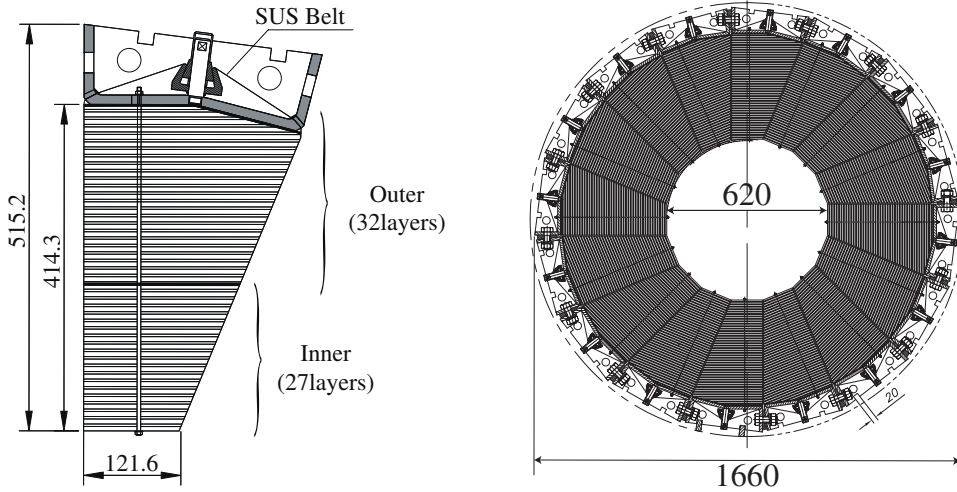


Figure 2.8: Cross-sections of the Front Barrel. Each module is connected together behind of the module [22].

2.3.4 Main Barrel

The Main Barrel [22] surrounds the decay region to detect extra particles from K_L decays. It consists of 32 modules of lead and scintillator sandwich detectors. The design parameters are listed in Table 2.3. The Main Barrel is formed cylindrically with a 2.0 m inner diameter. Each module is independently supported by the vacuum vessel as shown in Fig. 2.9.

A cross-sectional view of a module is shown in Fig. 2.10. The lead and scintillator layers are held together with 50 stud bolts and disc springs fixed on the backbone plate. The pressure at each spring is 300 kgf, so that the springs can compress a module with 15 tons in total. With this force, the friction between the layers kept the module shape when it is rotated.

Lead and scintillator plates are piled up alternately. All the scintillator layers are sandwiched between reflector sheets. The scintillator is made of MS-resin-based (80% polystyrene + 20% meta-acrylate) plastic scintillator [26] developed for the Main Barrel construction. MS-resin has a tensile strength 1.5 times larger than commercial scintillator made of polystyrene [26, 27].

The signal in the scintillator is read out from the wave length shifting (WLS) fibers glued in grooves of the scintillator. The layout of a layer is shown in Fig. 2.11. The WLS fiber is multi-clad type Y11-M made by Kuraray [28]. The fibers were glued by NORLAND Optical Adhesive NOA61. Reflector sheets are Toray TiO₂ PET. The signal is read out by Hamamatsu R329-EGP PMTs [29, 30]. These materials are described for the Inner Barrel in Chapter 5.

The Main Barrel was constructed for the E391a experiment in 2003. We reuse the detector for the KOTO experiment. The Main Barrel modules were removed from the vacuum vessel and transferred to J-PARC, and then reassembled in the Hadron Hall in 2012. The air temperature around the modules was controlled during safekeeping and reassembling processes to prevent deformation. Light yield measured just before the first assembling for the E391a experiment with cosmic ray is shown in Fig. 2.12. Light

Table 2.3: The design parameters of the barrel detector [22]. (* Confirmed by photo taken in 2012.)

	Main Barrel
Length (m)	5.5
Outer diameter (m)	2.8
Inner diameter (m)	2.0
No. of modules	32
Readout units / module	2 both ends
No. of PMTs	128 (32×4)
No. of scintillator layers	15(inner) + 30(outer)
No. of lead layers	15(inner) + 29(outer)*
Thickness of scintillator (mm)	5
Thickness of lead (mm)	1 (inner), 2(outer)
Thickness (X_0)	14.0
Module weight (kg)	1500
Front plate material and thickness (mm)	SUS 3.0
Back bone material and thickness (mm)	SUS 19.3(thin part) 28.6(thick part)

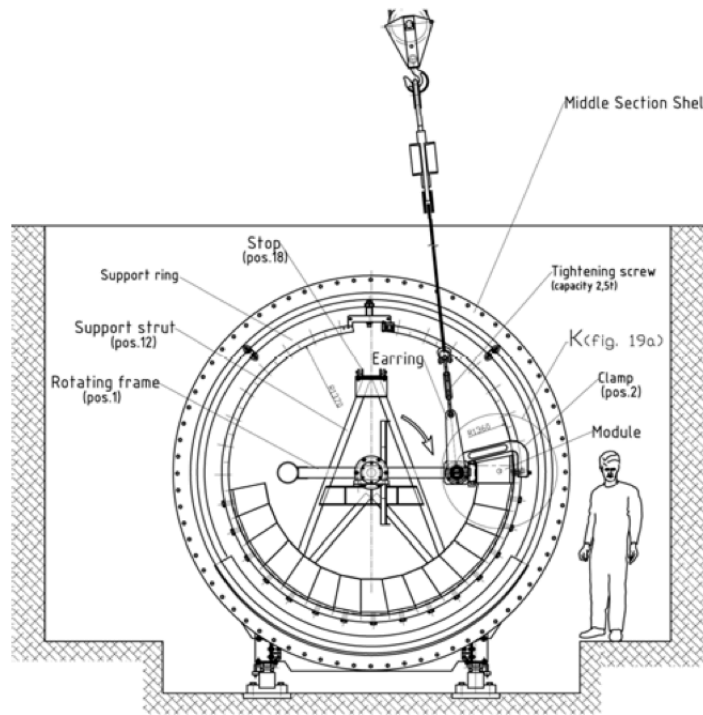


Figure 2.9: Cross-section of the Main Barrel under construction. Each module is supported independently by three support rings aligned in the vacuum vessel. The support ring and the backbone plate are connected by 36-mm-diameter bolts [25].

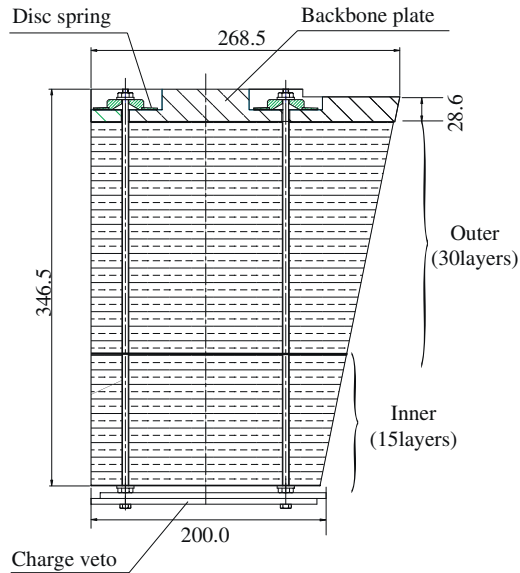


Figure 2.10: Cross-section of a module of Main Barrel [22]. The 5-mm-diameter 50 stud bolts fixed the laminate structure covering layers to the backbone plate.

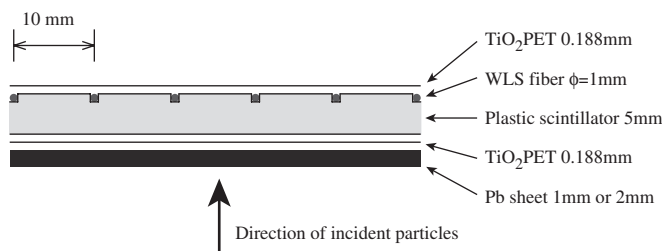


Figure 2.11: Cross-section of a layer of the Main Barrel with WLS fiber setting and light shields. The grooves for the WLS fibers have a cross-section of 1.2 mm (width) \times 1.3 mm (depth).

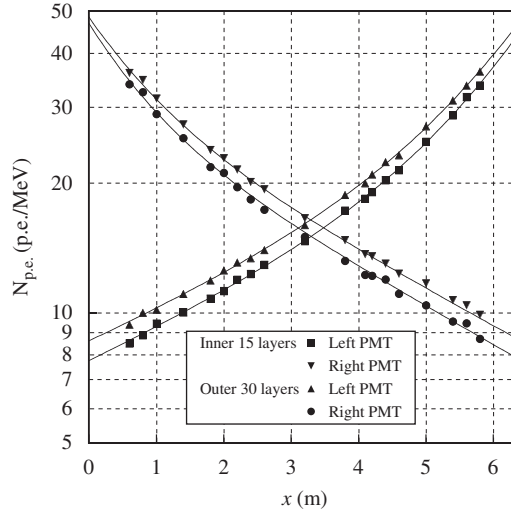


Figure 2.12: Position dependence of the light yield for the Main Barrel. The x is the distance from the photo-cathode of left side PMTs [22].

yield at the center of the detector was 14.7 p.e./MeV, and 11 p.e./MeV at 1.5 m from the center which was just downstream of the Front Barrel and just upstream of the CsI calorimeter. Result of measurements a decade later, during and after reassembling for the KOTO experiment, is described in Chapter 6.

2.4 Readout system

Most of the KOTO detectors including the CsI calorimeter and the Main Barrel are read out by Photo Multiplier Tubes (PMTs). These analog signals are digitized by Flash ADCs (FADCs) in the KOTO data acquisition system. Only high rate detectors such as BHCV and BHPV use 12-bit dynamic range and 500-MHz-sampling FADCs. Other detectors use 14-bit dynamic range and 125-MHz-sampling FADCs. Pulse heights of analog signal are stored in pipeline buffers inside Field Programmable Gate Arrays (FPGAs) in the FADCs.

The 125-MHz FADC had a 10-pole low-pass Bessel filter as shown in Fig. 2.13. The Bessel filter widened the waveform to increase the number of sampling points from only 1 or 2 without the filter to about 8 with the filter. With this scheme, we achieved a 0.3 ns timing resolution at 300 MeV deposit in a CsI crystal with the 8 ns samplings [32].

The trigger system to select events for offline analysis consisted of three steps.

The Level 1 trigger system made a decision based on the total energy detected in each detector. The Level 1 trigger system received the sum of ADC counts in each FADC module every 8 ns, and used the sums to select events with large total energy deposit in the CsI calorimeter and small energy in the veto detectors.

The Level 2 trigger system calculated the Center Of Energy (COE), which is the energy-weighted-average position of all the CsI crystals for the calculation. Because $K_L \rightarrow \pi^0 \nu \bar{\nu}$ signal has a large P_T , the COE should be away from the beam center.

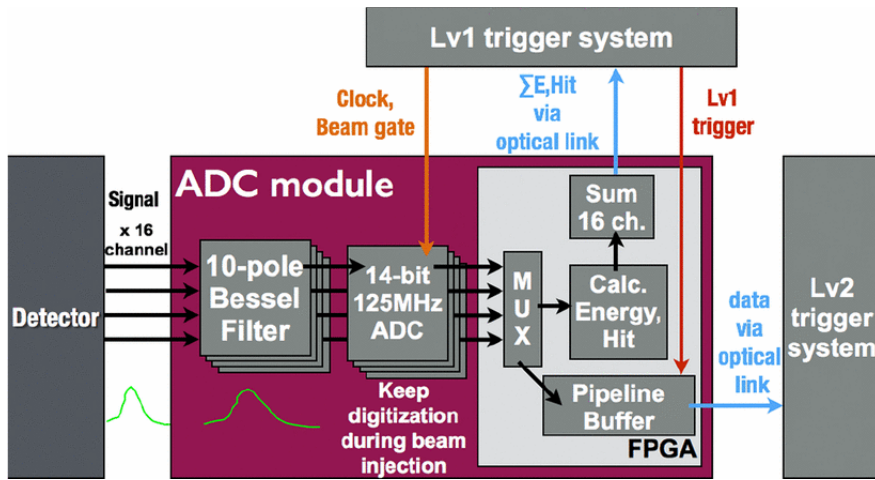


Figure 2.13: Schematic view of a 14-bit 125-MHz ADC module with a 10-pole Bessel filter in the KOTO data acquisition system [31].

The Level 3 trigger system only rearranged the array of data and compressed the data without selecting events. In the future, the Level 3 trigger system will be used to select events by analyzing data online.

Chapter 3

Performance of the idealistic Inner Barrel

As described in Chapter 1, there are two motivations to install the Inner Barrel: background reduction and acceptance increase. We will investigate the idealistic condition in this chapter for both motivations to know the ability of this detector idea.

We first explain the tools to examine the detector performance in Section 3.1.

The primary motivation was the background reduction. To realize more sensitive detector than the original design written in the KOTO proposal, we clarify the background sources in the original detector plan in Section 3.2. In addition, energy threshold dependence of the number of background events is described in Section 3.3. After that, we discuss extent of further improvements regardless of reality in Section 3.4. In the estimation of the extent, we assume the new detector to be made of idealistic material at an ideal position.

We consider the second motivation, acceptance increase, in the latter half of this chapter. Energy threshold is related not only to background reduction but also to acceptance increase. The acceptance increase is also affected by other conditions. A strategy for acceptance increase will be described in Section 3.5.

Detail of realistic detector condition for both two motivations will be discussed in Chapter 4.

3.1 Simulation study method

We used Monte Carlo simulation to study the detector performance.

As a background source, we considered only the $K_L \rightarrow \pi^0\pi^0$ decay mode. Other background sources were neglected under the ideal condition that other detectors were able to suppress other backgrounds. As for the acceptance loss, we only considered the loss caused by the Inner Barrel.

The estimation of the number of background events was separated in three steps. The first step was the $K_L \rightarrow \pi^0\pi^0$ simulation to determine the feature of π^0 decay gammas. Incident energies and angles of gammas were recorded. These two parameters were used to decide particle detection efficiencies. The second step was simulation of gamma with monochromatic energy and fixed incident angle. The purpose of the gamma simulation was to understand detector response with high statistics. The last step was

the estimation of the number of the $K_L \rightarrow \pi^0\pi^0$ background events by applying obtained inefficiencies.

In this section, we explain the simulation tools and methods, and describe features of the $K_L \rightarrow \pi^0\pi^0$ simulation and the gamma simulation.

3.1.1 Monte Carlo method

For the KOTO experiment, we mainly adopted the Geant4 package for Monte Carlo simulation. It was a toolkit for the simulation of the passage of particles through matter. Interaction with the material was calculated at each short flight distance step by step. Interaction processes followed physics models called physics list. The KOTO and this thesis mainly adopted QGSP_BERT physics list. It includes Bertini cascade[33] for protons, neutrons, pions and Kaons below 10 GeV in addition to basic hadronic interactions led by quark gluon string model. We expect that it describes physics phenomena well in the KOTO's energy region which is below a few GeV.

The KOTO used two methods to estimate interactions between incident particles and detectors. These were called Full simulation and Fast simulation.

Full simulation is an orthodox method in Geant4. Each interaction is calculated step by step. The cross-section of each process decides the probability of the space-time length to the next step. At each interacting step, Geant4 records the energy transferred to the material, and the time and position of the interaction. It also calculates three dimensional momentum of each particle. After all tracking particles lost their kinetic energies or passed through the material, we could determine the detector response. We summed up the transferred energies as a deposit energy. We also defined the timing of the energy deposit by taking the mean of the recorded timings weighted by the transferred energy. If we decided a timing window, the steps outside the window were excluded from the energy and timing calculations.

Fast simulation is a method to estimate the background quickly with high statistics. In contrast to the Full simulation which simulates the interactions step by step, we stopped the decay particle at the surface of the detector and calculated the background probability using the detection inefficiency for each particle.

In the Fast simulation, the number of background events N is calculated by summing the probability W that the event would be background:

$$N = \sum_i^{\text{evt}} W. \quad (3.1)$$

The probability W is calculated as:

$$W = \sum_l^{\text{pattern}} \left(\prod_k^{\text{cluster}} C_k \prod_j^{\text{veto.par.}} I_j \right). \quad (3.2)$$

Here, C_k is the probability that the k -th gamma that should be observed formed a cluster. The I_j is the probability that other j -th gamma was not detected. The l runs through patterns for detecting two clusters in the calorimeter. If $n(> 2)$ gammas hit the

calorimeter, $(3^n - 2^{n+1} + 1)/2$ patterns ¹ exist for detecting two clusters. The $n - 2$ extra gammas are either fused with other clusters, or not observed due to detector inefficiency. The probability of fusing is included in C_k , and the probability of the inefficiency is included in I_j .

We used Fast simulation to study the $K_L \rightarrow \pi^0\pi^0$ background. The inefficiency of barrel detectors for monochromatic gammas were prepared with Full simulation.

3.1.2 $K_L \rightarrow \pi^0\pi^0$ simulation

To design the Inner Barrel, we focus on the $K_L \rightarrow \pi^0\pi^0$ decay which is the main source background. The K_L 's were generated at 20 m downstream of the T1 target. The x-y position and the momentum of the K_L 's are shown in Fig. 3.1.

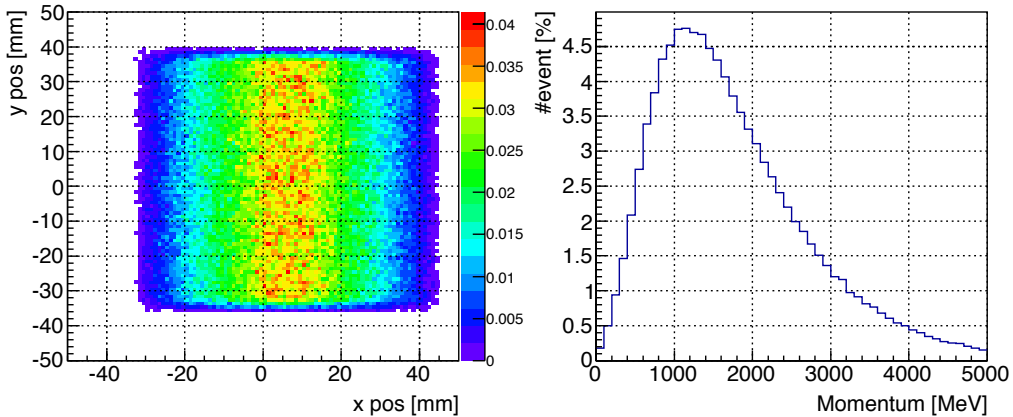


Figure 3.1: The K_L beam profile and the K_L momentum distribution at the 20 m downstream of the T1 target. Events are generated in Geant4 MC.

In the $K_L \rightarrow \pi^0\pi^0$ simulation, we used Fast simulation to clarify the features of gammas hitting the Main Barrel. Figure 3.2 shows the correlation of the energies of the two missing gammas for events weighted by the weight W in Eq. (3.2) prepared for the barrel detectors designed in the KOTO proposal.

Incident energy and angle distribution of decay gammas entering the barrel detectors is shown in Fig. 3.3 (left). Applying the weight W in Eq. (3.2) to each photon, we get Fig. 3.3 (right). Here, the W was taken from the inefficiency function in the proposal in which a 5 X_0 -thick barrel detector was placed outside the Main Barrel. These plots include events with more than one gammas hitting the Main Barrel. To see the effect of the gammas on the number of the background events, the weight of each gamma in the right plot was changed to W/n where n is the number of particles hitting the Main Barrel.

¹Gammas hitting the calorimeter and making two clusters are categorized into three cases: the gamma included in the first cluster, included in the second cluster, and vetoed. There are 3^n patterns. In the patterns, 3 patterns that all gammas are in one case, $2(2^n - 2)$ patterns that all gammas are in one cluster and vetoed are taken off. In addition, patterns are divided by 2 because two clusters are exchangeable. The $(3^n - 3 - 2(2^n - 2))/2 = (3^n - 2^{n+1} + 1)/2$ patterns thus exist.

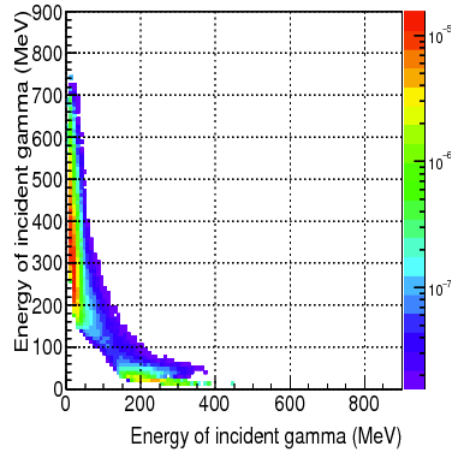


Figure 3.2: Energy distribution of the two missing gammas in even-pairing background, which were generated in Geant4 MC.

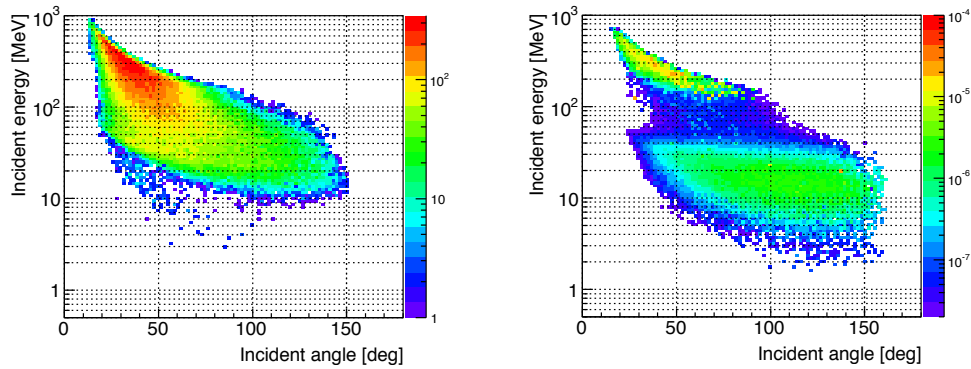


Figure 3.3: The number of gammas hitting the Main Barrel produced by the $K_L \rightarrow \pi^0\pi^0$ simulation (left). The number of gammas missing at the barrel detectors in the KOTO proposal (right). The number was estimated from the $K_L \rightarrow \pi^0\pi^0$ simulation. The x axis shows the angle θ of incident gamma, and the y axis shows incident energy. The θ is defined as the angle between gamma momentum and the z axis.

3.1.3 Monochromatic gamma simulation

Inefficiency function was prepared with the monochromatic gamma simulation at several energies and incident angles. Gammas were generated from the beam center. The hit position was set at midstream of the Main Barrel. For the Inner Barrel, designs which has an azimuthal angle ϕ dependence, gammas were generated randomly in ϕ . For the Inner Barrel designs which has a z position dependence, gammas were injected uniformly in z .

Generated gammas were injected in the sample detector and were counted as inefficient events if their deposit energies were below a detection threshold. The fraction of the inefficient events was defined as the inefficiency. Inefficiency function $I(E, \theta)$ is calculated by interpolating between the inefficiencies at near E and θ points, I_{xy} , as:

$$I(E, \theta) = \exp\{(\log I_l)(1 - \epsilon) + (\log I_h)\epsilon\} \quad (3.3)$$

$$I_x(\theta) = \exp\{(\log I_{xu})(1 - t) + (\log I_{xo})t\} \quad (3.4)$$

$$\epsilon = (\log E - \log E_l)/(\log E_h - \log E_l) \quad (3.5)$$

$$t = (\theta - \theta_u)/(\theta_o - \theta_u) \quad (3.6)$$

where $E_l < E < E_h$, $\theta_u < \theta < \theta_o$, $x = l$ or h , and $y = u$ or d . Figure 3.4 (left) shows the inefficiency function $I(E, \theta)$ of the Main Barrel.

When we used the inefficiency function of the Main Barrel alone instead of the inefficiency of the barrel detectors in the proposal design, the incident energy and angle distribution of missing gamma at the Main Barrel without the Inner Barrel was estimated as shown in Fig. 3.4 (right).

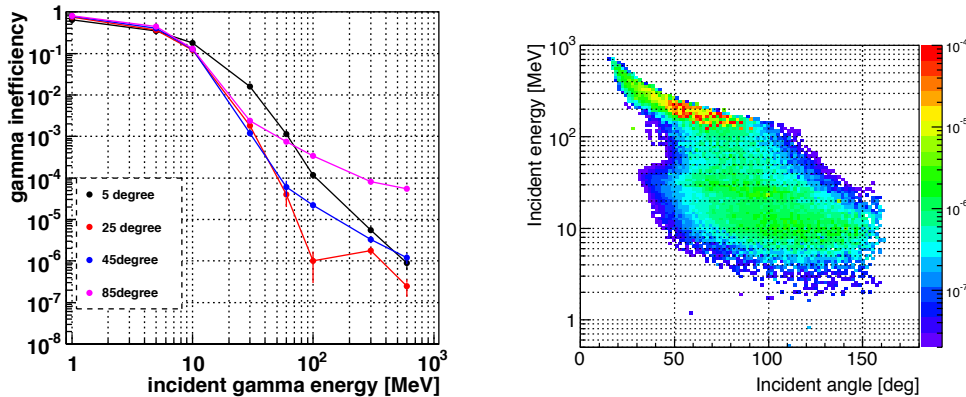


Figure 3.4: Left: Inefficiencies of the Main Barrel. Energy threshold was set to 0.5 MeV. Right: The number of gammas missing at the Main Barrel with inefficiencies in left figure. The number was estimated from the $K_L \rightarrow \pi^0\pi^0$ simulation. The x axis in the right figure shows the angle θ of incident gamma, and the y axis shows incident energy. The θ is defined as the angle between gamma momentum and the z axis.

3.2 Cause of inefficiency and features of background gamma with the original detector design

From the plots in Fig. 3.3 and Fig. 3.4, we understood the features of the incident gammas and the background source gammas, and the difference between them.

Most incident gammas have high energies (> 100 MeV) and shallow incident angles as shown in Fig. 3.3 (left). This feature means that most of remaining gammas were not missed by punch thoughts. Even if we add a thicker detector than the detector designed in the KOTO proposal to avoid punch thoughts, the actual effect on the number of background events should be small.

This possibility is also understandable by comparing the distribution of E and θ of missing gammas for the proposal design shown in Fig. 3.3 (right) and that for the Main Barrel shown in Fig. 3.4 (right). The additional 5 X_0 detector outside the Main Barrel only suppressed the missing gammas in the region $100 \sim 200$ MeV and $50^\circ \sim 90^\circ$. Remaining gammas distributed in $0.1 \sim 1$ GeV range have a correlation between incident energy and angle, and gammas distributed in $5 \sim 50$ MeV range have no correlation. This distribution suggested that the further improvement is necessary to reduce photo-nuclear interaction and sampling effect.

These feature of the remaining background source gammas were caused by two reasons.

One is the value of the inefficiency itself. The inefficiency of low energy gamma is relatively high, so that low energy gammas become a source of background.

The other is the combination of two gammas. Both two extra gammas in the $\pi^0\pi^0$ background often hit the barrel detectors. In this case, one gamma has high energy and shallow angle, and the other has low energy. Because the low energy gammas are likely to be missed, accompanying high energy gamma can show the high total background probability.

Figure 3.5 shows the inefficiency due to each source as a function of incident energy for barrel detectors in the proposal. The main contribution in low energy region was sampling effect. The energy range in which sampling effect is the main source depends on the gamma incident angle. In high energy region, the inefficiency for the gammas were dominated by punch through in large angle region, and by photo-nuclear interaction in small angle region.

The inefficiency due to photo-nuclear interaction is on the order of $< 10^{-5}$. The cross-section of photo-nuclear interaction is $\mathcal{O}(10^{-3}) \sim \mathcal{O}(10^{-4})$ of electromagnetic interaction, and Geant4 Monte Carlo (MC) reproduces the expected cross-section. The inefficiency in high energy region was smaller than not only the creation ratio reproduced in Geant4 but also inefficiency in an experimental data for photo-nuclear interaction measured in the ES171 experiment [17]. We simulated the inefficiency of the detector setup of the ES171 experiment with Geant4 because the detector was smaller than the barrel detectors, and the result was consistent with the data. It thus means that small photo-nuclear inefficiency in the barrel detectors is explained by the large size of the detector.

The mechanism of small inefficiency due to photo-nuclear interaction in a large size detector is understandable. As shown in Fig. 3.6, secondary neutrons created from incident gamma interact with detector material according to their interaction length and kick out charged particles. Large detector enables the secondary neutrons to create further interactions.

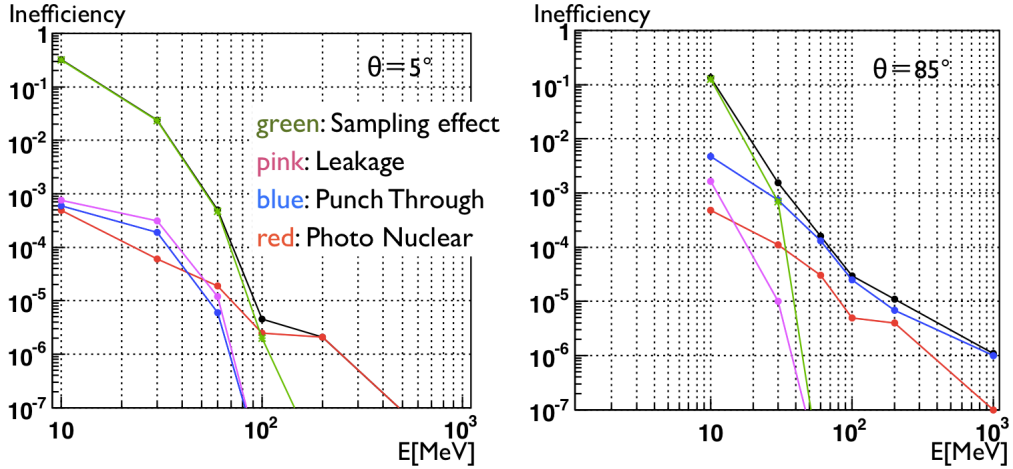


Figure 3.5: The inefficiency of the barrel detectors in proposal is shown for each source as a function of incident gamma energy. Each color shows the sources as; black: total inefficiency, blue: punch through in which a gamma deposits the full energy on the virtual detector outside the barrel detectors, pink: leakage in which a gamma deposits enough energy on the virtual upstream or downstream detector, red: photo-nuclear in which a event includes neutron in secondary particles in the rest events, and green: sampling effect which is the rest events.

Moreover, dead material in the detector such as absorber and support structure stops charged particles created by photo-nuclear interaction immediately. The fraction of inefficiency due to photo-nuclear interaction is thus sensitive to the dead material. Relation between the amount of dead material and the number of background events will be discussed in Chapter 4.

3.3 Energy threshold dependence of background reduction

As described in previous section, there were low energy deposit events caused by photo-nuclear interaction. The number of the background events is thus expected to have a threshold dependence. We calculated the inefficiencies of the barrel detectors designed in the KOTO proposal at several thresholds and applied the inefficiencies to the $\pi^0\pi^0$ background estimation. The result is shown in Fig. 3.7. As also described in previous section, the ability to detect low energy charged particle should be different between the amount of dead material in the detector. We will discuss the detail in Chapter 4 after candidate structures are listed.

3.4 Extent of further improvement for background reduction

As described in previous sections, a fully active detector placed inside the Main Barrel should improve the detection efficiency for most gammas. As an idealistic active and thick material, we considered a simple cylindrical detector made of CsI with a 750 mm

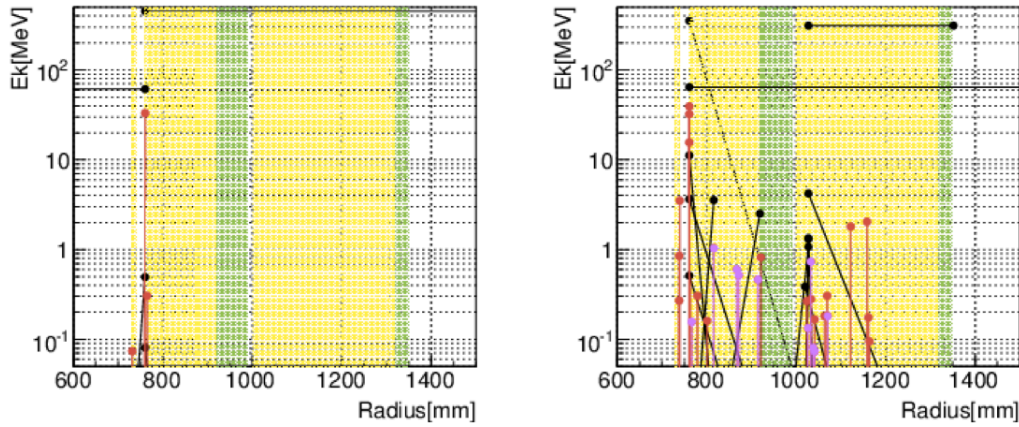


Figure 3.6: Kinetic energies of secondary particles in an event. The secondary particles which deposit the energy under (left) or over (right) threshold are created by photo-nuclear interaction. The X axis shows the radius from the beam center and the Y axis shows deposit energy of secondary particles. The barrel detectors were located from 750 mm to 1350 mm in radius. Position of the detector and structure are colored by yellow and green, respectively. Incident energy and angle of generated gamma were 600 MeV and 45 degree. Points connected with a line show initial to final conditions of the particles created by the photo-nuclear and the secondary interactions. Each color of the line shows the kind of particle, neutron, proton and heavy ions drawn in black, red, and magenta, respectively. The case without (with) secondary neutron interaction generates small (large) number of charged particle as shown in left (right) plot. Although some charged particles only interact in absorber, the case of many charged particles tends to be over threshold.

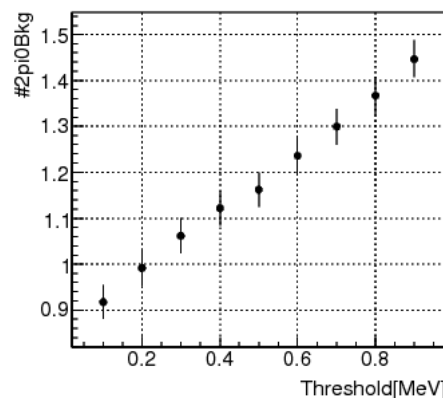


Figure 3.7: The number of the $\pi^0\pi^0$ background events as a function of energy threshold for the barrel detectors designed in the KOTO proposal.

inner radius. We made an inefficiency functions for a combination of the cylindrical CsI and Main Barrel.

Figure 3.8 shows the number of the $\pi^0\pi^0$ background events as a function of the thickness of the CsI cylinder. The $\pi^0\pi^0$ background is suppressed to the level of background

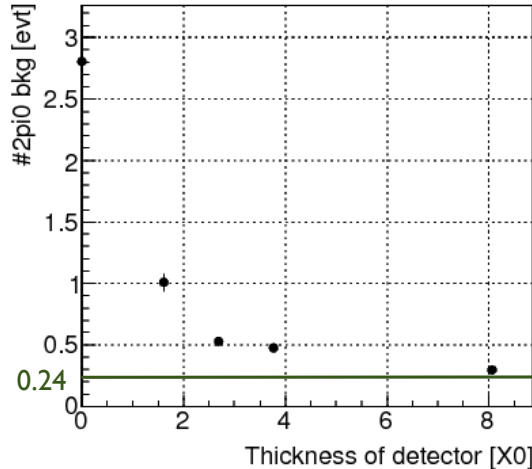


Figure 3.8: The number of the $\pi^0\pi^0$ background events shown as a function of CsI cylinder thickness. Green line shows the $\pi^0\pi^0$ background due to other detectors. Energy threshold on the CsI cylinder was set to 0.5 MeV.

caused by other detectors, if the CsI thickness is $8 X_0$, and twice the level with $3 \sim 4 X_0$. These background events are also affected by the performance of other detectors because in some events, one of extra gammas hit other detectors. Around 3 or $4 X_0$ thickness is a target because the improvements of other detectors become more effective for a further background reduction.

3.5 Strategy for acceptance recovery

Signal acceptance loss was caused by back splash events and beam accidental events, as mentioned in Chapter 1.

3.5.1 Comparison between back splash and $\pi^0\pi^0$ background

Backsplash is a backward shower leakage from the CsI calorimeter. Most of backsplash particles are low energy gammas, and some of them hit the Main Barrel. Hit timing and position of the backsplash particles on the Main Barrel are different from those of $\pi^0\pi^0$ background events as shown in Fig. 3.9. The deposit energy distributions are also different as shown in Fig. 3.10.

We can separate gammas from backsplash and the $\pi^0\pi^0$ background with two methods. One is a cut on the timing and z position correlation, called t-z cut, and the other is a cut on energy. With the t-z cut at the mean of timing and z position relation (t-z line) of the back splash, we could recover half of the backsplash events with late timing with narrower veto window such as the region $t < -0.00320z + 21.2$ in Fig. 3.10. One

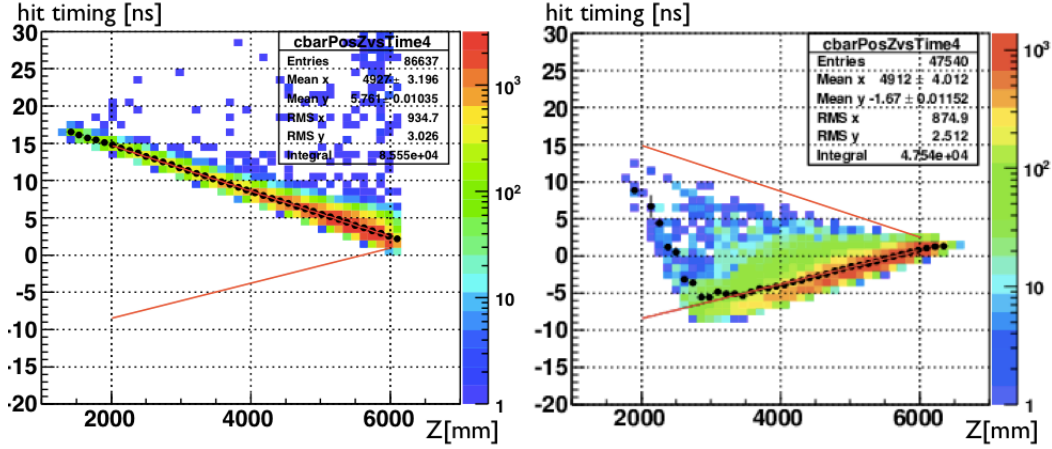


Figure 3.9: The Main Barrel hit timing and z position distribution of backsplash events (left) and the $\pi^0\pi^0$ background events (right) in MC. The position $Z=6148$ mm corresponds to the surface of the CsI calorimeter. The red lines show the mean of the timing and z position relation (t - z line) of back splash events ($t = -0.00320z + 21.2$) and that of the $\pi^0\pi^0$ background events ($t = 0.00231z - 12.8$).

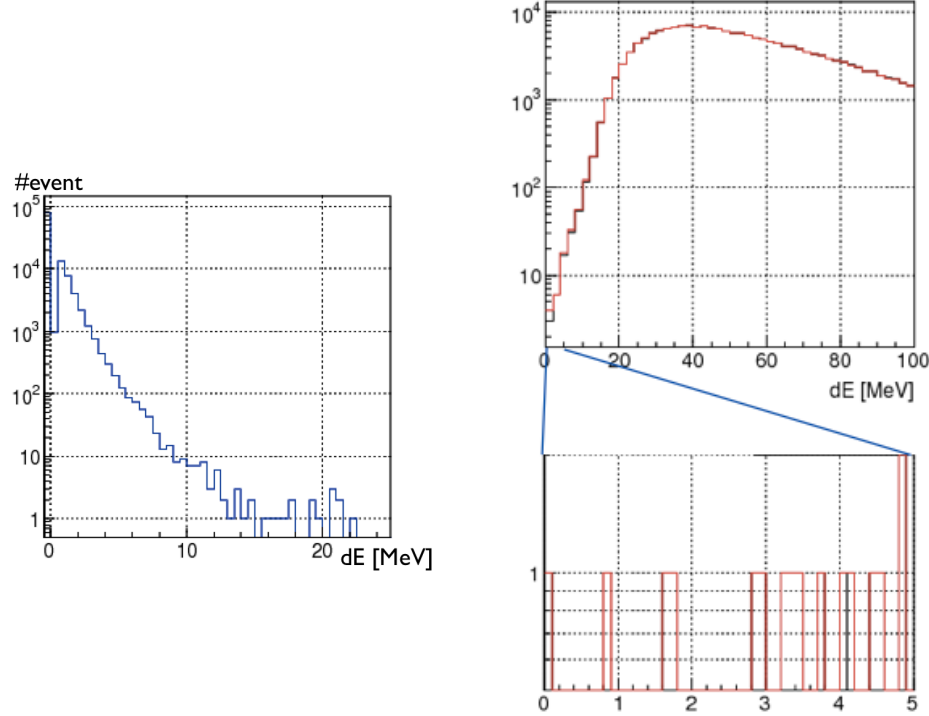


Figure 3.10: Deposit energy distribution in Main Barrel for back splash events (left) and $\pi^0\pi^0$ background events (right) obtained with the full simulation. A total 10^5 signal events were generated for the left plot, and $6 \times 10^8 \pi^0\pi^0$ events were generated for the right plot. The $\pi^0\pi^0$ plot shows remaining events after event selection.

concern of this cut was small amount of background events seep outside of veto window due to timing resolution which will be considered in following chapters.

About the cut on energy, the number of the $\pi^0\pi^0$ background events at each energy threshold depends on the amount of dead material because deposit energy in photo-nuclear interaction is sensitive to the material.

We will maximize the ratio of signal over background events. Detail of the ratio will be discussed in Chapter 4.

3.5.2 Reduction of effect of beam accidental activity

Some particles in high intensity beam can hit detectors accidentally within the veto timing window. Such possibility is reduced if the width of window is narrowed. On the other hand, if the veto timing window is narrower than the timing resolution of the veto detector, the number of background events will increase. The smaller timing resolution enables the narrower veto timing window. The hit timing distribution of the barrel detectors without timing resolution is shown in Figure 3.11. The RMS (root mean

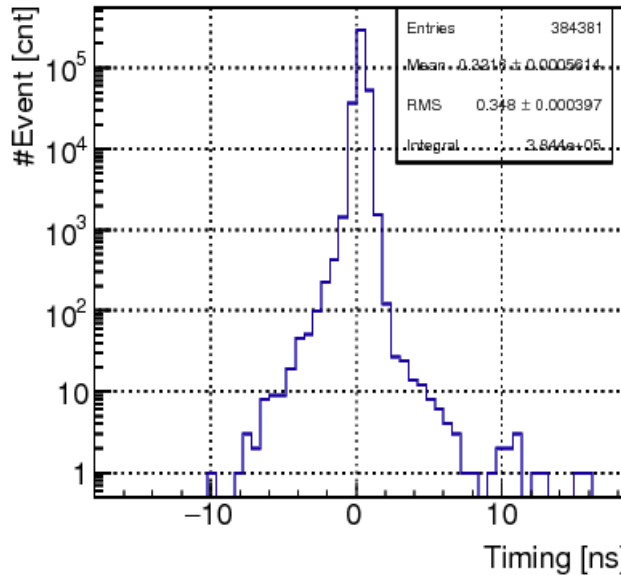


Figure 3.11: Timing distribution hitting the barrel detectors without timing resolution caused by timing response of the Main Barrel.

square) was 0.35 ns. The timing resolution thus does not have to be lower than this. Estimation with candidate detector response will be described in the next chapter.

Chapter 4

Design of detector and requirements for materials

As described in Chapter 3, an ideal detector placed inside the Main Barrel reduced the number of the $K_L \rightarrow \pi^0\pi^0$ background events more than the detector planned in the proposal.

However, realistic conditions such as geometry, cost, chemical characteristics of detector material, engineering limitation to support detector, should be taken into account. In addition, good timing resolution was also required for a veto detector.

This chapter describes the strategy we took to design a new Inner Barrel detector.

4.1 Strategy for designing the detector

At first, we decide material of the detector in Section 4.2 to design the detector. Criteria of the materials are decided based on the detector requirements as follows, and each criterion is investigated in further following sections.

As described in Chapter 3, the new detector had to satisfy the requirements on the particle interaction with detector material, the energy threshold dependence, and the timing resolution. The interaction is evaluated with the number of the $K_L \rightarrow \pi^0\pi^0$ background events in Section 4.3 and Section 4.4. The threshold dependence is studied in Section 4.5 after the detector candidate is designed. The threshold is closely related to the light yield, and how we consider the requirement on the light yield will be discussed in Section 4.6. Relation between timing resolution and timing response of the Inner Barrel is also discussed in Section 4.6. The relation between timing resolution and the acceptance recoveries will be described in Section 4.7.

In addition to satisfying these detector requirements, we had to consider some limitations.

One limitation was the geometry of the detectors. Inner radius of the Inner Barrel calculated from the gamma path had to be > 750 mm because the path of gammas hitting < 850 mm radius on the CsI calorimeter should not be blocked. The thickness of the detector including its support structure was thus limited to within 250 mm in a 750 \sim 1000 mm radial space. To make the detector 5 X_0 thick, the radiation length of its material had to be less than 50 mm.

Another limitation was the sampling ratio and the amount of dead material. The

Inner Barrel should be more sensitive than the Main Barrel, because the Inner Barrel covers the inner side of the Main Barrel. At least, lower or same ratio of dead material was required.

From the above, the major criteria to select the detector materials were light yield, timing response, and radiation length.

4.2 Selection of detector type

As described in Section 4.1, possible materials should be selected based on light yield, timing response, radiation length, and limitations described above.

One possibility was inorganic scintillating crystal. Properties of inorganic crystals are shown in Table 4.1.

Table 4.1: Properties of crystal [18] about decay time (D.T.), light yield (L.Y.), wave length (W.L.), radiation length and appropriateness (bottleneck compared to CsI (pure)) for the new Barrel detector. The light yield shows relative light output, not including the quantum efficiencies of the photodetector. Some crystals have two components of faster (f) and slower (s) decay times.

Crystal	Decay time [ns]	Light yield	Wave length [nm]	Radiation length [cm]	Appropriateness (Bottleneck)
NaI(Tl)	245	100	410	2.59	Poor (D.T.)
BaF ₂	0.9(f)	4.1(f)	220(f)	2.03	Good (W.L.)
	650(s)	36(s)	300(s)		
CsI(Tl)	1220	165	550	1.86	Poor (D.T.)
CsI(pure)	6(f)	1.1(f)	310(f)	1.86	Good
	30(s)	3.6(s)	420(s)		
PbWO ₄	10(f)	0.077(f)	420(f)	0.89	Poor (L.Y.)
	30(s)	0.3(s)	425(s)		
LaBr ₃ (Ce)	20	130	356	1.88	Good (D.T.)

The timing resolution can be roughly estimated as:

$$\sigma_t = T_{DT} / \sqrt{N_{LY} \times e_{q.e.}(w)} \quad (4.1)$$

where T_{DT} is decay time, N_{LY} is the number of photo-electrons per unit deposit energy, and $e_{q.e.}(w)$ is the quantum efficiency of PMT at wavelength w . The calculated σ_t of appropriate materials are 1.4 ns for the fast component of BaF₂, 1.0 ns for the fast component of CsI, and 3.2 ns for LaBr₃(Ce), assuming quantum efficiencies of $e_{q.e.}(220) = 0.1$, $e_{q.e.}(310) = 0.3$, and $e_{q.e.}(356) = 0.3$. The fast component of CsI(pure) around 310 nm wavelength can be selected with a UV bandpass filter. Among the inorganic crystals, CsI(pure) is the best candidate because it has the smallest timing resolution and we had some spare crystals.

The other possibility was sampling detector made of plastic scintillator and metal absorber. The merit of sampling detector is easiness of production compared to crystals. The demerit is that the absorber contained in the detector are dead material. The

thickness of the absorber layer in the Inner Barrel must be equal or smaller than that for the Main Barrel. In the following subsection, we assume that the Inner Barrel has the same layer structure with the Main Barrel, and later, other configurations to obtain better efficiencies are examined. The absorber materials will be also studied in the following section.

4.2.1 CsI

We considered reusing undoped CsI crystals used in the E391a experiment and the FNAL KTeV experiment. With 400 $7 \times 7 \times 30$ cm³ crystals from E391a, we can cover 1.2-meter-long cylindrical region as shown in Fig. 4.1. With 400 remaining KTeV crystals with the dimension of $5 \times 5 \times 50$ cm³, we can cover 1.5-meter-long region.

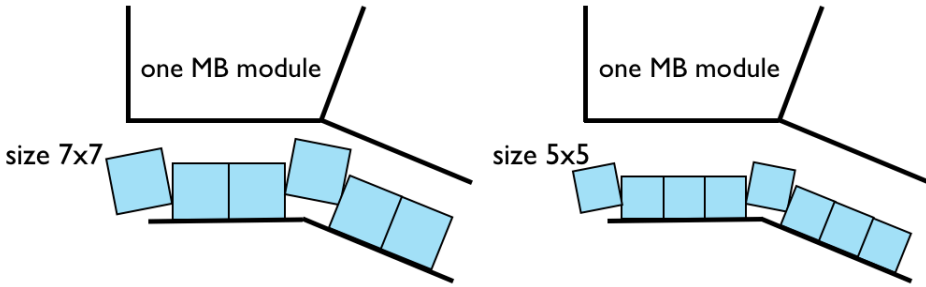


Figure 4.1: Front view of position assignment in case of E391a CsI crystal (left) and KTeV CsI crystal (right).

A 7-cm-thick and 5-cm-thick cylindrical CsI detectors were studied with MC. These thicknesses are equivalent to $3.9 X_0$ and $2.7 X_0$, respectively. Their inefficiencies are shown in Fig. 4.2. The main difference between the 7-cm and 5-cm crystals is apparent

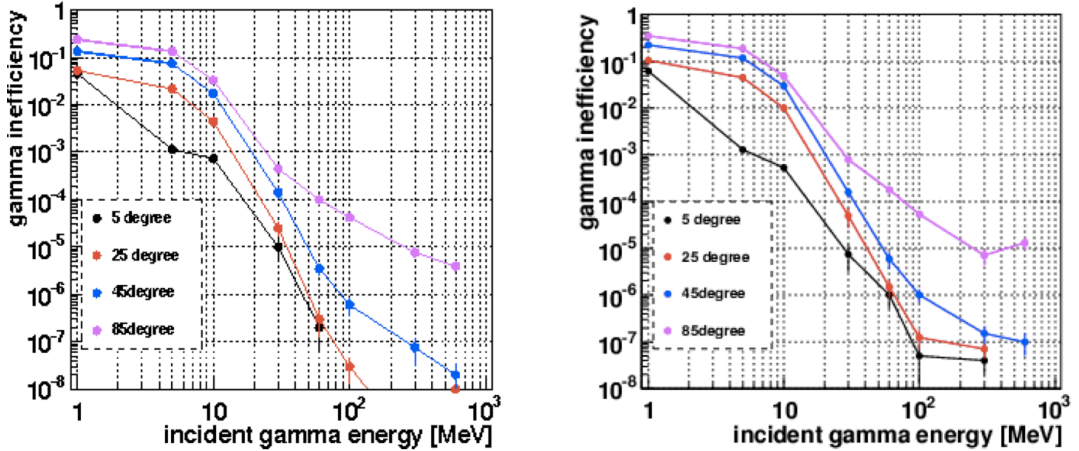


Figure 4.2: Inefficiencies of 7 cm (left) and 5 cm (right) thick CsI detector are shown as a function of incident energy.

in high energy and shallow angle incident gammas. This difference is caused by photo-

nuclear interaction. In contrast, for high energy and close-to-normal incident angle gammas, the inefficiency is dominated by punch throughs.

4.2.2 Sampling detector

As the baseline of a sampling detector, we considered 25 layers of 5-mm-thick scintillator and 1-mm-thick lead. These thickness are the same with those of the Main Barrel Inner Module. Total thickness was $5 X_0$. The inefficiency of a cylindrical detector with this configuration studied with MC is shown in Fig. 4.3.

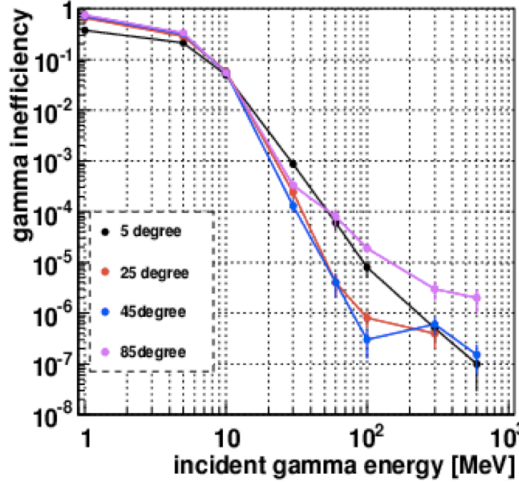


Figure 4.3: Inefficiency of $5 X_0$ -thick sampling detector shown as a function of incident gamma energy.

Sampling detector has larger inefficiencies in the low energy region due to sampling effect. On the other hand, sampling detector has a lower inefficiency in the high energy region near normal incident angle because of its thickness ($5 X_0$ compared to $3.9 X_0$).

4.2.3 Selection of detector type

Inefficiencies of the sampling detector (Fig. 4.3) and the CsI detector (Fig. 4.2) are different in all energy and angle regions. As described in Section 3.2, the main contribution in high energy and shallow angle region was photo-nuclear interaction, and the effect on the inefficiency was complex due to difference of radiation length of the detector and sampling effect of second charged particles. Using the inefficiency curves for these cylindrical CsI and sampling detector models, and by taking into account other detector thicknesses, the numbers of the $\pi^0\pi^0$ background events were calculated and summarized in Fig. 4.4.

The $5 X_0$ -thick sampling detector shows the same level of $\pi^0\pi^0$ background as 7-cm-thick CsI detector. Although the sampling detector has a lower sensitivity toward photo-nuclear interaction than CsI, the same level of background can be achieved with $5 X_0$ thickness.

From the above, we finally decided to build a $5 X_0$ -thick sampling detector.

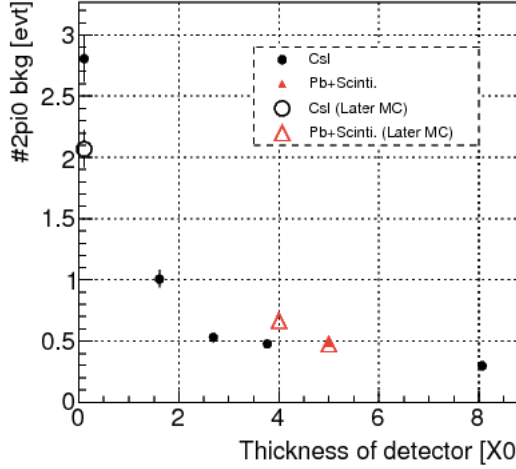


Figure 4.4: The number of $\pi^0\pi^0$ background events, at the sensitivity where 3.5 signal events are expected, are shown for Inner Barrel made of CsI (black circles) and sampling detector (red triangles). Solid circle and solid triangle were estimated with the same MC version. Open circle and open triangle were estimated later with another MC with a more realistic detector setup.

4.3 Layer structure of sampling detector

Performance of a sampling detector depends not only on the active part but also on the absorber part. The secondary charged particles have to go out from the absorber and deposit their energies in active parts to be detected. Here we describe how we decided the absorber material, sampling ratio, and sampling frequency.

4.3.1 Absorber material

The absorber material should have a high ratio of the electromagnetic cross-section σ_{EM} to photo-nuclear cross-section, σ_{EM}/σ_{PN} . This is because photo-nuclear interaction is a dominant source of inefficiency in > 50 MeV energy range.

The cross-section of photo-nuclear interaction is proportional to atomic number Z , because one gamma interact with a small number of nucleons in an atom [34]:

$$\sigma_{PN} \propto Z. \quad (4.2)$$

On the other hand, the cross-section of pair production cross-section [35] is:

$$\sigma_{EM} \propto Z^2. \quad (4.3)$$

The ratio σ_{EM}/σ_{PN} is thus approximately proportional to Z . It thus means that a high- Z material is appropriate for the absorbers.

To confirm the above argument, I ran MC simulations for sampling detectors with iron absorbers and with lead absorbers. The total thickness was made large enough to make the punch-through probability negligible. Figure 4.5 shows the energy deposits in the sampling detectors. The iron-absorber detector creates twice photo-nuclear events

in the initial gamma interaction than lead-absorber detector, and has larger number of events with lower energy deposit.

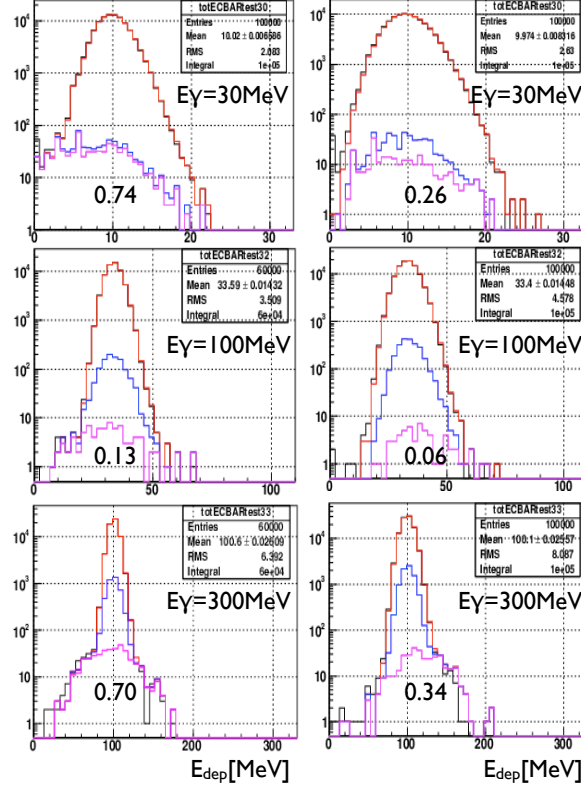


Figure 4.5: The distribution of energy deposit in sampling detectors with iron (left) and lead (right) absorbers. The energy of incident gammas were 30, 100, 300 MeV from the top. The thickness of each absorber plate was 1.5 mm for iron and 1.0 mm for lead. The number of layers were 300 for the detector with iron ($26X_0$) and 200 for the detector with lead ($35X_0$). Black line shows all the events, red line shows events without signal in the BCV, blue line shows events whose secondary particle contain photo-nuclear particles (neutron, proton or heavy ion). Magenta line shows the events in which photo-nuclear particles were created directly from the incident gamma. The numbers shown on the magenta events in the figures are the fractions [%] of these events.

4.3.2 Sampling ratio and frequency

The sampling ratio is defined as the fraction of energy deposited in the active part. Although higher sampling ratio gives a better detection efficiency, we set the ratio of scintillator and lead thickness to 5:1 because of the limitation of total module thickness as described in Section 4.1. With this ratio, the sampling ratio is 0.3, and the thickness of total $5-X_0$ thick detector is 150 mm by lead and scintillator alone.

Varying the thickness of layers while keeping the same sampling ratio shows different detection efficiency for low energy particles. We studied two conditions in addition to the basic condition described in Section 4.2.2 (25 layers of 5-mm-thick scintillator

and 1-mm-thick lead). The two conditions are a) a thinner condition with 42 layers of 3-mm-thick scintillator and 0.6-mm-thick lead, and b) a thicker condition with 13 layers of 10-mm-thick scintillator and 2-mm-thick lead. These conditions have the same 0.3 sampling ratio and the same total radiation length of $5 X_0$. Figure 4.6 shows the detection inefficiencies for these conditions.

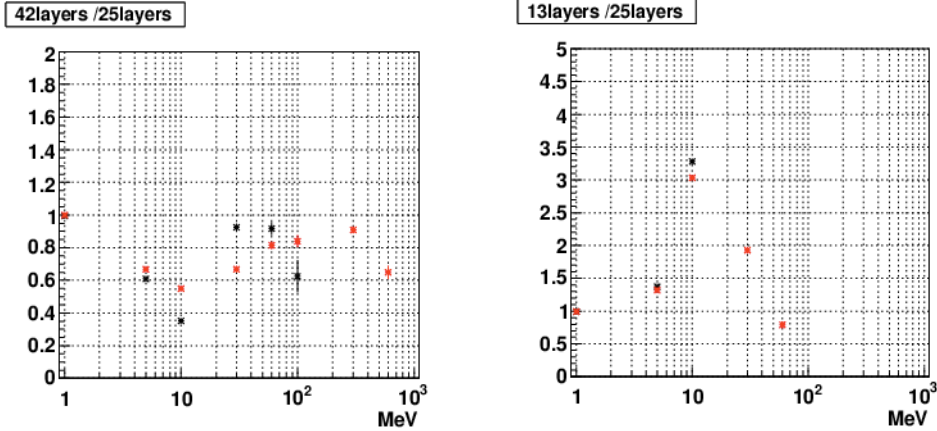


Figure 4.6: Ratios of inefficiencies between detectors with different layer configurations shown as a function of incident energy of gamma. Left figure shows the ratio for the 42 layers of 3-mm-thick scintillator configuration. Right figure shows the ratio for the 13 layers of 0.6-mm-thick lead configuration. Each color of the points shows 45 (black) and 85 degree gamma incident angles.

The main difference between these two sampling frequencies appears around 10 MeV because created e^\pm around 5 MeV can pass only few centimeters. Some e^\pm s with shallow angle become inefficient in thicker lead layers. The number of the $\pi^0\pi^0$ background events with the different layer configurations were also studied and summarized in Table 4.2. The difference of the background events is less than 10 % between the basic condition and the thinner condition. Considering the thickness of fibers and the easiness of handling lead sheets, we decided to select the basic configuration.

Table 4.2: The number of $\pi^0\pi^0$ background events with the Inner Barrel made of different sampling conditions.

Layer thickness [mm]	Number of $\pi^0\pi^0$ background events
Scintillator-3 : Pb-0.6	0.60 ± 0.04
Scintillator-5 : Pb-1	0.64 ± 0.04
Scintillator-10 : Pb-2	0.80 ± 0.04

4.4 Support structure

The shape of the new sampling detector was designed similarly to the Main Barrel. The 32 sectored asymmetric modules were arranged cylindrically. The modules were connected together with a support structure. We define the support structure as all metal material of the Inner Barrel except lead sheets. The main components of the structure are Front Plate and Back Plate at just inside and outside of a module and Ring structures supporting outside all modules. We will describe detail of the structure in Chapter 5. The amount of the structure material could affect the detector sensitivity. In this section, we describe the relation between the amount of material and the number of background events.

4.4.1 Amount of structure material

Most of the support structure was placed outside the Inner Barrel modules. The structure is a dead material for the Main Barrel because it is located inside the Main Barrel. For many types of support structures, we calculated the inefficiencies of the barrel detectors, and estimated the number of the $\pi^0\pi^0$ background events. Figure 4.7 shows the number of the $\pi^0\pi^0$ background events $N(x)$ as a function of the mean areal density (x) of the support structure. The $N(x)$ was approximated as:

$$N(x) = \exp(p_0 + p_1x) + p_2, \quad (4.4)$$

where $p_0 = -3.98 \pm 0.32$, $p_0 = 3.27 \pm 0.26$, and $p_0 = 0.55 \pm 0.03$.

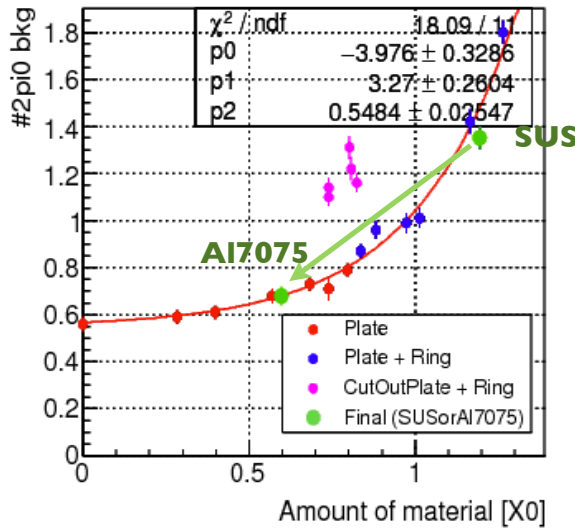


Figure 4.7: The number of the $K_L \rightarrow \pi^0\pi^0$ background events as a function of the areal density of the Inner Barrel support structure. The amount of material is normalized by the area of the Inner Barrel's total outside surface. Cut-out plate is a thicker Back Plate with holes.

The geometry of the structure including “cut-out plate” will be described in Chapter 5. The “cut-out plate” is a thicker Back Plate with holes as shown in Fig. 5.14.

Uneven distribution of support material like cut-off plate showed the larger number of background events. Uniform and low amount of material were thus recommended for the structure.

4.4.2 Gap between modules

A gap between neighboring modules is necessary to allow some tolerances for the construction. The number of the $K_L \rightarrow \pi^0\pi^0$ background events was studied for the gap between 0 and 4 mm as shown in Table 4.3. In this estimation, a realistic amount of support structure was placed behind modules. Difference between gap conditions was estimated within a 4 % statistical error for all the conditions except a 4-mm gap. The number of the $\pi^0\pi^0$ background events in the case of 4-mm gap is 7 % higher than the case without a gap.

If we filled the gap with a material with the radiation length smaller than the absorber, the background was reduced by a few percent. It was because particles passing through the gap interacted and deposited some energies in the active part.

Finally, we decided to make a 3 mm gap between modules without any material filling the gap not to add force on the neighboring modules.

Table 4.3: The number of $\pi^0\pi^0$ background events with $0 \sim 4$ mm gap between modules. The module was sandwiched between an iron Back Plate and Front Plate, and the sides were covered with 0.5-mm-thick iron plates.

Gap width [mm]	Number of $\pi^0\pi^0$ background
0	0.99 ± 0.04
2	0.95 ± 0.04
3	0.99 ± 0.04
4	1.06 ± 0.04

4.5 Energy threshold dependence of sampling detector

For the studies in the previous sections, we fixed the energy threshold at 0.5 MeV. We examined the number of the $\pi^0\pi^0$ background events again as a function of the threshold for a few candidate detectors with different amounts of dead materials. The result is shown in Fig. 4.8. The detector with less dead material for support structure has lower background and smaller energy threshold dependence.

4.6 Criteria for deciding material requirements

As described so far, the number of background events depends on the energy threshold. The threshold is related to the light yield requirement because the number of photoelectrons near the threshold is affected by photon statistics. In addition, the timing resolution is also related to the light yield. In this section, we clarify the assumptions and criteria to decide the requirements on light yield and timing resolution.

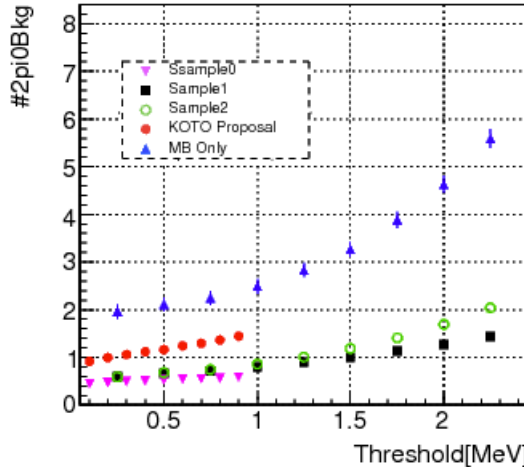


Figure 4.8: The number of the $\pi^0\pi^0$ background events as a function of the energy threshold are shown for sampling detectors with different support structures. Sample0 (magenta reverse triangle) has no support structure, Sample2 (green open circle) is the final design, and Sample1 (black square) has 85 % of the support material of the final design. Design of the KOTO proposal (red circle) and the Main Barrel only (blue triangle) are also shown.

4.6.1 Criteria for studying light yield

To decide the light yield specification, there were three points to be considered.

The first point was comparison with the Main Barrel. Performance of the Inner Barrel should be better than that of the Main Barrel. According to the measurements made just after the Main Barrel construction a decade ago, as shown in Fig. 2.12, light yields were 14.7 p.e./MeV at the center of the Main Barrel, and 11 p.e./MeV at 1.5 m far from the center which was approximatly the edge of the Inner Barrel. Measurements made recently will be described in Chapter 6. With larger light yield than the Main Barrel, we can understand the events with low energy deposit better.

The second point was the timing resolution. The light yield affects the timing resolution. Elements to decide the timing resolution specification will be discussed in the next subsection.

The last point was the main consideration, the effect of light yield on the number of the signal and background events. We evaluated the effect by the signal to background (S/B) ratio. The S/B ratio was closely related to energy threshold and photon statistics at the threshold. The effect of energy threshold and photon statistics are evaluated in Section 4.7.

4.6.2 Criteria for studying timing resolution

Timing resolution is generally approximated as:

$$\sigma_t = \frac{p_0}{E_{vis}} \oplus \frac{p_1}{\sqrt{E_{vis}}} \oplus p_2, \quad (4.5)$$

where E_{vis} is visible energy at the detector, and p_0 , p_1 , and p_2 are constants. The E_{vis} is proportional to the number of photoelectrons. Here, the first term is explained as a noise counting term, such as the effect of a thermo-electron in PMT on a signal. The second term is a photon statistic term, and the last term is affected not only by detector parts but also the readout system such as jitter in electronics.

We compared each term to that for the CsI calorimeter [37] in the same readout system. The first term for the CsI calorimeter was 5 ns for a 1 MeV energy deposit. The first term depends on detector condition and digitizing range in the readout system. Although the detector condition was known only after construction, the digitizing range of energy for the Inner Barrel was considered to be 10^2 times smaller than the CsI calorimeter. The Inner Barrel thus had 10^2 times larger electronic counts per unit energy, and the first term was assumed to be equivalent to that of 10^2 times larger energy in the calorimeter, that was 0.05 ns at 1 MeV energy deposit. As the result, the first term was negligible to be less than 0.1 ns level.

Value p_1 was considered to be the main contribution. Value p_2 was expected to be 0.1 ns level which is the same level as for the calorimeter because this term depends on the readout system and we use the same readout system with the calorimeter. We thus assumed the timing resolution of the Inner Barrel as:

$$\sigma_t = \frac{p_1}{\sqrt{E_{vis}}} \oplus p_2 \quad (4.6)$$

$$\sim \frac{C}{\sqrt{N_{p.e.}}} \oplus 0.1, \quad (4.7)$$

where C is decay time of signal emission in the scintillator and fibers, and $N_{p.e.}$ is the number of detected photo-electrons.

The requirement on the timing resolution was determined based on its effect on the number of signal and background events. The relationship between the timing resolution and these numbers of events will be discussed in Section 4.7.

4.6.3 Calculation for photon statistics

Photon statistics deals with the statistical fluctuation of actual photon output at a defined light yield. The probability of detecting k photo-electrons (p.e.) when x p.e.s are expected, follows Poisson distribution:

$$Poisson(k, x) = \frac{x^k}{k!} e^{-x}. \quad (4.8)$$

The probability that the number of p.e. is below a detection threshold a p.e. is:

$$P(a, x) = \sum_{k=0}^a [Poisson(k, x)]. \quad (4.9)$$

Some calculated samples are shown in Fig. 4.9. The larger expected number of photo-electrons is required to obtain the same detection efficiency with a higher threshold.

On the other hand, signal detection probability depends on the noise level. If we assume that 0 and 1 p.e. are not visible i.e., only single photo-electron can be noise, the inefficiency becomes $P(1, x)$. If we assume that 2 p.e. is also not detected i.e., to be

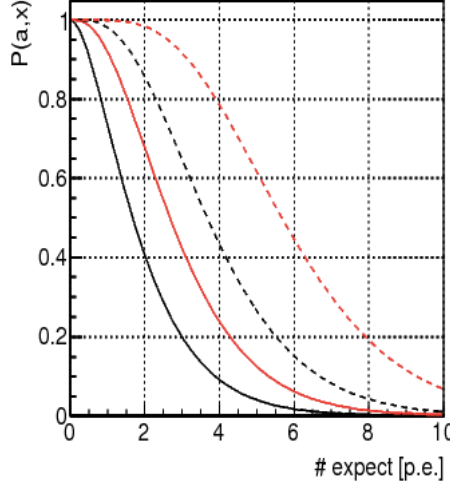


Figure 4.9: The probability $P(a, x)$ that signals are not observed is shown as a function of the expected number of p.e.s. The black solid line shows the probability for the threshold $a = 1$, the red solid line shows that for $a = 2$, the black dashed line shows that for $a = 3$, and red dashed line shows that for $a = 5$.

insensitive to accidental coincidence of single photo-electrons, the inefficiency becomes $P(2, x)$. If we assume 10^6 Hz single photo-electron counting rate and 10 ns timing spread, the accidental coincidence occurs at 1 %. To avoid such accidental coincidence, assuming $P(2, x)$ is safer as the criteria for the light yield.

The number of the invisible events N_{pstat} with photon statistics is calculated as:

$$N_{pstat} = \int_0^{\infty} P(a, bE) N(E) dE, \quad (4.10)$$

where b is the number of p.e. per unit energy deposit, and $N(E)$ is the distribution of energy deposit E used for the analysis. On the other hand, the number of events without considering statistical fluctuation of photo-electrons is:

$$N_0 = \int_0^a N(E) dE. \quad (4.11)$$

Effect of photon statistics will be evaluated with the ratio N_{pstat}/N_0 .

4.7 Relation between background and acceptance recovery

We discuss the number of signal events S and background events B and its ratio S/B in this section to consider requirements on the light yield and timing resolution of the Inner Barrel.

4.7.1 Back splash and $\pi^0\pi^0$ background

We compared the energy threshold dependence on the S/B ratio related to back splash and the $\pi^0\pi^0$ background. In this estimation, we will vary the detection threshold, and the expected light yield per unit energy.

Effect on the S/B by changing these conditions was estimated by a ratio between the original (S_{ori}/B_{ori}) value and the changed (S_{ch}/B_{ch}) value. With the change in the signal acceptance $\alpha = S_{ch}/S_{ori}$ and the change in the number of background events $\beta = B_{ch}/B_{ori}$, the effect of changing conditions is evaluated as $\alpha/\beta = (S_{ch}/N_{ch})/(S_{ori}/N_{ori})$. We could thus discuss the effect on the S/B only with the ratio α and β , without comparing absolute values of S and B .

At first, we compared the energy threshold dependence without light yield assumption. Deposit energy distribution of back splash events in the Inner Barrel is almost the same as that in the Main Barrel shown in Fig. 3.10 because of the same layer structure. We also used the result of the threshold dependence of the number of $\pi^0\pi^0$ background events described in Section 4.5. Energy threshold changes the S/B ratio as listed in Table 4.4.

Table 4.4: Probability of the signal events having back splash hits on the barrel detectors, the number of the $\pi^0\pi^0$ background events in Section 4.5, and the α , β and α/β (change of S , B and S/B) compared with those with a 0.5 MeV threshold.

Threshold [MeV]	Back splash [%]	α	$\# \pi^0\pi^0$	β	α/β
2.0	5.2	1.31	1.02 ± 0.03	1.56 ± 0.03	0.84 ± 0.03
1.0	15.9	1.17	0.72 ± 0.03	1.11 ± 0.04	1.05 ± 0.04
0.5	27.9	1	0.65 ± 0.03	1	1

If we apply only the energy cut without the t-z cut, the S/B ratio is almost the same between 1 MeV threshold and 0.5 MeV threshold. The threshold dependence on the number of background is sensitive to the amount of structural material. If the amount of structural material increases, the S/B ratio at the higher threshold become smaller than that at the lower threshold. We thus set the target threshold at 0.5 MeV.

The effect of photon statistics N_{pstat}/N_0 described in Section 4.6.3 only considered the back splash and the $\pi^0\pi^0$ background. The effect on the number of the $\pi^0\pi^0$ background events is shown in Table 4.5 for thresholds given in terms of the number of photo-electrons (a p.e.), and in terms of energy deposit (e_{th} MeV). The expected light yield is calculated as a/e_{th} [p.e./MeV]. The effect on the number of signal events calculated from the fraction of back-splash is shown in Table 4.6. Compared to the $\pi^0\pi^0$ background, the effect of photon statistics on the back-splash was small. It thus means that the lower energy threshold e_{th} and higher light yield a/e_{th} are desirable to reject larger number of background events.

By multiplying the effect of photon statistics shown in Table 4.5 and Table 4.6 to the number of background and signal events without photon statistics estimation, we could estimate the number of background and signal events with actual light yield easier. At this stage, attenuation of light in fibers is not included. By applying the effect of photon statistics at each light yield to each subdivided detector region, we can also estimate the effect of attenuation. This calculating method was useful for long period of detector material tests and detector construction because the expectation of light yield often changed.

Table 4.5: Ratio of the number of the $\pi^0\pi^0$ background events with to without photon statistics, B_{pstat}/B_0 . Energy distribution of the $\pi^0\pi^0$ events is approximated as a function $N(E_{dep}) = 10^{0.13E_{dep}+0.5}$ for energy E_{dep} [MeV] based on Fig. 3.10 (right).

	Threshold e_{th} [MeV]				
	0.3	0.4	0.5	1	2
Threshold a [p.e.]					
1	2.20	2.28	2.37	2.97	6.27
2	1.57	1.60	1.63	1.79	2.32
3	1.38	1.39	1.41	1.50	1.75
5	1.22	1.23	1.24	1.28	1.40

Table 4.6: Ratio of the number of the accepted signal events with to without photon statistics, $S_{pstat}/S_0 = (S_{tot} - S_{PstatLoss})/(S_{tot} - S_{0Loss})$, where $S_{PstatLoss}$ and S_{0Loss} are the number of back-splash loss events calculated in the same way as N_{pstat} and N_0 in Section 4.6.3, and S_{tot} is the number of signal events detected in the calorimeter. Energy distribution of back-splash is approximated as $S_{loss}(E_{dep})[MeV] = 10^{-0.3E_{dep}+4}$ from Fig. 3.10 (left).

	Threshold e_{th} [MeV]		
	0.5	1	2
Threshold a [p.e.]			
1	1.39	1.10	1.01
2	1.16	1.05	1.01
3	1.11	1.02	1.01
5	1.06	1.01	1.00

4.7.2 Beam accidental activity

We compared the timing resolution dependence on the width of veto timing window for the same S/B ratio as follows.

The beam accidental activity affects signal and background events equally, so that the S/B ratio does not change. However, the larger number of signal events improves the sensitivity of the experiment. By narrowing the veto timing window while keeping the same S/B ratio, the sensitivity becomes better.

To keep the S/B ratio, we assume the width of the timing window as a scale of timing spread of the $\pi^0\pi^0$ background events hitting the barrel detectors. Figure 4.10 shows the timing distribution with timing resolution of the Main Barrel, and a sample detector with a WLS fiber with a 2.7 ns decay time. The parameters relevant to the timing resolutions are listed in Table 4.7. If we use a fiber with a faster 2.7 ns decay time for the Inner Barrel and obtain the same light yield as the Main Barrel, we obtain the $\sigma_T = 0.093$ ns timing resolution and this value is 3 times better than that of the Main Barrel $\sigma_T = 0.304$ ns for gammas with 100 MeV incident energy. Even if we obtain 5 p.e./MeV, the timing resolution $\sigma_T = 0.156$ ns is 2 times better than the Main Barrel.

As shown in Fig. 4.10, the RMS (root mean square) of the timing distribution for these two conditions with 14 p.e./MeV light yield are 0.36 and 0.44 ns, respectively. A sample detector was thus expected to have a 20 % narrower veto width than that of the Main Barrel. This timing distribution is also affected by the timing resolution caused by the CsI calorimeter. Window adjustment with realistic timing resolutions will be discussed in Chapter 8.

Table 4.7: Timing resolution is calculated as a function $\sigma_T = Cb/\sqrt{nE_{in}s}$, where C is the decay time of the light emission in detector material, n is the light yield, b is the factor of the both end readout as $b = 1$ (CsI), $1/\sqrt{2}$ (others), E_{in} is the incident energy, and s is the sampling ratio of the detector as $s = 1$ (CsI), 0.3 (others). Here, the energy E_{in} is set to 100 MeV in this table as the average of incident gamma energy for the $K_L \rightarrow \pi^0\pi^0$ background.

Material	C [ns]	n [p.e./MeV]	σ_T [ns]
CsI	6	12.7	0.17
Y11 fiber (MB)	8.8	14	0.304
		5	0.508
A sample fiber	2.7	14	0.093
		5	0.156

4.8 Decision of detector type and requirements for detector material

We selected the design of the Inner Barrel as 5 X_0 sampling detector placed inside the Main Barrel as described in Section 4.2. It consists of 25 layers of 5-mm-thick plastic scintillator, and 24 layers of 1-mm-thick lead sheets.

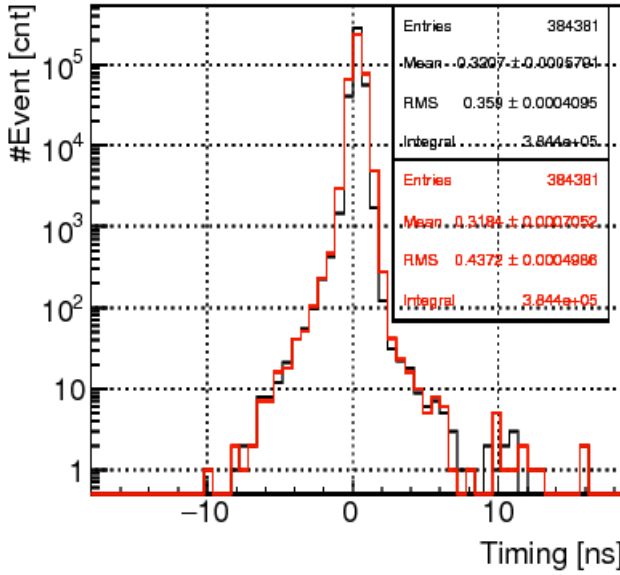


Figure 4.10: Timing distribution hitting the barrel detectors with timing resolution caused by timing response of the Main Barrel (red) and a sample detector (black) listed in Table 4.7.

As discussed in Section 4.4, the detector was also examined from the view point of dead material whether it should be placed inside or not. To be placed inside, support structure should be uniform with $< 0.8X_0$ per unit area.

The total thickness of a module was larger than 150 mm with 5 X_0 detector and support structure. Total length of the detector was about 3 m because of the available space for the detector. Possible space to place the detector was 3 m between just downstream of NCC and just upstream of CV.

From the view point of requirements on detector material, we should prepare the ability to apply a 0.5 MeV threshold based on the back splash related S/B estimation. To be insensitive to photo-electron noise, the threshold should be set to more than 2 p.e. It thus means that the light yield should be larger than 5 p.e./MeV at all positions. The light yield of the Main Barrel was $N_{p.e.} = 14.7$ p.e./MeV at the center and 11 p.e./MeV at 1.5 m far from the center. Although we hoped the same or larger light yield for the Inner Barrel than that obtained for the Main Barrel to understand phenomena close to energy threshold in real environment beyond MC reproduction, it was not necessity as far as data and MC agreed well.

From the view point of timing resolution, a better resolution enables a better back-splash event separation. The lowest requirement was to achieve a timing resolution better than the Main Barrel. Such resolution on the Main Barrel was calculated from Eq. (4.6) as 2.4 ns at the center and 2.7 ns at 1.5 m away from the center for 1MeV energy deposit. If we use a fiber with a decay time faster than 2.7 ns, and obtain the same light yield as the Main Barrel, we can achieve 3 times shorter timing resolution. In that case, we can set a 20 % narrower veto width. Even if we obtain 5 p.e./MeV for the Inner Barrel, we can still achieve a 2 times better timing resolution than the Main Barrel.

Chapter 5

Design for production

In this Chapter, we describe how we chose the material for the Inner Barrel, and how we decided the design for making the actual detector.

5.1 Materials for the active part

The active part of the Inner Barrel consists of scintillator plates, and scintillating light is read out via Wave Length Shifting (WLS) fibers and PMTs. The total light yield is affected by the combination of these three components. The scintillators and WLS fibers have individual absorption and emission light wavelengths. The quantum efficiency of the PMTs has a wavelength dependence. Other elements such as reflector sheets and light guides between fibers and PMTs also affect the light yield.

5.1.1 Candidate materials

We will first list candidate materials that we considered for the active part.

Wave Length Shifting fiber

We examined two candidates for the WLS fibers: Y11 made by Kuraray [28] and BCF-92 made by Saint-Gobain [39]. The Y11 fiber was used for the Main Barrel. The BCF-92 was chosen as a candidate because it has the shortest decay time among available fibers as shown in Fig. 5.1.

Catalog values of both fibers are listed in Table 5.1, and their absorption and emission spectra are shown in Fig. 5.2. We examined single cladding (SC) and multi cladding (MC) BCF-92 fibers and multi cladding Y11 (Y11-M) fiber used for the Main Barrel.

Scintillator

Most scintillators on the market are generally made by casting process. The maximum length of the scintillator made by this process is 1.2 m. On the other hand, the length of the Inner Barrel is 3 m as described in Chapter 4. The total number of scintillator plates required for the Inner Barrel was 800, with the total area of 400 m². To make such large number of long scintillator plates at low cost, we decided to use the extrusion-molding technique, the same technique used for the Main Barrel.

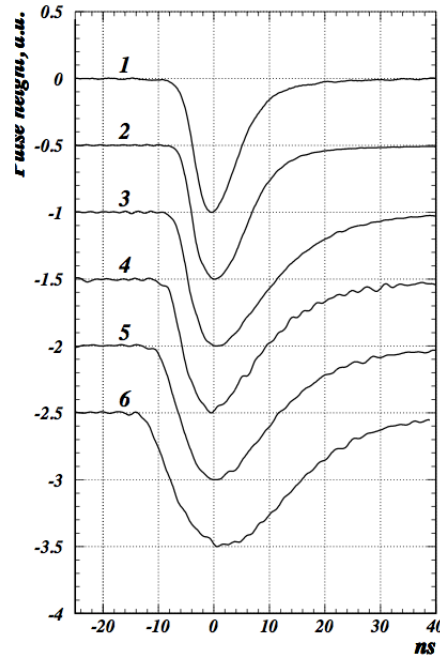


Figure 5.1: The recorded shapes for different WLS fibers: 1 - BCF-92; 2 - BCF-99-29A; 3 - Pol.Hi.Tech.(S250); 4 - Y-11(MS250); 5 - Y-11(M200); 6 - BCF-91A [38].

Table 5.1: Properties of Y11 (M200) fiber [28] and single and multi cladding BCF-92 fibers [39].

	Y11 (M200)	BCF-92 (SC)	BCF-92 (MC)
Decay Time [ns]	8.8	2.7	2.7
Emission Peak [nm]	476	492	492
1/e Length [m]	> 3.5	> 3.5	> 3.5
Core material	Polystyrene	Polystyrene	Polystyrene
Cladding material (inner)	Polymethylmethacrylate	Acrylic	Acrylic
Cladding material (outer)	Fluorinated Polymer	-	Fluor-acrylic

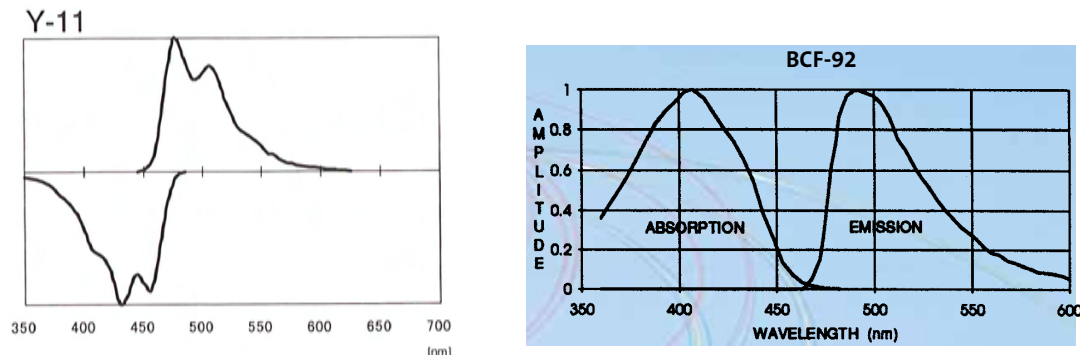


Figure 5.2: Absorption and emission wavelength of Y11-M fiber [28] (left) and BCF-92 fiber [39] (right).

In the extrusion-molding process, melted resin containing fluorescence is extruded from a nozzle and extended. This process requires a certain amount of plastic pellets per one production for stability of extrusion.

In the initial test stage, we studied the compatibility between scintillators and Y11 and BCF-92 fibers. For this test, we used the scintillators made by casting process because this test required only small amount scintillators. Some scintillators containing candidate fluorescences are listed in Table 5.2. The EJ-200 was the scintillator using the same fluorescence with the Main Barrel. The EJ-200 was combined with Y11 fiber to reproduce the performance of the fluorescences and fibers which were used for the Main Barrel. Other scintillators were prepared to be combined with BCF-92 fiber to match its short absorption wavelength.

Table 5.2: Features of tested scintillators [40].

Properties	EJ-200	EJ-204	EJ-230	EJ-232
Scintillation Efficiency (photons/1 MeV e^-)	10,000	10,400	9,700	8,400
Maximum Emission [nm]	425	408	391	370
Pulse Width FWHM [ns]	2.5	2.2	1.2	1.3

PMT

The R329EGP PMT [29] was a highly sensitive PMT developed to readout WLS fibers for the Main Barrel. It has the highest quantum efficiency at 450 nm among 2-inch diameter PMTs.

Combined with Y11 fibers, the number of photoelectrons obtained with R329EGP PMT was 1.8-times higher than the standard type R329 PMT because of the following three modifications. First, well polished electrodes was devised to obtain better light reflection. Second, special material on the photocathode extended the sensitive wavelength to match the emission spectrum of WLS fibers. Third, a prism-shaped photocathode increased the chance of photoelectric emission by increasing the path length of the initial photon in the same photocathode thickness.

Later, we had to adopt R7724 PMTs because R329EGP was not available for all the modules due to difficulty of production of prism-shaped photocathode. The R7724 has super bialkali (SBA) photocathode developed recently. The R7724 was compared with R329EG which was downgraded PMT of R329EGP without prism-shaped photocathode. As shown in Fig. 5.3, R7724 had almost the equal quantum efficiency with R329EG. Total light output calculated for BCF-92 fiber with R7724 was $0 \sim 10\%$ higher than that with R329EG.

Glue

To readout scintillation light with WLS fibers, we made grooves in the scintillator and glued fibers in the grooves. To select glue which offers good light transfer and smooth glueing process, we tested two glues, Saint-gobain BC-600 [39] and NORLAND Optical Adhesive NOA61 [41]. BC-600 is generally used for optical connection of scintillator.

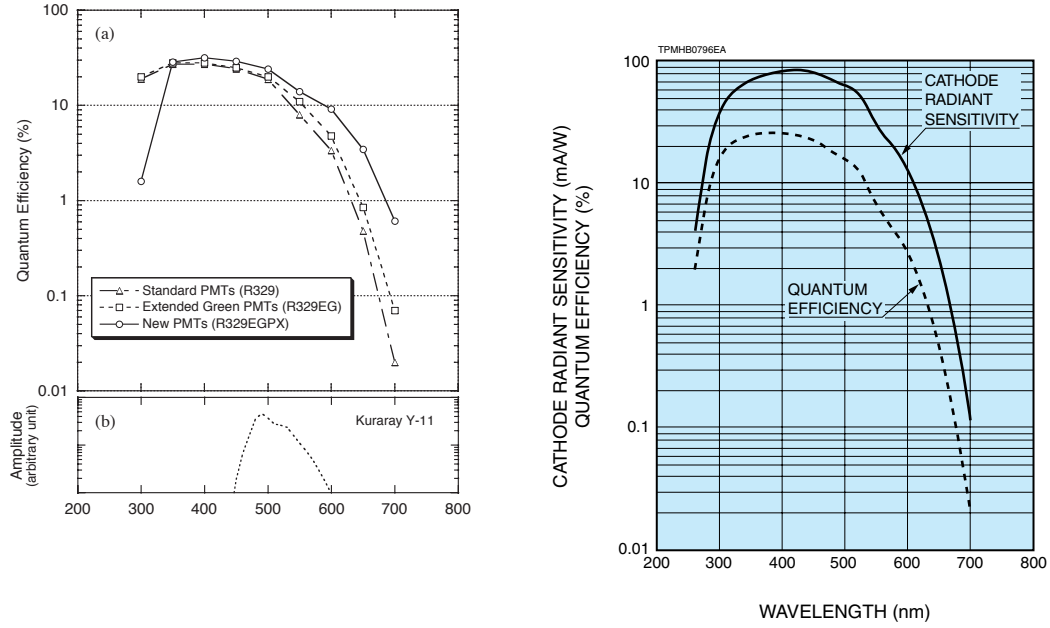


Figure 5.3: The quantum efficiencies of R329, R329EG and R329EGPX PMTs (left) [29] and R7724 PMT (right) [30]. (“P” and “X” in “EGPX” mean “prism-shaped photocathode” and “developing version”, respectively.)

NOA61 was used for the Main Barrel production. The properties of glues are listed in Table 5.3.

Table 5.3: Properties of glues, BC-600 [39] and NOA61 [41], and grease BC-630 [39].

	BC-600	NOA61	BC-630
Refractive Index	1.56	1.56	1.465
Harding Material	Twin pack mixing Epoxy resin	UV light cure Mercapto-ester resin	-
			Silicone

BC-600 takes 24 hours to harden after mixing main solvent and hardener. On the other hand, NOA61 hardens by applying ultra-violet light. NOA61 was easier to use for mass production because it did not harden while placing fibers in the grooves, and dried fast by irradiating ultra-violet light after that.

Absorption wavelength of NOA61 for hardening is within the range of 320-380 nm with the peak at 365 nm. The energy required for full cure is 3 Joules/cm² in this wavelength range. Optimum adhesion will be reached in 1 week. The final form is elastic.

The grease BC-630 [39] by Saint-gobain was also used for the first testing stage to measure the light yield at different distances of fiber readout. Properties of BC-630 are also listed in Table 5.3.

Reflector

We covered the scintillators with reflector sheets to increase the number of readout

photons. We selected TiO_2 PET (Toray RW188 (E60L#188)) which was also used for the Main Barrel. The thickness of the sheet was $188 \mu\text{m}$.

Silicone connector between fiber and PMTs

The bundles of fibers and PMTs were optically connected with so-called silicone cookies. The silicone cookie was transparent, elastic, and removable. By using the cookies, we could attach and remove the PMTs easily as needed during the construction stages.

As for the cookie material, TSE3032 by Momentive Performance Materials with 4 % hardener [42] and KE103 by Shinetsu-kagaku with 2, 3 and 5 % hardener, were tested. Although KE103 with 5 % hardener was used for the Main Barrel, softer cookie was better to make a more reliable optical connection. Hardness of KE103 with 3 % hardener was equal to that of TSE3032 with 4 % hardener. From the view point of the proper optical connection and the production stability, TSE3032 with 4 % hardener, which was used for the CsI calorimeter, was chosen for the Inner Barrel.

Light transmittance of all the tested cookies were $90 \sim 95 \%$ around 400 ns wavelength. The thickness of cookies were adjusted to 5 mm to make optimum optical connection.

5.1.2 Combination of materials

The light yields of the combination of fibers and scintillators were measured. Figure 5.4 shows the light yield measured with a Strontium source. Large fluctuation of measure-

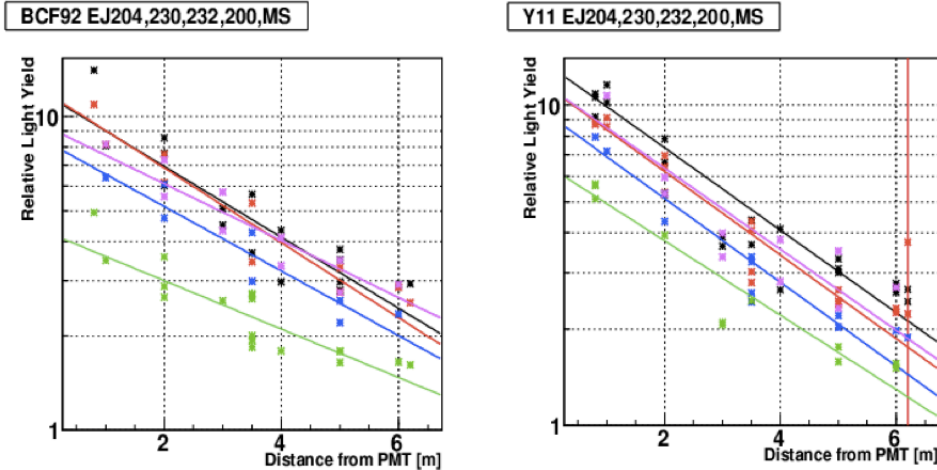


Figure 5.4: Relative light yield v.s. the distance from PMT for various combinations of scintillators and fibers. The EJ-200 (magenta), EJ-204(black), EJ-228(red), EJ-232(blue), and the MS-resin used for the Main Barrel (green) were read out by BCF-92 (left) and Y11 (right) fibers.

ments is due to the reproducibility of optical connection with grease. The light yield fitted at all positions were equivalent between 1.0 mm ϕ BCF-92 and Y11 fibers if they

were combined with EJ-204 scintillator. With BCF-92 fiber, EJ-200 and EJ-204 scintillators showed similar light yield in the regions > 2 m from the PMT.

The timing was also measured with a 50 ps/count resolution TDC. As shown in Fig. 5.5, the timing resolution of BCF-92 was (60 ± 3) % of that of Y11. We thus

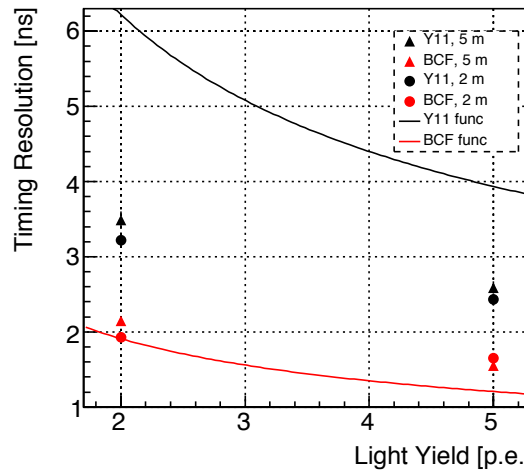


Figure 5.5: Timing resolution measured at 2 and 5 m distance for 2 and 5 photo-electron outputs of Y11 and BCF-92 fibers. The curves are estimated values for Y11 and BCF-92 fibers from Eq. (4.6).

decided to examine BCF-92 fiber further.

To select between EJ-200 and EJ-204 scintillator for BCF-92 fiber, we prepared another setup shown in Fig. 5.6 to reduce systematic ambiguity. The EJ-200 and EJ-204

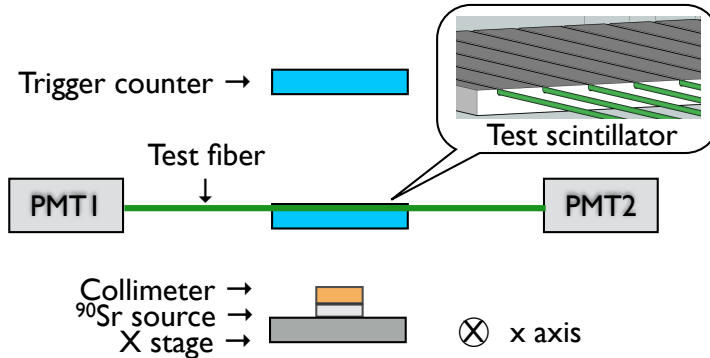


Figure 5.6: Setup to measure light yield in combination of EJ-200 or EJ-204 scintillator and BCF-92 fibers.

scintillators were glued to the center of 2-m-long BCF-92 fibers with adhesive NOA61. The light yield of EJ-200 was 9 ± 1 % higher than EJ-204. Energy distribution and position dependence for direction of width of EJ-200 drawn in units of absolute light yield are shown in Fig. 5.7.

The Table 5.4 shows the relative light yields of other configurations with different

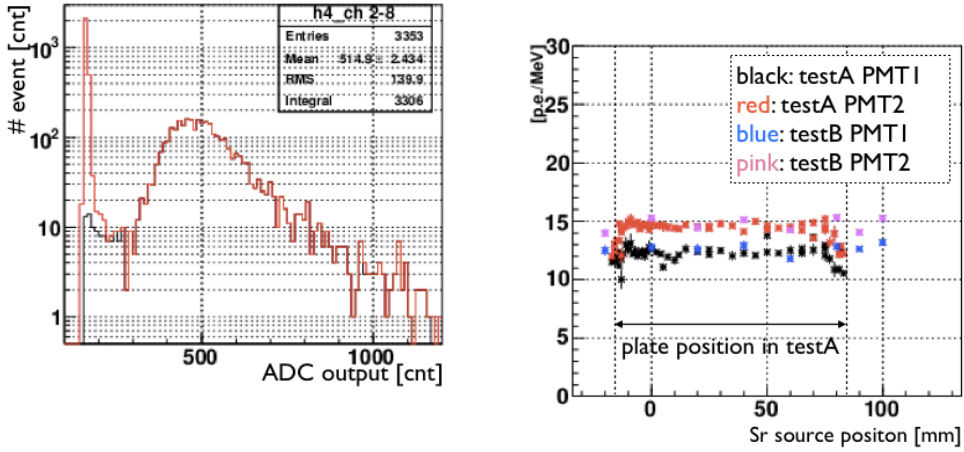


Figure 5.7: Left: The distribution light yield of EJ-200 scintillator and BCF-92 fiber glued with BC600 at 1 m from a PMT. Right: The mean light yield as a function of the position of the ^{90}Sr source on a moving stage. The ADC count is converted to the absolute light yield by one photo-electron count calibrated for PMTs. Combination of EJ-200 scintillator glued with BCF-92 fiber by adhesive BC600 was read out from both ends at 1 m distance. In left plot, the other side PMT signal was required additionally (black line). In right plot, PMT1, 2, means each end readout. Charge of the signal is normalized by that of 1-photoelectron signal measured independently. Difference between PMTs was caused by the difference of PMT quantum efficiency.

fiber pitches and diameters. The basic configuration was EJ-200 scintillator with 10-

Table 5.4: Light yield for different configurations measured by changing only one condition from the basic configuration.

Test ID	Conditions	Relative light yield
1	Basic	1
2	7 mm pitch groove	1.27
3	6 mm pitch groove	1.30
4	1.5 mm ϕ fiber diameter	1.67
5	1.5 mm ϕ fiber diameter, adhesive NOA61	1.50
6	Single clad fiber	0.70
7	U-shaped groove	1.02

mm-pitch grooves in which 1-mm ϕ multi-clad BCF-92 fibers were glued by adhesive BC-600. The grooves had a square cross-section and 0.2 mm larger depth and width than the fiber diameter. Fibers were read out at 1 m from both ends.

The configuration with the 1.5 mm ϕ fiber diameter increased light yield more than the configurations with the 7 mm or 6 mm pitch groove. We thus selected 1.5 mm ϕ fiber as a candidate and decided to examine its properties further.

For the glue, although NOA61 had 10 % lower light yield than BC-600. we adopted NOA61 because it was easier to handle during fabrication.

We selected multi-clad fiber because its light yield was 30 % higher than that of

single-clad fiber. However, we had to purchase single-clad fibers due to a production problem at the manufacture.

We also tried grooves with a U-shape cross-section whose diameter was 0.2 mm larger than fiber diameter. The groove cross-section can be changed by changing the shape of blade for the lathe. The light yield was the same as that of the basic configuration. We selected the U-shape groove because bubbles did not remain at the groove edge.

5.1.3 Examination of larger-diameter fiber

We examined larger BCF-92 fiber when we changed fiber diameter from 1.0 mm ϕ to 1.5 mm ϕ . We studied position dependence of light yield compared with 1.0 mm ϕ fiber, and the relation between light yield and fiber bending radius for bundling.

Figure 5.8 shows the light yield of 1.0 mm ϕ and 1.5 mm ϕ fibers measured as a function of distance from the PMT with 405nm LED. Both fibers had similar attenuation

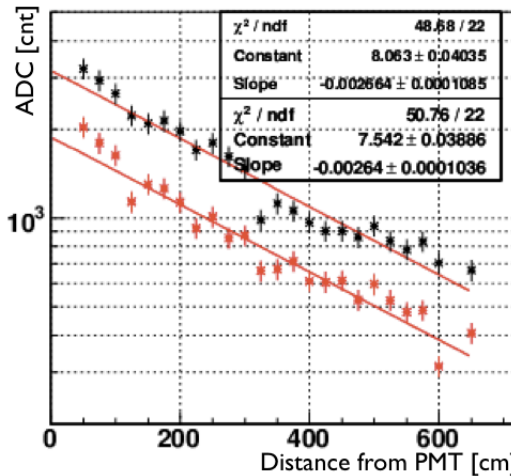


Figure 5.8: Fiber attenuation length about 1.5 mm ϕ (black) and 1.0 mm ϕ (red) BCF-92 fiber irradiated by 405 nm wavelength LED.

lengths.

Before large purchase, we developed a relative light yield measuring system with 405 nm wavelength LED for accurate and speedy measurement. We parametrized relative light yield with two exponential attenuation length as:

$$f(d) = A_1 \exp\left(\frac{-d}{L_1}\right) + A_2 \exp\left(\frac{-d}{L_2}\right), \quad (5.1)$$

where A_1 and A_2 are normalization factors and L_1 and L_2 are attenuation lengths in units of cm. Typical fiber attenuation length for the delivered 1.5 mm ϕ single clad fiber was $A_1 = 4.254 \pm 0.2042$, $A_2 = 3.544 \pm 0.1358$, $L_1 = 66.99 \pm 5.412$ and $L_2 = 418.6 \pm 12.99$ [43].

Relation between light yield and bending radius for both multi-clad and single-clad fibers was tested. The light yield decreased by $\sim 10\%$ if the fiber was bent with a 7 cm diameter.

5.1.4 Selection of extrusion-molding scintillator

We selected the same fluorescence with EJ-200 scintillator for extrusion-molding scintillator. The scintillator was made of MS-resin (80 % polystyrene and 20 % meta-acrylate) mixed with 1.2 % p-terphenyl and 0.045 % POPOP. We also tried 1.45 % p-terphenyl and 0.045 % POPOP sample.

The light yield of new extrusion-molding scintillator fluctuated between productions. The light yield of the scintillator was $60 \sim 70$ % of that of EJ-200. Difference of light yield between the samples with 1.2 % and 1.45 % p-terphenyl was negligible compared to the production fluctuation.

The scintillator extrusion methods were different between the way for the Inner Barrel and the Main Barrel. The extrusion for the Main Barrel was done by rolling out, whereas melted scintillator was pushed through a square frame for the Inner Barrel. In these extrusion-molding process, evaporation and coagulation of fluorescence occurred, and grains of the fluorescence stuck on the roll or the frame. The grains on the frame could not be wiped away, and made stripes on the scintillator surface.

We examined the effect of stripes with test scintillators with and without grinding. The grinding increased the light yield only by (3 ± 1) %. The gain in the light yield was small, considering the cost of grinding.

Finally we selected MS-resin mixed with 1.2 % p-terphenyl and 0.045 % POPOP without grinding surface.

5.1.5 Light yield of module

As active part of the Inner Barrel, we selected 1.5 mm ϕ BCF-92 fiber and MS-resin based scintillator mixed with 1.2 % p-terphenyl and 0.045 % POPOP. Fibers were glued with scintillator by adhesive NOA61 in 10 mm pitch U-shaped grooves.

We made a 1/10-length prototype module with the selected materials, but with two differences: we used EJ-200 scintillator instead of MS-resin scintillator, and multi-clad fibers instead of single-clad fibers. The production process was also tested by making the prototype.

The light yield of this prototype was (11.0 ± 0.1) p.e./MeV at 4.8 m away from a R329EGP PMT. The expected light yield with the final materials was 5.0 p.e./MeV at 4.8 m distance considering the light yield ratio between MS-resin and EJ-200 ($\times 0.65$) and the ratio between single-clad and multi-clad fibers ($\times 0.70$).

5.2 Mass production process of active part

This section describes the process to produce one layer of scintillator connected with fibers.

Scintillator preparation

The scintillator was produced and processed by a manufacture.

The 400-mm-wide scintillator was extruded. The thickness varied across the width; the side was (5.14 ± 0.05) mm thick and the center was (4.97 ± 0.02) mm thick for a few measured sample plates. The difference in thickness was caused by the difference in the pressure during extruding from the frame. After an extrusion-molding process,

the scintillator plate was cut into half width along the long direction by grinding. We alternately assigned the edge that was at the center of original scintillator to left and right of the module to make the module thickness uniform.

The scintillators were cut twice to release internal stress and to make the edges straight. After releasing the stress by the first cut, the second cut ensured the straightness of the plate within 0.5 mm. All the grooves on the scintillator plate were made by one pass of multi-blade saws. The straightness of the grooves was kept with the same precision with the plate straightness. This tolerance satisfied the requirement for constructing a cylindrical detector, and for making the glueing process smooth. After the grooved scintillators were delivered, we had to remove shavings remaining in the grooves by ourselves.

Fiber preparation

We cut fibers from a reel to 4.5 m. (Actually, 4.2 m was long enough.) and checked that each fiber has uniform diameter and no damage. The light yield of the fibers varied between reels by $\pm 20\%$ [43]. The fibers with high and low light yields were assigned to the grooves alternately to make the light yield of modules even [43]. We protected the fibers near the scintillator edge with 2-cm-long thin tubes made of PEEK resin. The ends of fibers were fixed temporary on a table for curing called exposure table so that the fibers would not move while curing glue.

Glue applying

We applied glue in the grooves in a scintillator by a dispenser system attached to an automatic positioning stage. All three dimensions were controlled by the stage fixed on a special table made for applying glue. We fixed the scintillator on the table with bolts and supporters, and adjusted the position of the needle of the dispenser system before start applying glue. We applied 1.4 cc/m glue at speed 30 cm/sec.

Cureing

The scintillator plate was moved from the table for glueing to the exposure table after applying glue. We lowered the fibers into the grooves, and added tension to fibers to soak them in glue. We exposed glue to UV light for an hour. The exposure time was decided based on the production test.

5.3 Concept for assembling modules

Missions for assembling module were to make rigid module shape and to decide module length to readout from narrow space between detectors.

5.3.1 Rigid module

The modules have to keep their shapes even when they are rotated along the beam axis.

To keep the detection inefficiency low, the module shape should be kept with small amount of dead material. We considered the three methods shown in Fig. 5.9 to keep the module shape.

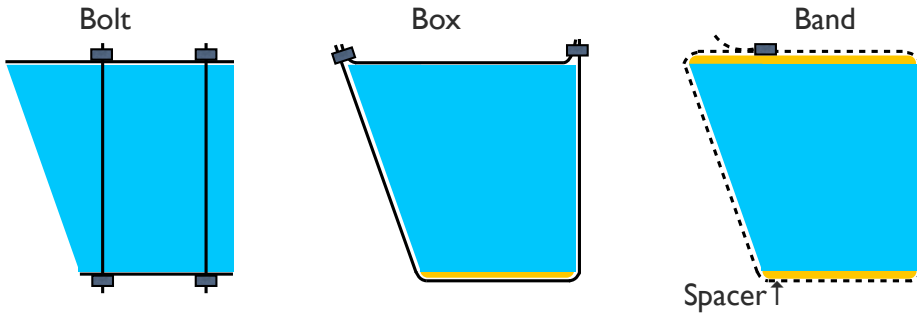


Figure 5.9: Three methods to make rigid module.

The first method was the same as the method used for the Main Barrel. The scintillator and lead plates are pushed together with bolts penetrating through the module. Although this method was successful, it was expensive; a total of 50 holes had to be drilled on every scintillator and lead plate.

The second method packs the scintillator and lead plates inside a rigid box. The box should not deform along its 3 meter length. Although the box is made by bending a thick plate to U-shape, the curvature of its corner had to be large to keep its strength. To reduce the requirement on the box strength, we considered applying a pressure on the scintillator and lead plates and use the friction between layers to keep the module shape. This idea lead to the third method.

The third method presses the layers just as the first method, but with bands around the module to apply pressure. To prevent the layers from slipping, the compressing force

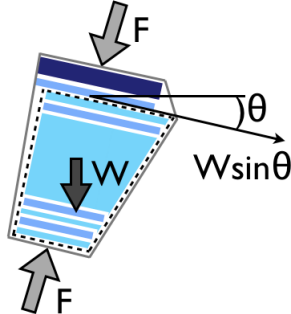


Figure 5.10: Module deformation and compressing force.

F should satisfy:

$$\mu(F - W \cos \theta) > W \sin \theta, \quad (5.2)$$

where μ is the coefficient of friction, W is module weight, and θ is tilt angle as shown in Fig. 5.10.

If we use n bands, the tension on each band is:

$$f = F/2n. \quad (5.3)$$

The measured friction coefficient μ was 0.24 between the reflector and lead, 0.55 between the reflector and test acrylic plate. The required force at each band was thus $f=59$ kgf for $W=250$ kg and $n = 9$.

Several types of tapes and steel bands were tested. Although glass-cross tapes were strong enough, its aging effect was the largest concern. A concern about steel band was that once the steel is belt bent at a module corner, it could not be tightened any more. This problem was solved by attaching a plastic guide with a large curvature at the module edge.

Another concern was about the amount of dead material for the strong plates to keep the lead and scintillator layers flat. This concern was solved by using stronger plates outside the module to prevent the deformation of total module. We named the plate covering the inside surface of the module as Front Plate, and the plate covering the outside of the module as Back Plate. The Front Plate also served as the first absorber layer in total barrel detectors. Its radiation length had to be equal or less than an absorber layer of the Inner Barrel. Inside the Front Plate, new Barrel Charged Veto was placed.

From the above, we selected the method using the steel bands to apply pressure around the module sandwiched between Front Plate and Back Plate. These structural components are described in next section.

5.3.2 Module length and readout

Figure 5.16 shows the side view of the final design of the Inner Barrel. The length of

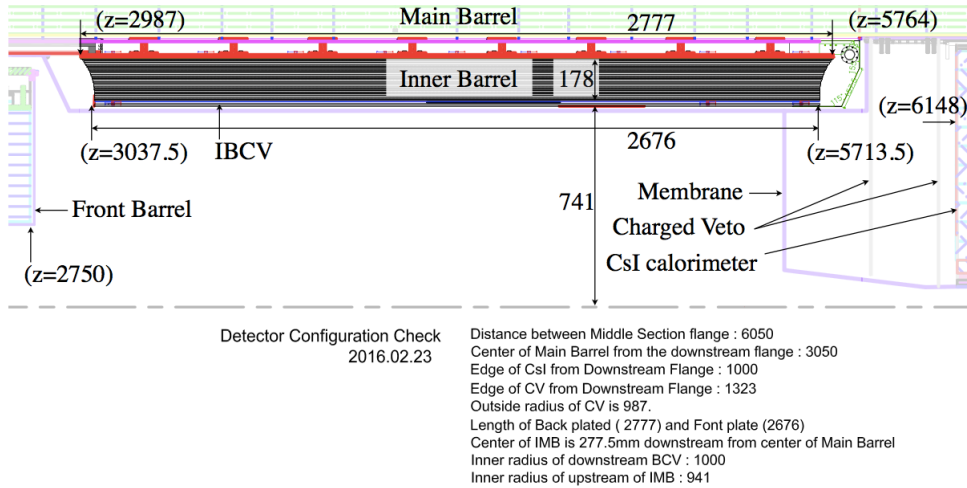


Figure 5.11: Side view of the Inner Barrel. Each size and position was measured value except the calculated position from the upstream edge of the Front Barrel written in parenthesis.

the Inner Barrel was decided based on the space available inside the detector system, the allowed fiber curvature, and required air flow for evacuation.

The fibers were bundled just outside the scintillator and connected to a 2-inch PMT. The diameter of the bundle of 400 fibers from a module was ~ 40 mm. The relation

between a fiber curvature and the distance between the scintillator edge and the PMT is shown in Fig. 5.12. The distances are:

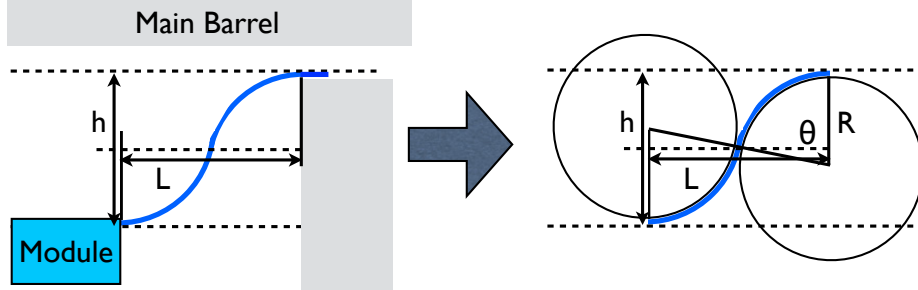


Figure 5.12: Fiber curvature.

$$h = 2R(1 - \cos\theta), \quad (5.4)$$

$$L = 2R\sin\theta, \quad (5.5)$$

where R is the fiber curvature radius, and θ is angle keeping the curvature. By removing θ from the equations, we get:

$$L^2 = 4Rh - h^2. \quad (5.6)$$

The curvature of fibers outside the scintillators was kept larger than 100 mm in radius. The limitation of radial distance h is required for fibers to be able to pass through the the gap between the Main Barrel and other detectors. The required h is 67 mm for the outermost layer, and 220 mm for the innermost layer. In addition, a 16-mm margin for L between the edges of the Front Barrel and the Inner Barrel was added to allow air flow during evacuation. The distance between the edge of the Front Barrel and the surface of the Charged Veto was 3092 mm.

Based on these boundary conditions, the length of the Inner Barrel was decided to be 2777 mm for the outermost layer, and 2676 mm for the innermost layer.

5.4 Material of non-active part in module

Properties of absorber and tools for forming modules are described.

Lead sheet

Lead sheets were produced according to the Japanese Industrial Standards (JIS). The purity was 99.99 % and the tolerance of thickness was less than ± 0.1 mm for 1.0 mm thick plate including safety factor provided by the manufacturer. The radiation length of a layer is $0.18 X_0$. The lead sheets were degreased to prevent out-gassing in vacuum.

Stiffer lead sheets containing 4 % antimony (Sb) was considered for the easiness of construction, but they were not available for a thickness < 3 mm.

Steel bands

To tighten the lead and scintillator plates together, 3/4-inch-wide and 0.76-mm-thick stainless steel (SUS201) band made by Bandit was chosen. The band can support maximum of 1020 kgf tensile strength.

Band guide

A plastic pieces shown in Fig. 5.13 were placed on the Front Plates and Back Plates to guide the steel band with a 12 mm curvature.

The band guide is made of polyethylene. The material was chosen because of its low mass, low out-gassing, high yield strength, and a low friction coefficient between it and steel band. To prevent the steel band from slipping, it has 1-mm-high side walls.

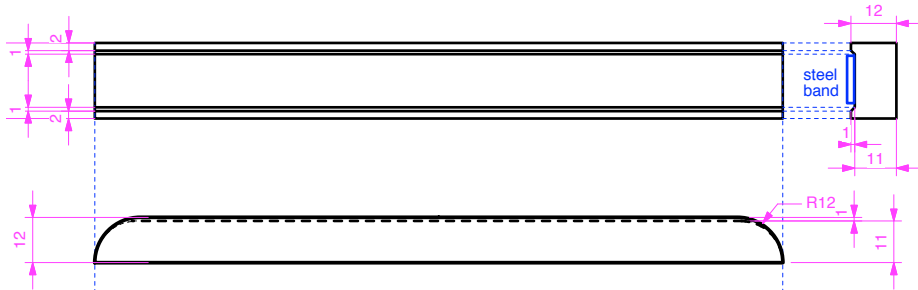


Figure 5.13: Band guide plastic.

Front Plate

The Front Plate is a 3-mm-thick ($0.17 X_0$) SUS plate. The Front Plate serves as a strong structure to keep the lead and scintillator layers flat, and also as the first absorber of the module.

Back Plate

The Back Plate has two roles.

The first role is to prevent the module from deformation. Two shapes were considered. One was just a thin flat plate, and the other was a thicker plate with holes between the path for stainless steel bands as shown in Fig. 5.14. As described in Chapter 4, the flat

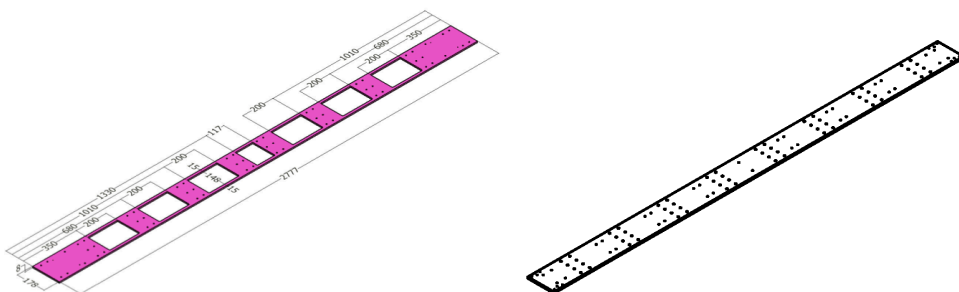


Figure 5.14: A sample of Cut-out back plate (left) and flat Back Plate at final design (right).

structure (uniform thickness) had a benefit to lower the number of background events.

The second role is to connect the module to supporting rings on the outside. The thickness of the Back Plate had to be larger than 10 mm to use M8 bolts. We decided to make the Back Plate with a 10-mm-thick A6061-T651 aluminum alloy plate.

5.5 Production process of assembling modules

To construct a module, we used an inclined table used to make the Main Barrel modules for E391a. We stacked scintillators, lead sheets, and reflector sheets between them, on the table. The length of lead was about half of total module length for the easiness of handling. We used two lead sheets per one layer and the positions of boundaries were switched between layers.

The Front Plate and Back Plate on which band guides were connected were placed at first and end of piling up. After all the layers were stacked, the Back Plate was placed on top, and the layers were pressed with 4.5 tons of force uniformly for 12 hours by oil press system to flatten the lead sheets.

The total module thickness depended on the thickness of scintillator because the tolerance of lead was smaller than that of scintillator. Extrusion-molding scintillator could keep uniform thickness for long direction and the thickness was (5.06 ± 0.02) mm for a few measured sample plates. With assignment of thicker and thinner side alternately, the tolerance of total module thickness was less than 1 mm. We bound the module at 9 positions with the steel bands. The binding force was checked based on the thickness of the module to be the same as that under pressure.

A bundle of fibers were hardened inside an acrylic pipe with epoxy-base adhesive. After 24 hours for hardening, the bundle and the acrylic pipe were cut together, and polished to have a good optical connection with a silicone cookie.

5.6 Design of cylindrical structure

The Inner Barrel was designed to be a self-supportive detector because it cannot be connected to the Main Barrel.

Initially, we considered a Roman arch structure in which modules are pushed inward to form a cylindrical detector shape. However, there were two difficulties due to non-rigid body of the module.

First, the force between modules may be concentrated on small areas where the modules touch each other. In that case, scintillator could brake. Second, even if we could assemble all the modules cylindrically, a sheer stress deforms the module. The sheer stress is caused by torque from fulcrum of the next module. Although we also considered to connect modules at the Back Plate, the structure satisfying the strength against the sheer stress was too massive to be installed inside the Main Barrel. Finally the modules were decided to be supported by 8 rings on the outside as shown in Fig. 5.15. The support ring was made of AL-7075-T7352 aluminum alloy.

Each module is supported individually from outside. A gap between neighboring modules was needed so that the modules would not apply forces each other. The size of gap was decided to be 3 mm based on the background estimation described in Chapter 4.

Figure 5.16 shows the front view of the Inner Barrel in the final design. To insert the

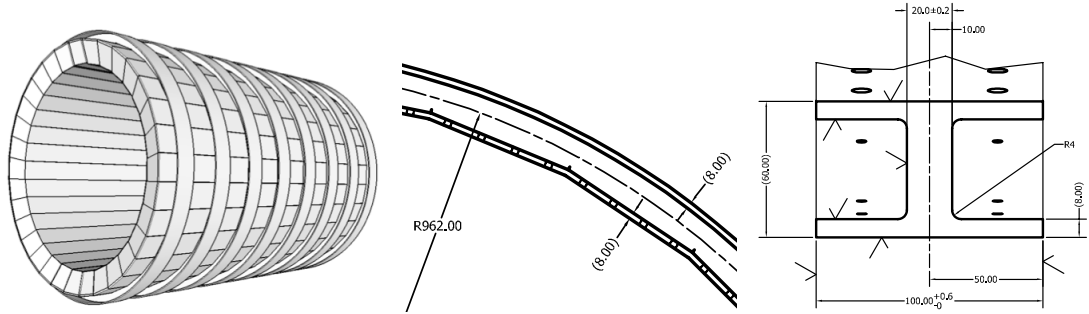


Figure 5.15: Inner Barrel supported by 8 rings (left figure) and design of ring (right two drawings).

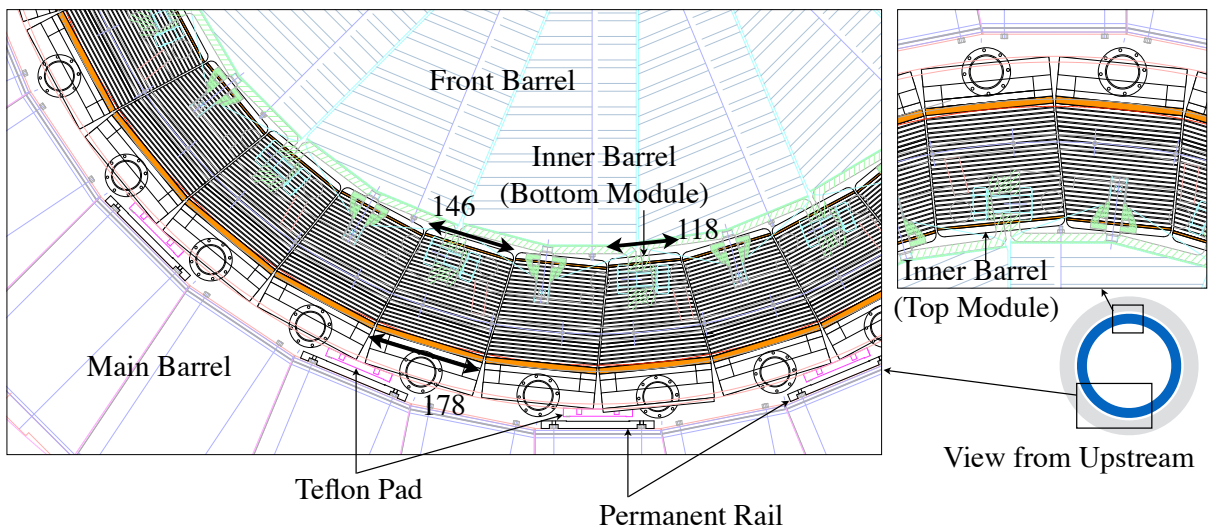


Figure 5.16: Front view of the Inner Barrel.

final module into the ring, the top module had a rectangular cross-section.

To insert the Inner Barrel into the Main Barrel, 5 sets of aluminum rails and pads were aligned. To reduce friction between rails and pads, 1-mm-thick teflon sheets were glued on the rails and pads. The size of the rails remaining after the installation on the Main Barrel were $180 \times 4250 \times 12t$. The size of the pads on the 8 rings were $110 \times 120 \times 17t$ ($16.5t$) (with a curved inner surface to match ring).

Chapter 6

Light yield and timing resolution obtained by the Inner Barrel and the Main Barrel

After we constructed the first Inner Barrel module, we studied its performance.

We also investigated the Main Barrel, because we had not understood its performance related to the waveform readout, and we had to finally evaluate the combined performance of the Inner Barrel and the Main Barrel.

In Section 6.1, we introduce the relation between several parameters and the performance. In Section 6.2 and Section 6.3, we report measurements of parameters for the Inner Barrel and the Main Barrel, respectively. In Section 6.4, we describe the timing resolution estimated based on the measured parameters.

6.1 Relation between detector response and resolution

As described in Chapter 4, requirements on the performance of the Main Barrel and the Inner Barrel were decided based on light yield and timing resolution. As expressed in Eq. (4.5), timing resolution depends on the light yield and noise level. Noise and the different number of photoelectrons change the shape of waveforms, and the fluctuation of shapes and the timing defining method of waveform affect the timing resolution. Therefore, we reproduced waveforms to understand the timing resolution.

Waveforms are affected not only by light yield and noise level but also by the timing spread of photoelectrons and sampling frequency of the readout system. Light yield and the noise level were measured and described in the following sections. As for the sampling frequency of the readout system, we studied 125 MHz and 500 MHz. The timing spread of photoelectrons was defined and measured as follows.

The timing spread of photoelectrons depends on the material and the structure of a detector. Detector components that determine the waveform in the Main Barrel and the Inner Barrel are classified into scintillator, wavelength shifting fiber, PMT, and FADC. In scintillator, a fluorescent signal has a timing spread according to the path of the incident particle and emission decay time of the scintillator. Wavelength shifting fiber absorbs the light from the scintillator, and re-emit scintillation light with a different wavelength according to its emission decay time. The signal in fibers also spread by different paths

of photons in the fibers. Although Monte Carlo for KOTO already contained the effect of the paths of incident particles, it did not include other processes. In particular, the fiber emission decay time dominated the total timing spread. We included the effect of these timing spreads in scintillator and fibers in Monte Carlo as timing probability density function (timing PDF) of photoelectrons.

The timing PDF was extracted as shown in Fig. 6.1. To extract a timing PDF, we

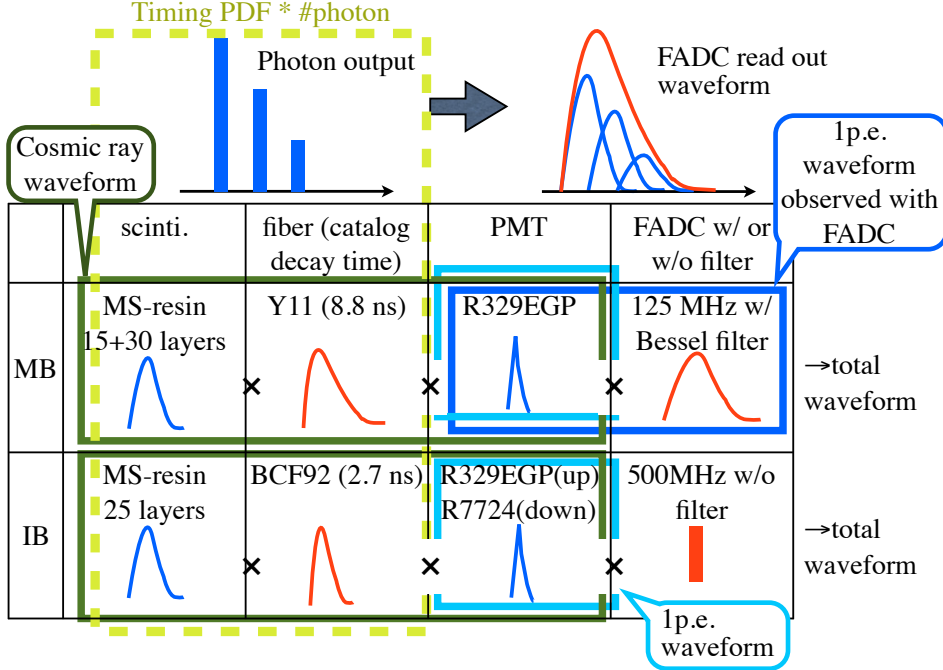


Figure 6.1: Method of timing PDF extraction and combining to realistic waveform.

used a scope to see the PMT signal for two types of data: the waveforms of cosmic ray signals, and the waveforms of 1-photoelectron signals. Additionally, to convolute the pulse shaping effect of the Bessel filter, we also measured 1-photoelectron signals with a 125 MHz FADC.

The waveform of cosmic ray signal is made of 1-photoelectron signal pulses distributing according to the timing PDF. We thus convoluted the timing PDF and the pulse shape of 1-photoelectron signal. We fitted the observed waveform with the reconstructed waveform by varying the parameters for the timing PDF and searched for the waveform at the minimum χ^2 . Details will be described in Section 6.4.

To create an observable waveform, we convoluted a pulse caused by detector components based on timing PDF, light yield, and a pulse caused by PMT and FADC.

6.2 Parameters of the Inner Barrel

We collected waveforms of cosmic ray signals observed in a module and 1-photoelectron signals with a 500-MHz-sampling FADC, and a 5 GS/s sampling rate 500-MHz-bandwidth scope. With the FADC, we obtained light yield and timing resolution for minimum-

ionizing particles (MIP). With the scope, we obtained the waveforms of cosmic rays and 1-photoelectron signals. The measured timing resolution by the FADC is compared with the resolution estimated in Section 6.4.

6.2.1 Parameters measured with 500 MHz FADC

Figure 6.2 (left) shows the measured light yields as a function of the distance from a PMT [43].

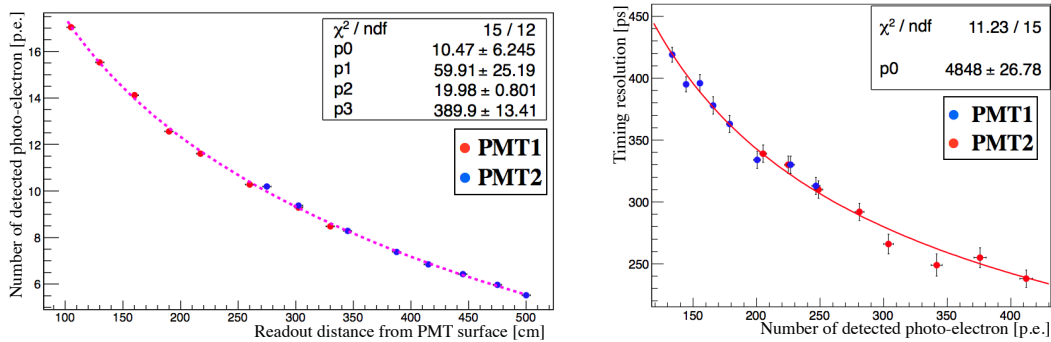


Figure 6.2: Light yield (left) and timing resolution (right) for the Inner Barrel obtained from cosmic ray data taken with 500 MHz FADC [43].

The light yield at 5 m from a PMT was (5.6 ± 0.2) p.e./MeV. The attenuation lengths fitted with Eq. (5.1) were (59.91 ± 25.19) cm for a short component and (389.9 ± 13.4) cm for long component.

Figure 6.2 (right) shows the timing resolution obtained with cosmic ray MIPs. The resolution was $(4850 \pm 30)/\sqrt{N}$ [ps/(p.e.) $^{1/2}$] for $N = 100 \sim 500$ and the corresponding z-position, where N is the number of photoelectrons deduced from the light yield at each cosmic ray position.

6.2.2 Waveform of cosmic ray signal

The waveforms of cosmic ray signals were measured with a scope to obtain data relevant for the timing PDF. The waveforms were measured at 4 z-positions in a module. The setup is shown in Fig. 6.3.

The typical waveform was obtained by taking the average of waveforms after normalizing the peak heights, and shifting the waveforms in time to match the peak timing. The peak position was defined by fitting the waveform with landau function. The typical waveform will be used to extract timing PDF in Section 6.4.

6.2.3 Waveform of single photon signal

Waveforms of 1-photoelectron signal were measured with a scope. Typical 1-photoelectron waveforms of R329EGP PMT and R7724 PMT are shown in Fig. 6.5. The typical waveform of 1-photoelectron will be used in Section 6.4.

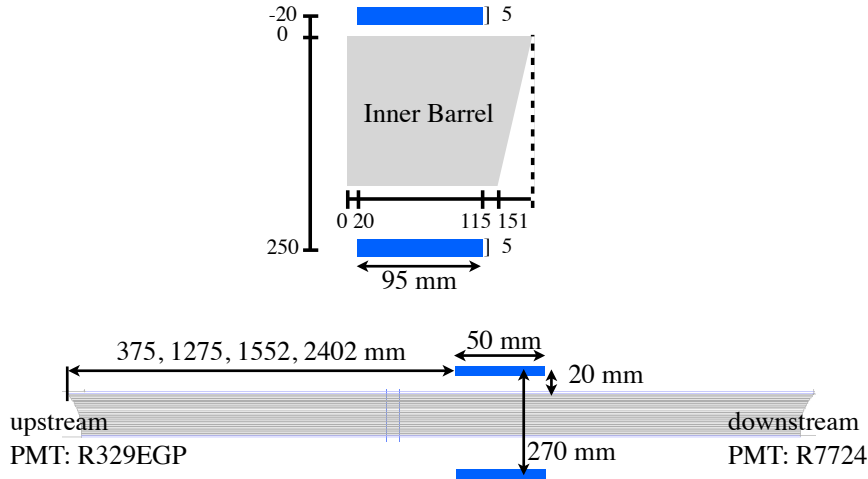


Figure 6.3: Setup of waveform measurement for cosmic ray data. Top figure shows the front view and bottom figure shows the side view. Trigger counters were placed above and below the Inner Barrel.

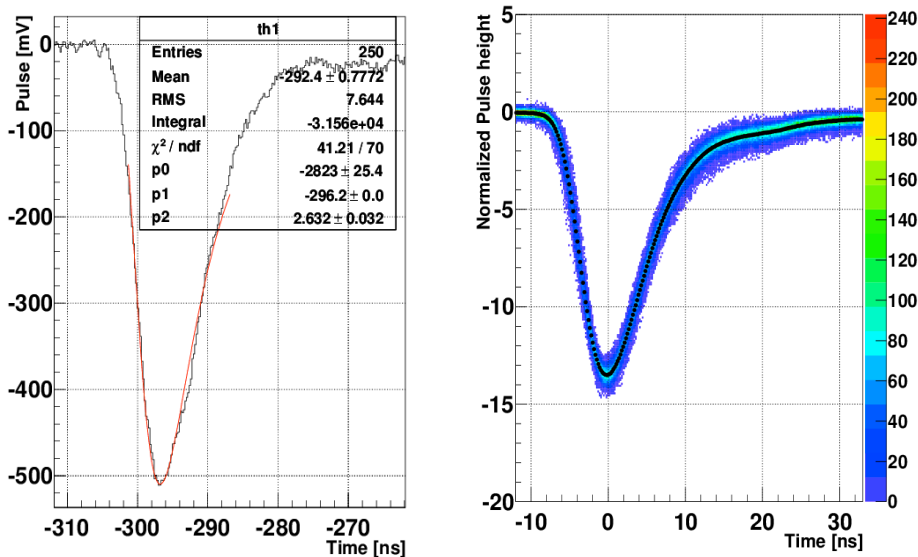


Figure 6.4: Left: Waveform of a cosmic ray event fitted. Right: Overlaid waveforms after matching the fitted peak timing and fitted peak heights. Black points in the right figure show the averaged typical waveform.

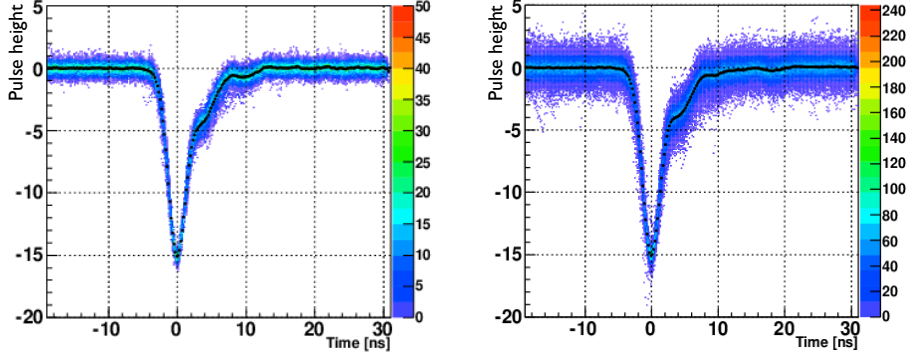


Figure 6.5: Waveform of 1-photoelectron signal measured with R329EGP PMT (left) and R7724 PMT (right). Waveforms were shifted in time to match the fitted peak timing and normalized by the fitted peak height with a gaussian function. Black points show the obtained typical waveform.

6.3 Parameters of the Main Barrel

Some parameters for the Main Barrel were measured differently from the Inner Barrel because they had to be measured after the Main Barrel was assembled. We measured light yield, waveform and noise level to obtain timing resolution.

6.3.1 Light yield

We measured the light yields of 4 Main Barrel modules during detector reconstruction in 2012, and all of the modules in 2015 after assembling. The light yields measured in 2012 were consistent with the light yields measured in 2015.

To measure the absolute light yield, we made three measurements. First, we obtained ADC counts per energy deposit in a module using cosmic rays. Second, we obtained ADC counts per 1-photoelectron signal by using weak LED light. The first and second measurements gave the number of photoelectrons per 1 MeV energy deposit. Because the above two measurements had to be made with different high voltages for PMT, we also measured the gain curve of PMTs.

The measured light yields in units of the number of photoelectrons per MeV are shown in Fig. 6.6. The mean of all the channels of the Main Barrel was (10.39 ± 0.04) p.e./MeV. This result is 70 % of the initial light yield measured before the E391a experiment started [22]. On the other hand, this result was consistent with the measurement we made in 2012. The light yield decreased sometime between the beginning of the E391a experiment and 2012.

6.3.2 Noise level

Noise level was measured as one of the parameters to reproduce the waveform. The noise level was defined as the standard deviation of pedestals. The pedestal in an event was defined as the average of the first 10 samples. Width of pedestals depended on FADC channels as shown in Fig. 6.7. Channels of the Main Barrel and the BCV are arranged

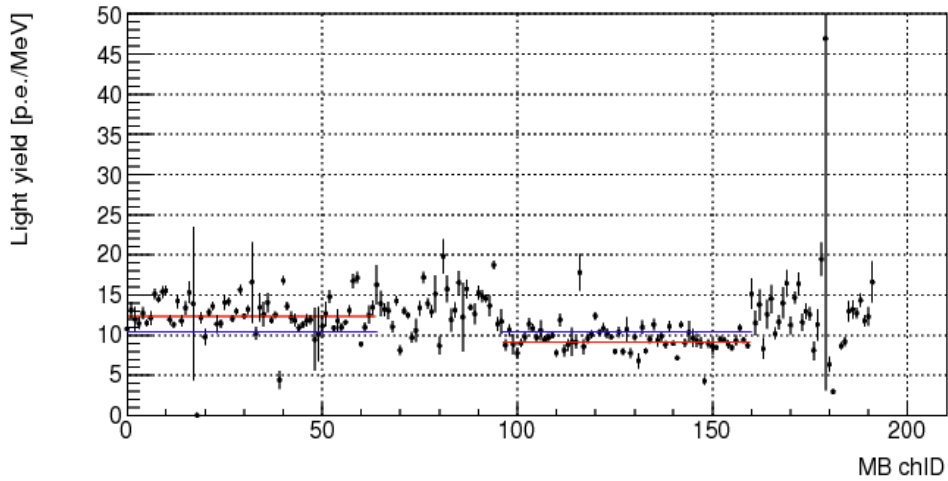


Figure 6.6: Light yields in the units of the number of photoelectrons per MeV for all the channels of the Main Barrel and the Barrel Charged Veto. The light yield is normalized to the value at the center of z direction of modules.

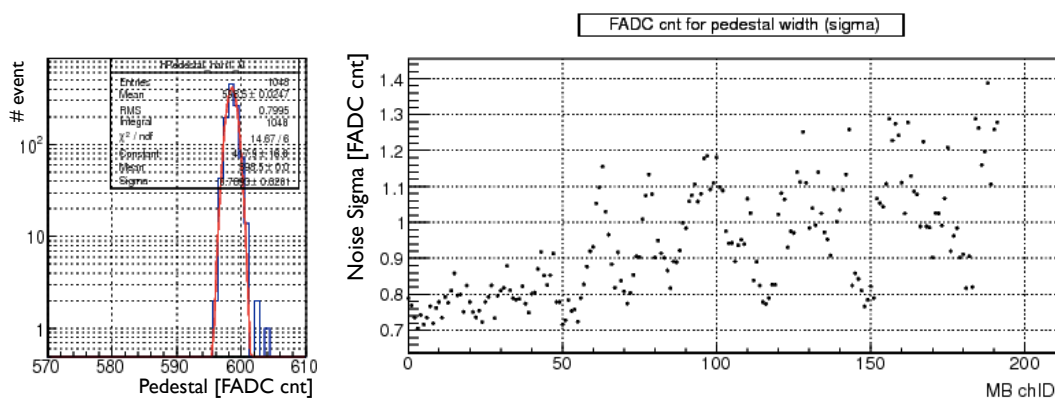


Figure 6.7: Pedestal value defined event by event (left) and the sigma of pedestal distribution at each readout channel (right).

in one FADC crate in order. Latter channels in a 16-channel FADC module and latter FADC modules in the crate containing 14 FADCs had larger noise level. This tendency was common to the KOTO's 125 MHz FADCs.

6.3.3 Waveform of cosmic ray signals

We measured the timing PDF of a Main Barrel module with cosmic ray signals, in the same way as the Inner Barrel. We took the waveform data with a scope in 2012 just before reassembling the detector. The setup is shown in Fig. 6.8.

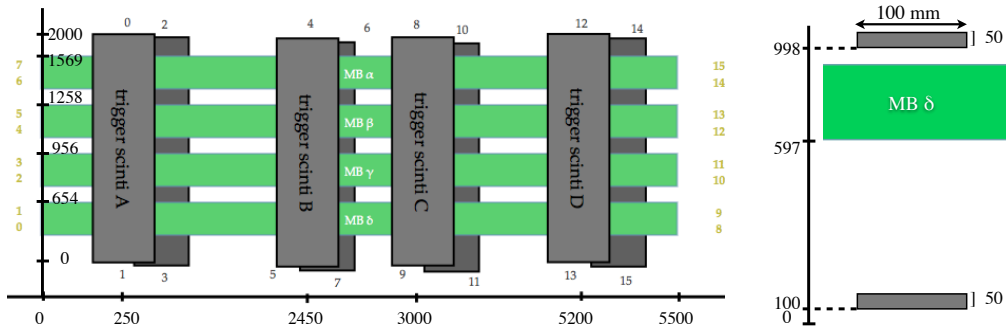


Figure 6.8: Setup to measure the timing PDF of the Main Barrel with cosmic rays. Top view (left) and side view (right) of 4 modules of the Main Barrel and trigger counters are shown. Waveform were taken at the positions of trigger counters A, B, C and D.

The waveforms were shifted and scaled with the same method as for the Inner Barrel described in Section 6.2.2. The typical waveform of a channel is shown in Fig. 6.9.

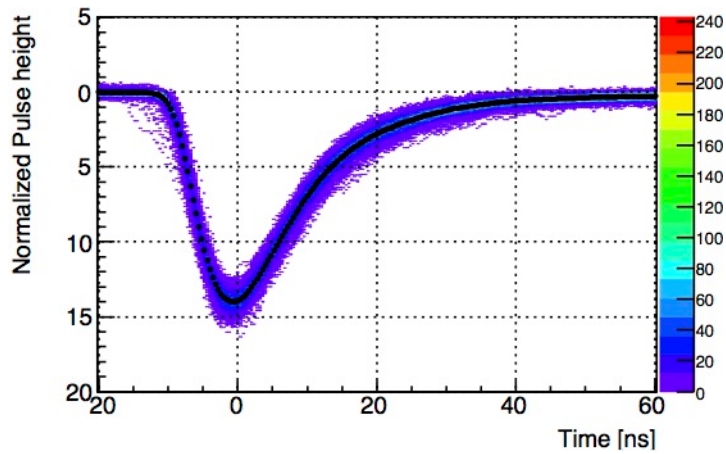


Figure 6.9: Waveform of the Main Barrel taken with a scope. Waveforms were normalized at peak position and overlaid. Black points show the defined typical waveform.

6.4 Estimation of timing resolution

As described in Section 6.1, we extracted timing PDF from waveforms to estimate the timing resolution of the Inner Barrel and the Main Barrel.

6.4.1 Timing PDF extraction

In the process of extraction, we assumed that the timing PDF has a form of an asymmetric gaussian:

$$f(t) = A \exp \left[- \left(\frac{t - \mu}{a(t - \mu) + \sigma} \right)^2 \right] + C, \quad (6.1)$$

where t is time, σ is the width of waveform, a is asymmetric parameter, μ is peak timing, A is pulse height, and C is pedestal level.

The convolution of a timing PDF and the pulse shape of 1-photoelectron signal reproduced the shape of the measured waveform. With the pulse shape of 1-photoelectron signal $W(t)$ measured in Section 6.2.3, the convoluted waveform $H_i^{pdf}(t)$ at timing t_i is described as:

$$H_i^{pdf}(t_i) = \sum_{j=-n}^n f(t_i - j\delta) W(j\delta), \quad (6.2)$$

where δ is pitch of this calculation, and n is the cut-off range. The pitch δ has to be small enough, and n has to be large enough for fluctuation of the convoluted waveform to be negligible.

The convoluted waveform $H_i^{pdf}(t)$ and the measured cosmic ray waveform $H_i^{cos}(t)$ were compared based on a reduced χ^2 defined as:

$$\frac{\chi^2}{NDF} = \frac{1}{N-2} \sum_i^N \frac{(H_i^{cos} - H_i^{pdf})^2}{\alpha_{min} (\sigma_i(H_i^{cos})^2 + \sigma_i(H_i^{pdf})^2)}, \quad (6.3)$$

where N is the number of measured points, $\sigma_i(H)$ is the error of $H(t)$ at each timing t_i , α_{min} is the minimum value of a parameter α to normalize systematic discrepancy between the measured and convoluted waveform. The parameter α is defined as a reduced χ^2 without systematic correction as:

$$\alpha = \frac{1}{N-2} \sum_i^N \frac{(H_i^{cos} - H_i^{pdf})^2}{\sigma_i(H_i^{cos})^2 + \sigma_i(H_i^{pdf})^2}. \quad (6.4)$$

The error $\sigma_i(H)$ includes two definitions. One is $\sigma_i(H_i^{pdf})$ defined from the error of 1-photoelectron measurement. The other is $\sigma_i(H_i^{cos})$ defined from cosmic ray measurements.

The best timing PDF and its parameters σ and a were defined at the minimum χ^2 in Eq. (6.3) as shown in Fig. 6.10. Parameters of timing PDF at best fit for each hit position in the detector is shown in Fig. 6.11. The shape of timing PDF depends on the hit position in the detector. The waveform of hits far from PMT are wider. This

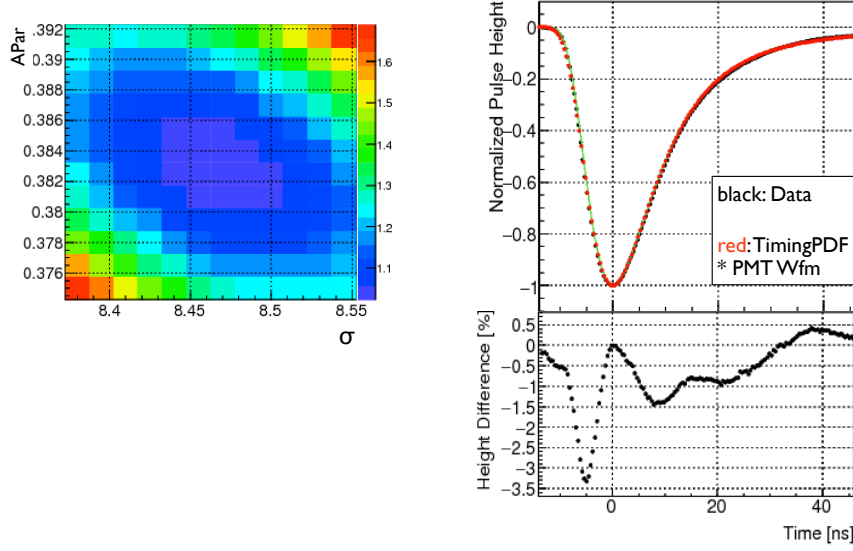


Figure 6.10: Left: The reduced χ^2 used for fitting the timing PDF is shown for asymmetric gaussian width σ (horizontal axis) and asymmetric parameter a (vertical axis). Top right: Waveform at best fit with $\sigma = 8.47$, $a = 0.382$. Bottom right: Difference of the waveform height between data and MC in the top figure.

tendency is reasonable because the propagation time in fiber depends on the emitted photon angle in the fiber. Difference between upstream and downstream readout in the Inner Barrel was considered to be caused by different direction of fiber bundle: straight for upstream and 90° bent for down stream.

6.4.2 Waveform simulation

We reproduced waveforms for the various numbers of photoelectrons using the obtained timing PDF. As described in Section 6.1, we convoluted the timing PDF and the waveform caused by readout systems.

We created the waveforms as follows. First, we created photons at random timing according to the timing PDF. Second, we smeared the timing of each photon to emulate the waveform read out by PMT. This smeared pulse means the distribution of photo-electron readout from PMT, and thus overlaid pulse of all photons means waveform of the signal. Third, we added ground noise to the waveform. For the noise level, we used a gaussian with $\sigma = 0.82$ FADC counts, which is the mean of σ of all the 64 channels of upstream PMTs described in Section 6.3.2. Last, we quantized the pulse hight at a regular interval to match FADC's resolution and sampling frequency. As the FADC's resolution, we used 2.1 FADC counts per a photoelectron based on the measurement of the Main Barrel. As a sampling frequency, we selected 2 or 8 ns pitch for 125 or 500 MHz FADC, respectively. We set random timing offsets within one count not to make bias on the relation between waveform position and FADC count timing.

Samples of generated waveform are shown in Fig. 6.12.

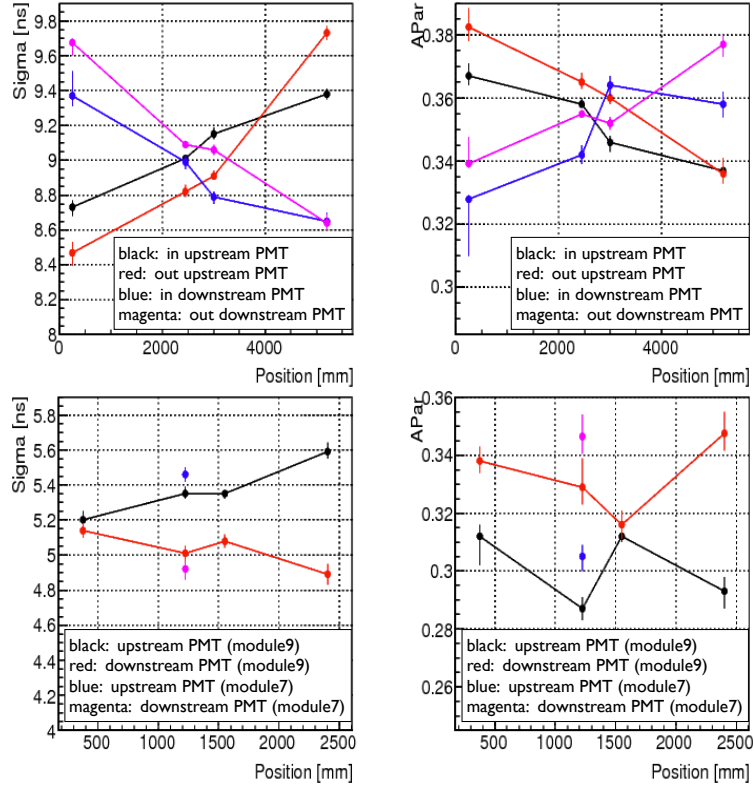


Figure 6.11: Hit position dependence of the timing PDF parameters σ (left) and $\bar{\alpha}$ (right) for the Main Barrel (top) and the Inner Barrel (bottom). The position 0 mm shows the upstream edge of the detector. Error bar at each point indicates the range of reduced $\chi^2 < 1.1$. Colors in the top two plots show the Inner or Outer module, and the upstream or downstream readout PMT: inner and upstream (black), outer and upstream (red), inner and downstream (blue), and outer and downstream (magenta). Colors in the bottom two plots show the upstream or downstream readout PMT for two modules: upstream (black and blue), and downstream (red and magenta).

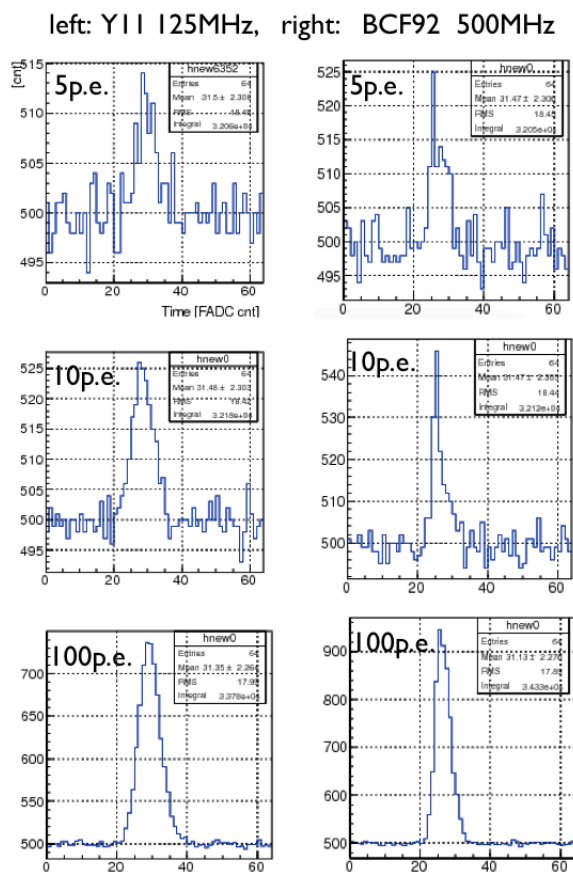


Figure 6.12: Samples of generated waveforms for 5, 10, 100 photoelectrons in the Main Barrel (left) and the Inner Barrel (right). Pedestal was set to 500 counts.

6.4.3 Time defining method

The timing of each event was decided with a waveform and a defining method. We compared 4 defining methods; constant fraction, parabola fitting, asymmetric gaussian fitting, and fixed parameter fitting. We generated waveforms, decided timing, and then estimated timing resolution. The pedestal in each event was defined by averaging the first 10 samples in all four methods. The pedestal value in an event was not affected by a real pulse because the peak position was set at around the 27th sample.

Constant fraction

Constant fraction method [11] decides the timing as the position at half maximum of the highest sample in all the sampling points. A sample of a waveform and its defined timing is shown in Fig. 6.13 (left). After finding the highest sample, adjacent 2 samples crossing half maximum were searched for in the rising slope. On the line connecting these 2 samples, the timing at half maximum height was defined as the constant fraction time. If there were multiple positions crossing the half maximum, the position nearest to the highest sample was defined as the timing.

This method was developed mainly for detectors reading large signal, such as the CsI calorimeter.

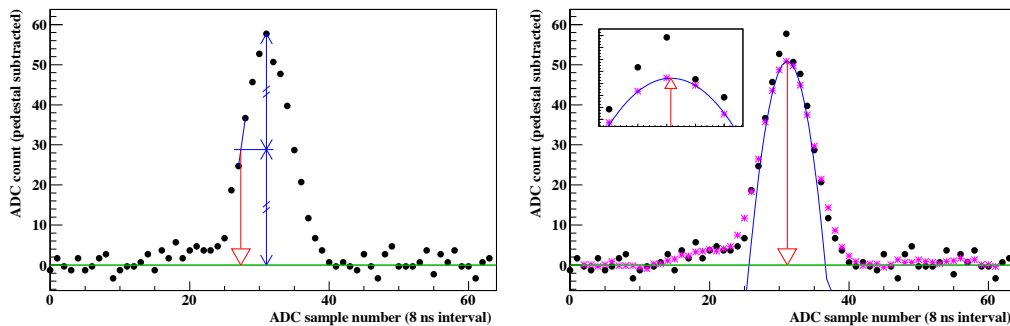


Figure 6.13: An example of defining constant fraction time (left) and parabola fitting time (right). Sampling points are shown in black points. The base lines are shown in green horizontal lines. Red vertical arrows show the decided timings. In the right figure, purple points show moving averages of neighboring 5 sampling points. These figures are taken from [44].

Parabola fitting

Parabola fitting method [44] decides the timing by searching for a local maximum of a pulse. This method was developed for veto detectors not to lose a small pulse at veto timing. For this purpose, the local maximum was required to be around the veto timing. We used this method in the analysis for the 2013 data because we had high accidental hit rates as it will be described in Chapter 7.

In parabola fitting method, the timing was defined as the peak of parabola function. Fitting points were made by making a simple moving average as shown in Fig. 6.13 (right). Each moving average was the mean of the nearest 5 points centered on each the

original sample, and the nearest 3 moving averages were used in parabola function.

This method had three requirements. First, the middle of the 3 moving average points had to be larger than the other 2 points. Second, the middle of 3 moving average points had to be larger than a given threshold. This parabola threshold was set at 10 FADC counts, equivalent to 4.8 p.e., in this analysis in common with the analysis for the 2013 data. Third, parabola peak was required to be close to the nominal timing.

Although parabola fitting method was effective for the 2013 data, there are two issues to be solved in the future. One is the inefficiency of waveforms caused by the parabola threshold shown in Fig. 6.14. The energy threshold for the 2013 data was set to 2 MeV,

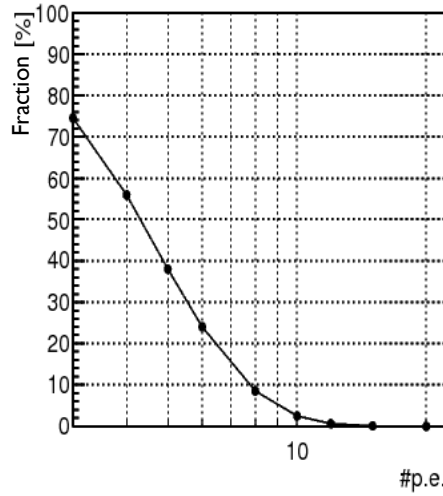


Figure 6.14: The fraction of events that signal is not detected in the Main Barrel.

equivalent to 14 p.e. for the hits near the calorimeter, read from the upstream side. If we lower the energy threshold, event loss increases due to the parabola threshold. The other issue is that the nominal timing cannot be set appropriately for a long detector such as the Main Barrel. For these reasons, we tried another method to prepare for future analysis.

Asymmetric gaussian fitting

We considered another method to separate accidental hits from background hits by fitting the waveform.

Regenerated waveform described in previous subsections can be also fit to an asymmetric gaussian given in Eq. (6.1). We set σ , a , μ and A as fitting parameters, and searched for a waveform. The σ of the convoluted waveform was larger than that of timing PDF because of the distribution of the convoluted 1-photoelectron waveforms. As shown in Fig. 6.15, the fitted σ and a converge toward their certain values for higher number of photoelectrons. Different timing PDF assuming each position in the detector shows a similar convergence. Thus, we conclude that position dependence of waveform in the detector shown in Fig. 6.11 does not affect observed waveforms.

Fixed parameter fitting

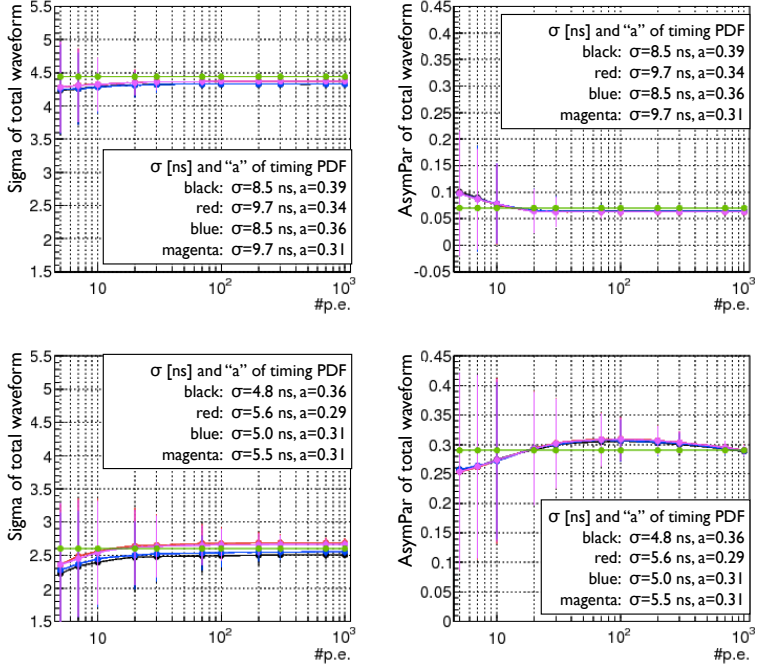


Figure 6.15: Fit parameters of “asymmetric gaussian fitting method” (black, red, blue, and magenta) and “fixed parameter fitting method” (green). The left plots show σ , and the right plots show a , for the Main Barrel (top) and the Inner Barrel (bottom).

Another fitting method called “fixed parameter fitting” kept σ and a in asymmetric gaussian as constant convergent values shown in Fig. 6.15, and assigned only peak timing μ and peak height A as free parameters. This method performed better than the asymmetric gaussian fitting method at low energy, because the fitting function was not sensitive to fluctuated waveform caused by the small number of photoelectrons.

6.4.4 Timing resolution of candidate detectors

Finally, we calculated the timing resolutions with the four described methods. The results are shown in Fig 6.16. When we generated waveforms at each light yield, we chose the actual number of photoelectrons according to Poisson distribution.

The constant fraction timing showed relatively better timing resolution than other methods in high energy region but not in low energy region for 125 MHz FADC. This is because Constant fraction methods is easily influenced by noise fluctuation in low energy region than other methods. Constant fraction method decides the timing from one sample at pulse peak. If the sample is fluctuated, the timing is inaccurate. On the other hand, other methods are less sensitive to pulse shape because the timings are decided from multiple samples by fitting.

A veto detector requires good timing resolution in low energy region. The fixed parameter fitting is a suitable method for the Main Barrel. The parabola fitting is also a suitable method next to the fixed parameter fitting method.

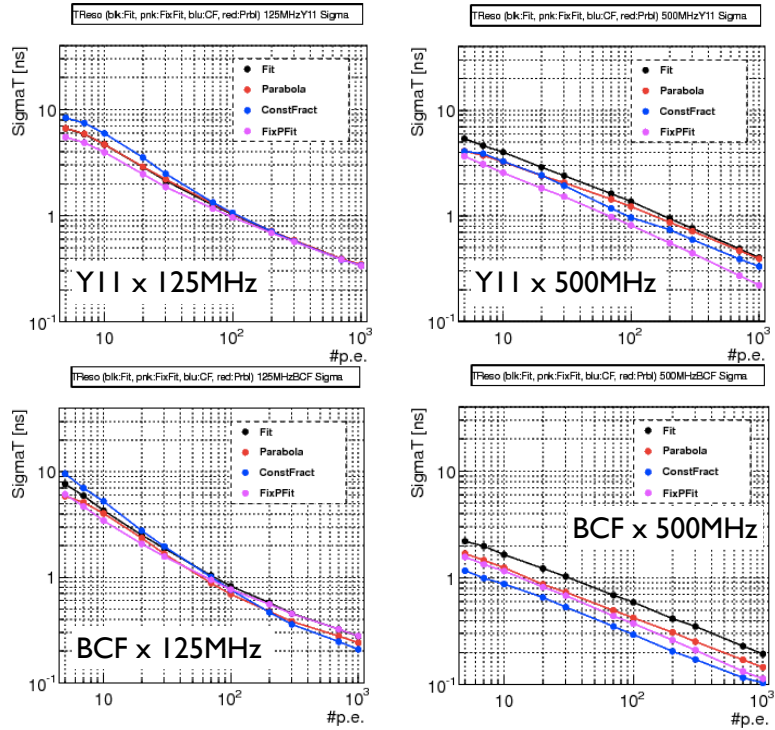


Figure 6.16: The timing resolution of each detector component and readout system evaluated with “asymmetric gaussian fitting method” (black), “parabola fitting method” (red), “constant fraction method” (blue), and “fixed parameter fitting method” (magenta). Each plot shows the combination of fiber types and FADC frequencies: Y11 fiber and 125 MHz FADC (top left), Y11 fiber and 500 MHz FADC (top right), BCF-92 fiber and 125 MHz FADC (bottom left), and BCF-92 fiber and 500 MHz FADC (bottom right).

6.5 Result of light yield and timing resolution of the Inner Barrel and the Main Barrel

Based on the measurements and calculations described in this chapter, we obtained the light yield and the timing resolution caused by detector response.

We compared the estimated timing resolution with the timing resolution measured with cosmic rays. The light yield of the Inner Barrel was (5.6 ± 0.2) p.e./MeV at 5 meter from PMT as described in Section 6.2. Timing resolution of cosmic ray was thus estimated as 0.24 ns with 500 MHz FADC and constant fraction (CF) timing. Compared with the measurement described in Section 6.2, the estimated value was (0.10 ± 0.01) ns smaller than measured value. In all measured energy region, the measured values were systematically higher than the estimation of the Inner Barrel (BCF92 fiber) and 500 MHz FADC using CF timing.

For the Main Barrel, the timing resolution measured with cosmic rays was (0.51 ± 0.02) ns for the inner module and (0.30 ± 0.02) ns for the outer module [45]. The estimated value was 0.1 ns larger than these results for a modules with 10.4 p.e./MeV light yield at the center of the module and a factor $1/\sqrt{2}$ with both-side readout.

In the next chapter, we evaluate the timing resolution mainly in low deposit energy region for the Main Barrel as significant energy region for veto detector.

Chapter 7

Confirmation of timing resolution with the Main Barrel

In the previous chapter, we obtained timing resolution caused by fluctuation of waveform. In this chapter, we evaluate this resolution in low deposit energy region. We apply the resolution in the KOTO Monte Carlo (MC) simulation, and compare MC with the data taken in the KOTO beam line and detector system. We used only the Main Barrel because the Inner Barrel had not been installed at the time of this study.

To evaluate the resolution, we selected 5-cluster events on the CsI calorimeter in the $K_L \rightarrow \pi^0\pi^0\pi^0$ events. This decay mode has 6 gammas in total in the final state. The four-vector-momentum of the 6th gamma was reconstructed by using the 4-vector-momentum of other 5 gammas. If the 6th gamma hits the Main Barrel, its hit timing and position measured by the Main Barrel were compared with those obtained from the 5 gammas on the calorimeter. We evaluated the timing resolution by investigating the difference of measured and reconstructed timings. We used parabola fitting for this evaluation because of the limitation of the analysis flow as following.

7.1 Data set for the analysis

We compared data taken in the May 2013 Run with its MC. The detector setup in the run was the same with that described in Chapter 2.

We used a trigger called normalization trigger. The difference from the usual trigger was that the trigger did not include the selection of Center Of Energy (COE). It means that the trigger did not select P_T . The trigger requires large energy deposit on the CsI calorimeter and no large energy deposit in some veto detectors. The energy deposit in the Main Barrel was required to be less than 50 MeV equivalent.

Data and MC were analyzed in the KOTO analysis scheme shown in Fig. 7.1. We will explain analysis of data and full MC here. The Fast MC has a special analysis scheme as described in Chapter 3. We describe the analysis steps according to the procedures. In each step, we focus on the CsI calorimeter and the Main Barrel.

From Raw to DST (Data)

The first step of the analysis scheme is to convert measured values at each channel to physical quantities.

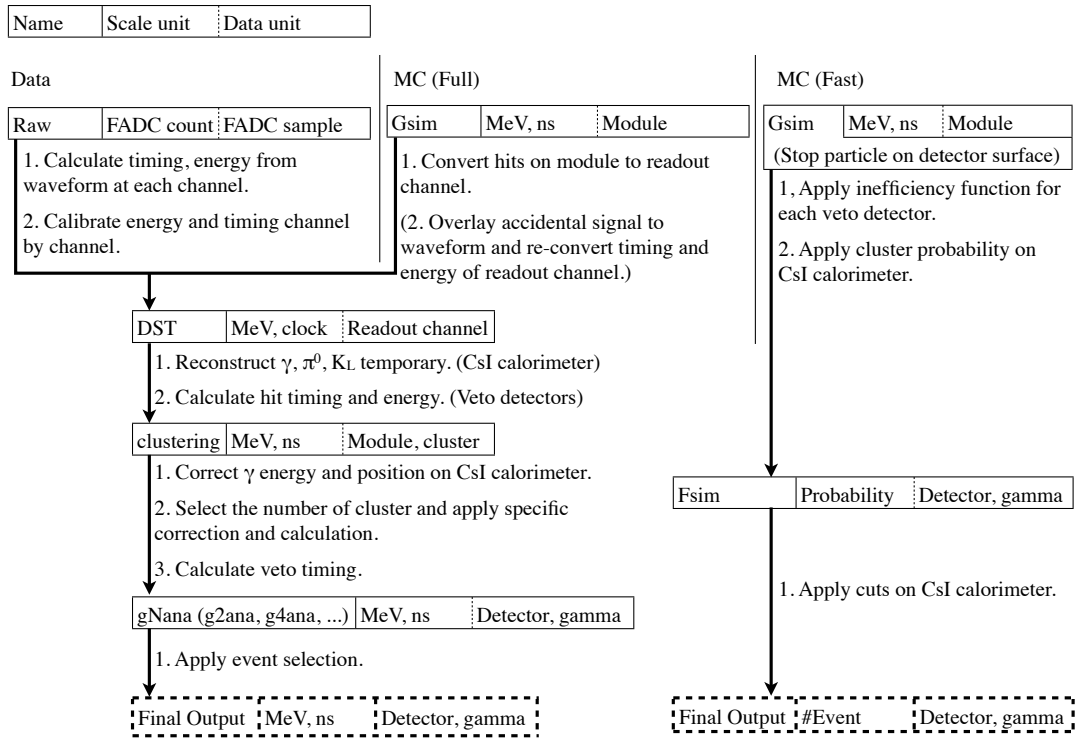


Figure 7.1: The conceptual view of the KOTO analysis scheme. (Some data partially include two types of contents expressed as “data unit”. For instance, Raw data includes not only FADC samples but also integrated ADC.)

The parabola fitting time was calculated for the veto detectors in this step. Raw data already had Constant Fraction time (CFTime) and the sum of all the 64 samples (integrated ADC) after subtracting pedestal. Timing offset decided from CFTime at each channel was also applied to the parabola time.

The Main Barrel used cosmic ray data for the calibration [11]. Nominal timing for the parabola fitting time was defined as one constant value based on the mean of all hitting events.

The waveforms recorded in FADC counts for each sample were not included in DST (data summary tape) data. It was thus difficult to access Raw data to reproduce a timing decided in another timing defining method from the waveform. This was the reason for using the parabola fitting time but not the fixed parameter fitting time in this evaluation.

From Gsim to DST (MC)

In the KOTO Monte Carlo (MC), the hit energy was converted to the observed energy by attenuating the signal based on the hit position.

For the Main Barrel, the hit timing was converted to the observed timing by correcting for the propagation time between the hit position and a PMT. Based on the measurement in the early stage of the KOTO experiment [11], the light attenuation constant was 4920.5 mm, and the propagation velocity was 168.1 mm/ns.

If we add accidental hit samples to MC data, we reproduce a waveform for an original event, and then overlay accidental hit samples on the samples of the waveform. The FADC samples was created temporary in this step and removed from MC DST.

For the Main Barrel, we generated waveforms according to an asymmetric gaussian waveform with $\sigma = 37.416$ ns and $a = 0.08396$. The accidental hit samples were taken by target monitor (TMON) trigger which will be described in Section 7.3. After that, energy and timing were reconstructed from the overlaid samples in the same way as real data.

From DST to clustering

In this step, physical quantities at each readout channel were grouped to each cluster for the CsI calorimeter and each module for veto detectors.

- CsI calorimeter:

Quantities of the cluster; energy $e_{cluster}$, x-position $x_{cluster}$, y-position $y_{cluster}$, and timing $t_{cluster}$, were calculated from the i -th crystal in n crystals contained in the cluster as:

$$e_{cluster} = \sum_{i=1}^n e_i, \quad (7.1)$$

$$x_{cluster} = \frac{\sum_{i=1}^n e_i x_i}{\sum_{i=1}^n e_i}, \quad (7.2)$$

$$y_{cluster} = \frac{\sum_{i=1}^n e_i y_i}{\sum_{i=1}^n e_i}, \quad (7.3)$$

$$t_{cluster} = \frac{\sum_{i=1}^n t_i / \sigma_t^2}{\sum_{i=1}^n 1 / \sigma_t^2}, \quad (7.4)$$

$$\text{and } \sigma_t [\text{ns}] = \frac{5}{e_i [\text{MeV}]} \oplus \frac{3.63}{\sqrt{e_i [\text{MeV}]}} \oplus 0.13, \quad (7.5)$$

where σ_t is the timing resolution for each CsI crystal [32], e_i , x_i , y_i and t_i are the energy, x -position, y -position and timing for the i -th crystal, respectively.

The decay vertex Z_{vtx} was calculated with equations for the π^0 reconstruction shown in Eq. (2.1) and Eq. (2.2) by substituting the gamma energy and position in the equation with the reconstructed cluster energy and position. The decay timing T_{vtx} is calculated from the timing of each cluster in the observed n clusters as:

$$T_{vtx} = \frac{\sum_{k=1}^n T_k / \sigma_T^2}{\sum_{k=1}^n 1 / \sigma_T^2}, \quad (7.6)$$

$$T_k = t_{\text{cluster}(k)} - |\mathbf{r}_k|/c, \quad (7.7)$$

$$\text{and } \sigma_T [\text{ns}] = \frac{3.8}{\sqrt{e_{\text{cluster}(k)} [\text{MeV}]}} \oplus 0.19, \quad (7.8)$$

where σ_T is the timing resolution of a cluster obtained by the $K_L \rightarrow \pi^0 \pi^0 \pi^0$ reconstruction [11], and \mathbf{r}_k is a vector $\mathbf{r}_k = (x_{\text{cluster}(k)}, y_{\text{cluster}(k)}, z_{\text{CsI}} - Z_{vtx})$, which points the cluster position on the calorimeter surface from the vertex position.

- The Main Barrel:

Hit timing T_{DetMB} , z-position Z_{DetMB} , and deposit energy E_{DetMB} were calculated from raw readout energy e_u (e_d) and timing t_u (t_d) read out from upstream (downstream) as:

$$T_{\text{DetMB}} = (t_u + t_d)/2, \quad (7.9)$$

$$Z_{\text{DetMB}} = v(t_u - t_d)/2, \quad (7.10)$$

$$E_{\text{DetMB}} = E_{\text{up}} + E_{\text{down}}, \quad (7.11)$$

$$\text{and } e_d^u = E_{\text{down}}^{\text{up}} \exp \left(\frac{\mp Z_{\text{DetMB}}}{\Lambda \pm \alpha Z_{\text{DetMB}}} \right), \quad (7.12)$$

where $v = 168.1$ mm/ns is propagation velocity, $\Lambda = 4920.5$ mm, $\alpha = 0.495$, and E_{up} (E_{down}) is the readout energy after applying correction for the light attenuation in the detector. These parameters are based on the measurement made in the early stage of the KOTO experiment [11]. The z-position dependence of the measurement for relative light yield is shown in Fig. 7.2.

From clustering to gNana

After we reconstructed clusters and the vertex, we corrected these quantities in the following steps.

First, we corrected the gamma energies and positions. A cluster energy and position depends on the incident angle [46], because cluster shapes have incident angle dependence and the cluster was reconstructed with crystals only with energies above an energy threshold.

Next, we reconstructed the vertex again with the corrected gammas.

If a decay contains multiple π^0 s, such as $K_L \rightarrow \pi^0 \pi^0 \pi^0$ or $K_L \rightarrow \pi^0 \pi^0$, we also used parameters according to the π^0 and K_L reconstructing methods. Each gNana analysis,

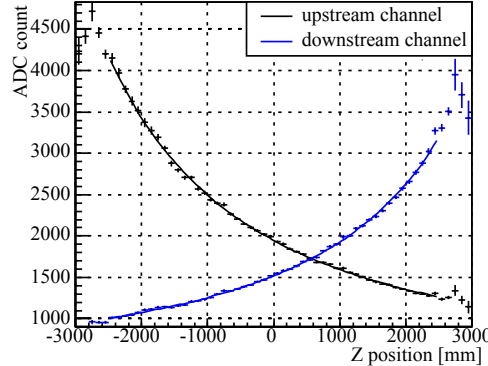


Figure 7.2: The z-position dependence of ADC output at the Main Barrel [11].

which N means the number of clusters, has specific reconstructing methods. The χ^2 for the vertex reconstruction was used to select the best combination to reconstruct K_L . The decay vertex Z_{K_L} and the χ_Z^2 are calculated as:

$$Z_{K_L} = \frac{\sum_{k=1}^m Z_{vtx(k)} / \sigma_{Z(k)}^2}{\sum_{k=1}^{n/2} 1 / \sigma_{Z(k)}^2}, \quad (7.13)$$

$$\chi_Z^2 = \sum_{k=1}^m \frac{(Z_{vtx(k)} - Z_{K_L})^2}{\sigma_{Z(k)}^2}, \quad (7.14)$$

where m is the number of reconstructed π^0 's, $Z_{vtx(k)}$ is the reconstructed vertex from the k -th π^0 , and σ_Z is the z-position resolution calculated from the energies of the gamma pairs. The decay timing T_{K_L} is calculated again with Eq. (7.6), using the reconstructed Z_{K_L} instead of Z_{vtx} in the definition of the vector \mathbf{r}_k in Eq. (7.7).

Last, veto timing according to the vertex position and timing were calculated. For the Main Barrel, the veto timing t_{MB} was calculated as:

$$t_{MB} = (T_{DetMB} - TOF_{MB}) - T_{vtx}, \quad (7.15)$$

$$TOF_{MB} = \sqrt{r_{MB}^2 + (Z_{DetMB} - Z_{vtx})^2 / c}, \quad (7.16)$$

where TOF_{MB} is the time of flight from the vertex to the Main Barrel surface, and r_{MB} is the radius of the Main Barrel surface defined as 1018 mm for inner module and 1118 mm for outer module. Hit timing T_{DetMB} and z-position Z_{DetMB} are defined in Eq. (7.9) and Eq. (7.10), and vertex time T_{vtx} is defined in Eq. (7.6).

From gNdata to final output

In this step, we apply vetoes and kinematic cuts.

Veto at the Main Barrel in the standard analysis for the May 2013 data required > 2 MeV energy deposit within ± 30 ns of veto timing. We used the energy deposit in the module having the largest energy deposit for veto.

Events are selected based on the values measured at the CsI calorimeter. Parameters for cluster quality common in gNana are the followings.

E_γ : Gamma energy as a cluster $e_{cluster}$ finally obtained after corrections.

Fiducial XY: Distance from the beam hole at $|x_{cluster}|$ and $|y_{cluster}|$.

Fiducial R: Distance from outer edge of the calorimeter at $R = \sqrt{x_{cluster}^2 + y_{cluster}^2}$.

Cluster distance: Distance between clusters to ensure that one cluster is originated from only one gamma.

7.2 5-gamma pointing method

The 5-cluster events were treated in g5ana, and specific reconstructing methods and cut conditions were applied. Procedure to reconstruct four momentum of the 6th gamma from other 5 gammas is the following.

First, we reconstructed 2 π^0 's from 4 clusters in 5 clusters hitting the calorimeter. The best combination was selected to be the one with the smallest vertex χ^2 represented in Eq. (7.14). With the selected combination, momentum of 5 gammas, the vertex Z_{KL} , and the timing T_{KL} were decided.

Second, by assuming $P_T = 0$ for the K_L and the π^0 mass for 3rd π^0 , the 6th gamma was temporary reconstructed as:

$$p_{6(x)} = - \sum_{i=1}^5 p_{i(x)}, \quad (7.17)$$

$$p_{6(y)} = - \sum_{i=1}^5 p_{i(y)}, \quad (7.18)$$

$$M_{Rec\pi^0}^2 = (|\mathbf{p}_5| + |\mathbf{p}_6|)^2 - (\mathbf{p}_5 + \mathbf{p}_6)^2, \quad (7.19)$$

where $\mathbf{p}_i = (p_{i(x)}, p_{i(y)}, p_{i(z)})$ is a three-momentum of the i -th gamma, and $M_{Rec\pi^0}$ is the reconstructed π^0 mass. Equation (7.19) is a quadratic equation about $p_{6(z)}$. Applying the nominal π^0 mass to $M_{Rec\pi^0}$, we obtained two answers for $p_{6(z)}$. The K_L mass M_{RecK_L} was reconstructed as:

$$M_{RecK_L}^2 = \left(\sum_{i=1}^6 |\mathbf{p}_i| \right)^2 - \left(\sum_{i=1}^6 \mathbf{p}_i \right)^2. \quad (7.20)$$

Third, these \mathbf{p}_6 , $M_{Rec\pi^0}$, and M_{RecK_L} were corrected by minimizing the χ^2 :

$$\chi^2_{Rec}(p_{6(x)}, p_{6(y)}, p_{6(z)}) = \frac{(M_{RecK_L} - M_{K_L})^2}{\sigma_{K_L}^2} + \frac{(M_{Rec\pi^0} - M_{\pi^0})^2}{\sigma_{\pi^0}^2} + \frac{p_{xSum}^2}{\sigma_{p_x}^2} + \frac{p_{ySum}^2}{\sigma_{p_y}^2} \quad (7.21)$$

where M_{K_L} (M_{π^0}) is the nominal K_L (π^0) mass, p_{xSum} (p_{ySum}) is the sum of six gammas' x (y) momentum, and σ_{K_L} , σ_{π^0} , σ_{p_x} and σ_{p_y} are the errors of M_{RecK_L} , $M_{Rec\pi^0}$, p_{xSum} and p_{ySum} , respectively. Three-momentum of the 6th gamma was a free parameters for the fitting.

Last, veto timing and hit z-position of the 6th gamma are defined as:

$$t_{Rec} = T_{K_L}, \quad (7.22)$$

$$z_{Rec} = Z_{K_L} + l_{MB} \frac{\mathbf{p}_6 \cdot \mathbf{e}_z}{|\mathbf{p}_6|}, \quad (7.23)$$

where l_{MB} is the path length from the vertex to the hit position at the inner radius $r_{MB} = 1018$ mm of the inner module of the Main Barrel, \mathbf{p}_6 is the momentum of the 6th gamma, and \mathbf{e}_z is a unit vector pointing z-direction.

Kinematic cuts for selecting 5-gamma events are listed in Appendix A.

7.3 Contamination of accidental hits

Accidental hits were investigated during the May 2013 Run with Target Monitor (TMON) trigger data. The TMON was a hodoscope to monitor the yield of secondary particles created at the T1 target. It detected particles toward 50° direction from the primary beam line. The timing of the TMON trigger was adjusted to the K_L beam events at the KOTO detector. The counting rate at each module of the Main Barrel and deposit energy distribution are shown in Fig. 7.3. Higher accidental hit rate were shown in the

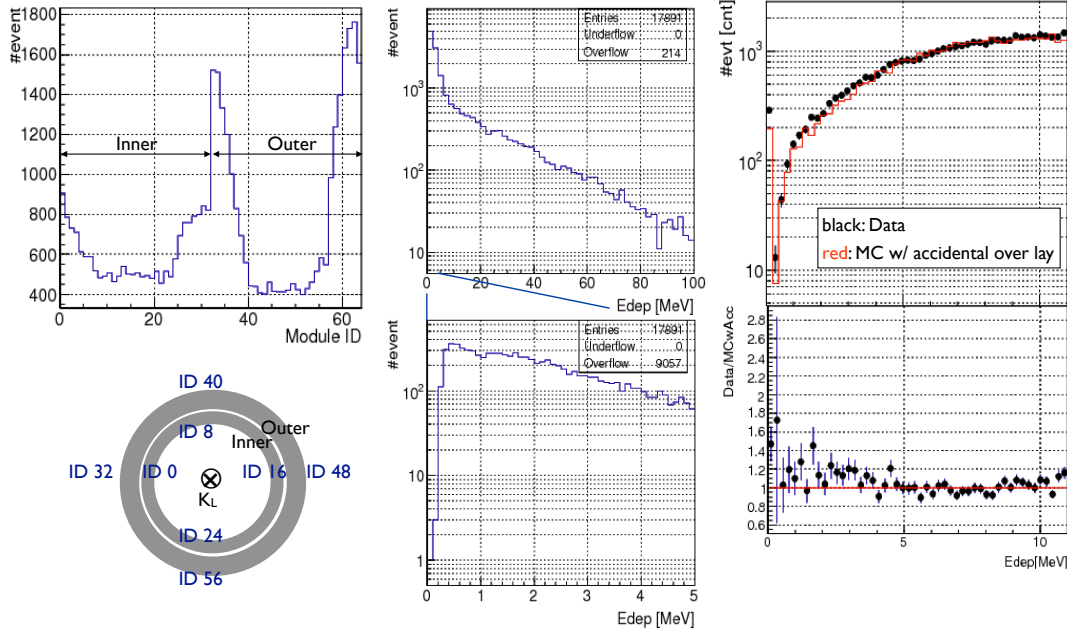


Figure 7.3: Left: Signal counting rate at each Main Barrel module. Center: The largest energy deposit in the modules of the Main Barrel for TMON trigger data. Right: The deposit energy distribution of 6th gamma hitting the Main Barrel for data and MC with accidental overlay. Module ID shown in the bottom left figure was numbered in a clockwise direction viewed from upstream from the near primary beam side for inner 32 modules and later outer 32 modules. Therefore, ID 0 and 31 for the inner modules, 32 and 63 for the outer modules were placed near the primary beam line.

side modules near the primary beam line. We suspected that neutrons from the primary

beam line downstream of T1 target hit the modules. We thus dealt with the particles by water and iron shield and tuning of RF modulation. By tuning of RF modulation, the different arrival timing between K_L and neutron can change their ratio around the KOTO detector.

By overlaying the waveforms observed in TMON trigger on the waveforms of MC events, we could compare data with MC in a realistic beam accidental rate condition. We call this method the accidental overlay. Events analyzed with 5-gamma pointing method had a 10 % acceptance reduction by the accidental overlay. In the following analysis to measure the timing resolution with 5-gamma events, we used MC events with accidental overlay.

7.4 Measured timing resolution

We evaluated timing resolution with the distribution of difference of the detected and reconstructed timing. In the same way, we also evaluated the z-position resolution, which is closely related to the timing resolution. The definitions of each timing and z-position were as follow.

The hit timing difference T between veto timing t_{MB} in Eq. (7.15) and reconstructed timing t_{Rec} in Eq. (7.22) is described as:

$$T = t_{MB} - t_{Rec} \quad (7.24)$$

$$= T_{DetMB} - TOF_{MB} - T_{vtx} - T_{K_L} \quad (7.25)$$

$$= T_{DetMB} - TOF_{MB} - 2T_{vtx}. \quad (7.26)$$

The position difference Z between detected position Z_{DetMB} in Eq. (7.10) and reconstructed hit position z_{Rec} in Eq. (7.23) is:

$$Z = Z_{DetMB} - z_{Rec}. \quad (7.27)$$

The relation between the detected position Z_{DetMB} and reconstructed hit position z_{Rec} in the KOTO data is shown in Fig. 7.4.

From Eq. (7.9) and Eq. (7.10), the detected z-position resolution $\sigma_{z_{Rec}}$ is proportional to the detected timing resolution $\sigma_{t_{Det}}$ as:

$$\sigma_{z_{Rec}} = v\sigma_{t_{Det}}. \quad (7.28)$$

The resolution of T and Z are:

$$\sigma_T = \sigma_{t_{Det}} \oplus \sigma_{t_{TOF}} \oplus (\sqrt{2}\sigma_{t_{vtx}}), \quad (7.29)$$

$$\sigma_Z = \sigma_{z_{Det}} \oplus \sigma_{z_{Rec}}, \quad (7.30)$$

$$= v\sigma_{t_{Det}} \oplus \sigma_{z_{Rec}}, \quad (7.31)$$

where $\sigma_{t_{TOF}}$, $\sigma_{t_{vtx}}$, and $\sigma_{z_{Rec}}$ are the resolutions of TOF_{MB} , T_{vtx} , and z_{Rec} , respectively.

The data taken in the experiment contains the timing and z-position resolutions caused by the waveform described in Section 6.4. We added such resolution in the MC. The resolution of data, and that of MC with and without waveform contribution are shown in Fig. 7.5.

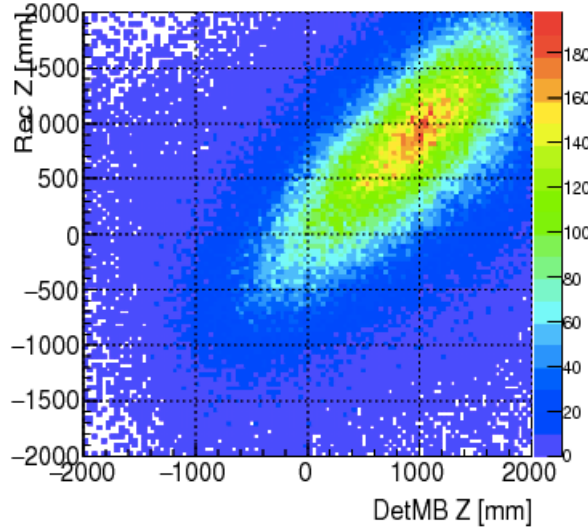


Figure 7.4: Detected and reconstructed z-positions. The $Z = 0$ mm is defined as the center of the Main Barrel.

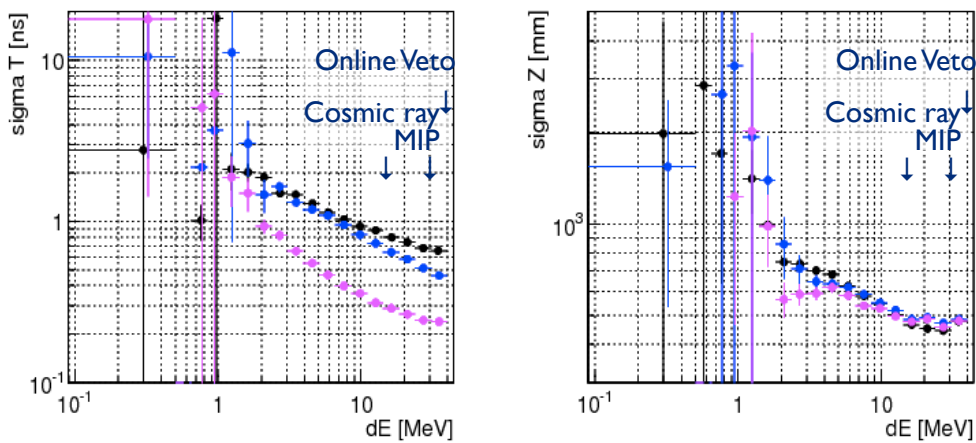


Figure 7.5: The width σ_T (left) and σ_Z (right) at each deposit energy region. Each color shows data (black) and MC with (blue) and without (magenta) resolution caused by waveform.

In the figure, the discrepancy between data and MC was reduced after the resolution caused by the waveform was added, as visible by comparing these three σ_T 's. In other words, the effect of the waveform was the main contribution in the timing resolution observed in data. This effect was included in $\sigma_{t\text{Det}}$ term in Eq. (7.29).

On the other hand, the z-position resolutions are not different between data and MC with and without waveform contribution. This means that the fluctuation of the reconstructed z-position is the main contribution in the z-position resolution observed in data.

Chapter 8

Optimization of veto window and threshold

The veto windows and thresholds for the Main Barrel and the Inner Barrel should be adjusted to maximize the sensitivity of the experiment. We evaluated the sensitivity with a significance S/\sqrt{B} , where S and B are the number of signal and $K_L \rightarrow \pi^0\pi^0$ background events, respectively.

In Chapter 4, we estimated the signal to background ratio (S/B) without considering the timing resolution. In this chapter, we re-estimate the signal and noise with the realistic timing resolution we obtained in Chapter 6, and evaluate the significance.

To reproduce realistic relative timings between the Inner Barrel, the Main Barrel, and the CsI calorimeter, in the following analysis, we used MC set for the May 2013 data analysis which included the timing response in the calorimeter.

At the first physics run, we also learned that there were several issues to be solved for the further progress of the KOTO experiment. One of the issues was the large accidental loss. Dependence of the accidental event rate on beam intensity and the estimation for future condition are described in Section 8.2. Another issue was the statistics of MC. Both Fast and Full MC had difficulties for future analysis. The data size of Full MC is too large to generate large number of events. Fast MC had some discrepancy between Full MC for the estimated number of background events. Detail of these issues and a trial of another MC method will be described in Section 8.3.

Beforehand, in this and next chapters, we call the barrel detectors after installing the Inner Barrel as “middle-stream Barrel detectors” to express the Main Barrel and the Inner Barrel working together.

8.1 $K_L \rightarrow \pi^0\nu\bar{\nu}$ analysis

In this section, we will obtain the number of the $K_L \rightarrow \pi^0\nu\bar{\nu}$ signal events, and its dependence on veto width and energy threshold caused by back-splash.

8.1.1 Analysis method

To study the effect of the barrel detectors on the sensitivity for the $K_L \rightarrow \pi^0\nu\bar{\nu}$, we generated Full MC without beam accidental overlay. Most parts of the analysis method

for the $K_L \rightarrow \pi^0 \nu \bar{\nu}$ mode were common with the 5-cluster analysis in the $K_L \rightarrow \pi^0 \pi^0 \pi^0$ mode described in Chapter 7. The main difference from the 5-cluster analysis was the cuts to avoid vertex mis-reconstruction. In 2-cluster analysis, we reconstruct only one π^0 vertex for the $K_L \rightarrow \pi^0 \nu \bar{\nu}$ mode. The cuts are listed in Appendix A. Most of cuts were the same as the analysis for the May 2013 data, without cuts for neutron backgrounds such as Neural Net cuts.

8.1.2 Number of signal events

The single event sensitivity (S.E.S) is defined as:

$$S.E.S. = \frac{1}{N_{KL} \times \epsilon_{sig}}, \quad (8.1)$$

where N_{KL} is the total number of the incident K_L 's and ϵ_{sig} is the signal acceptance including decay probability of the incident K_L . In this analysis, the signal acceptance after applying all the cuts including the Main Barrel veto at 2 MeV threshold was 2.1×10^{-3} without a beam accidental loss. In this study, I assumed that the total number of protons on target (P.O.T.) is 1.3×10^{21} , the loss of acceptance is 50 % due to accidental hits, and another 50 % due to cuts to suppress the neutron backgrounds. We assumed $N_{KL} = 2.8 \times 10^{14}$ based on the K_L flux $F_{KL} = (4.041 \pm 0.109) \times 10^7$ per 2×10^{14} P.O.T from the result of K_L measurement [47]. The S.E.S. is equivalent to 6.9×10^{-12} . With this S.E.S., the number of the Standard Model signal events is 3.5.

8.1.3 Timing and z position distribution of back-splash

Timing and z-position distributions of the backsplash particles hitting the barrel detectors in the $K_L \rightarrow \pi^0 \nu \bar{\nu}$ mode are shown in Fig. 8.1. The backsplash particles hit the

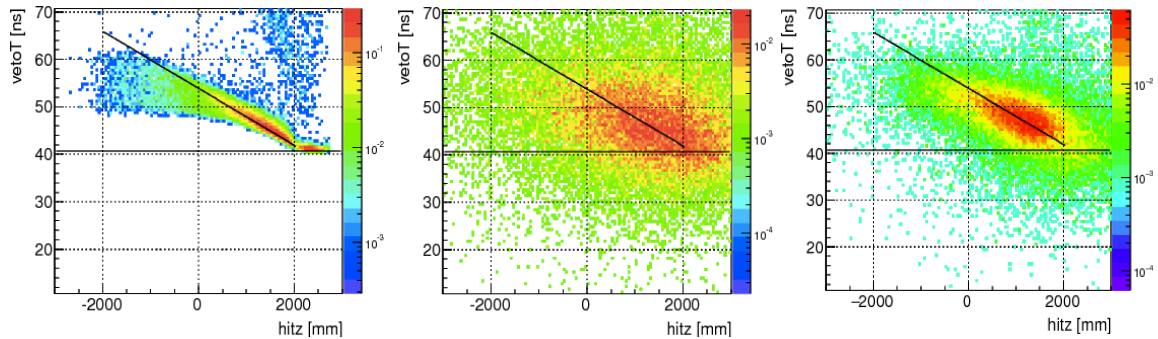


Figure 8.1: Timing and z-position distributions of the largest energy deposit of the backsplash particles hitting the barrel detectors in the $K_L \rightarrow \pi^0 \nu \bar{\nu}$ mode. Full simulation without timing and z-position smearing (left), that with smearing for the Main Barrel (center), and that with smearing for the middle-stream Barrel detectors (right). The flat line ($vetoT = 40.7$) shows the veto timing. The black shallow line ($vetoT = -5.67 \times 10^{-3}z + 53.93$) shows the mean timing of back-splash events.

barrel detectors after the veto timing. Late shower events around $z_{hit} = 2000$ mm shown in Fig 8.1 (left) were caused by photo-nuclear interaction in the CsI calorimeter.

As already shown in Fig. 3.10, 28 % of observed signal events had back-splash hits in the middle-stream Barrel detectors, and the deposit energies in 99 % of these events were less than 5 MeV. Because the timing resolution is large at low energy, the reconstructed timing and z-position have a broad distribution.

8.2 Beam accidental event

As described in Chapter 7, the May 2013 data had high rate of accidental events hitting the Main Barrel. Beam accidental hits will be reduced by shielding and beam tuning. I thus studied accidental hits estimated from the K_L beam line MC for future beam conditions. Besides, we estimated the signal loss caused by accidental hits in various beam intensities by scaling the counting rate.

8.2.1 Requirement for acceptance

Before estimating the signal loss due to accidental hits, we mention the relation of signal counting rate to the signal collecting efficiency, that is the yield of collected signal event, and Data Acquisition (DAQ) system. The yield of signal events Y is described as:

$$Y = N_K \times P_{live} \times A_{sig}, \quad (8.2)$$

where N_K is the number of K_L 's which satisfies the trigger condition per spill, P_{live} is the probability that the DAQ can accept triggers (live ratio), and A_{sig} is the fraction of the events without accidental hits in the triggered events. The live ratio is expressed as:

$$P_{live} = \frac{1}{1 + N_K \times w_{DAQ}/w_{sp}}, \quad (8.3)$$

where w_{DAQ} is dead time of the DAQ system for an event, and w_{sp} is the spill length. By assuming that the accidental hit timing is flat, the probability that a selected event has no accidental hits is:

$$A_{sig} = Poisson(0, N_{acd}), \quad (8.4)$$

where N_{acd} is the expected number of accidental hits in a trigger on the barrel detectors. The Poisson distribution was defined in Eq. (4.8).

If $N_{acd} \lesssim 0.1$, we can regard $R_{acd} = 1 - Poisson(0, N_{acd}) \simeq N_{acd}$, where R_{acd} is the fraction of events with accidental hit per one K_L in the barrel detectors. Figure 8.2 shows the signal yield as a function of the intensity at the same 2 sec spill and 6 sec beam cycle. Here, we assumed 10 % ($R_{acd} = 0.1$) and 3% ($R_{acd} = 0.03$) acceptance loss at 24 kW beam intensity, and no advanced trigger to reduce N_K less than that for > 24 kW beam intensity. If the acceptance loss is 10 % at 24 kW, and if the condition did not improve, the efficiency of data acquisition system reaches a plateau near 100 kW beam intensity. As described in Chapter 7, there was a 10 % loss in 5-cluster events at 24 kW beam power. Therefore, accidental event rate lower than May 2013 Run is required for efficient data taking in future high intensity beam at ~ 100 kW. Study to reduce accidental hits is underway. We thus should study the acceptance loss and the achievable sensitivity after the accidental rate is reduced.

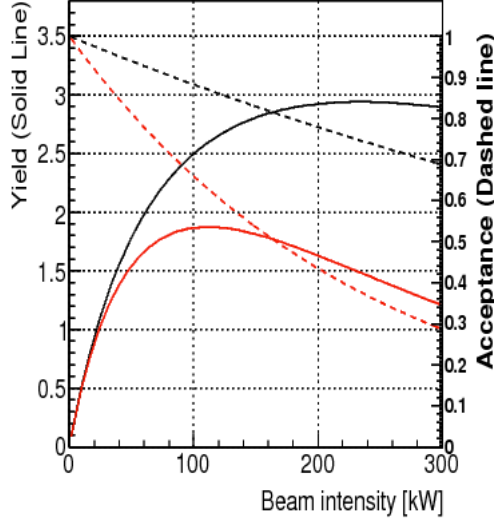


Figure 8.2: Factor of acceptance and signal yield as a function of beam intensity for 10 % (red) and 3% (black) acceptance loss at 24 kW beam intensity. Signal yield is normalized by that at 24 kW beam intensity. Beam cycle is assumed to be 2 sec spill and 6 sec beam cycle as in May 2013.

8.2.2 Beam Monte Carlo

In beam Monte Carlo simulation, particles with momentum $> 100 \text{ MeV}/c$ were generated as sources of accidental events. The particles which were produced in a 66-mm-long gold target and passed the collimators downstream of T1 target were collected. The types of generated particles and deposit energy distribution caused by each source particle are shown in Fig. 8.3. Most particles hitting the Main Barrel were particles decayed from the K_L . Table 8.1 shows the rate that a particle deposits energy higher than a given threshold in the Main Barrel.

8.2.3 Event loss expectation

We counted the number of accidental hits reproduced in MC in a trigger width as:

$$N_{acd} = f_{KL} \times \frac{w_{veto}}{w_{sp}} \times n_{acd}, \quad (8.5)$$

where f_{KL} is a factor of the flux of K_L , w_{veto} is veto width, w_{sp} is spill length. The n_{acd} is the number of accidental hits per one K_L but includes hits of particles produced by gamma and neutrons.

Width of veto window w_{veto} is assumed to be 60 ns which is the same as in the May 2013 data analysis. We scaled f_{KL} by P.O.T based on $F_{KL, Full} = (4.041 \pm 0.109) \times 10^7$ per 2×10^{14} P.O.T [47].

In future, the beam power will be increased to 100 kW. Repetition cycle is shortened to be 4 seconds from 6 seconds without altering the 2 seconds spill length by replacing power supply for J-PARC Main Ring [48]. In this 4-seconds cycle, acceptance become better than that in 6-seconds cycle at the same beam power.

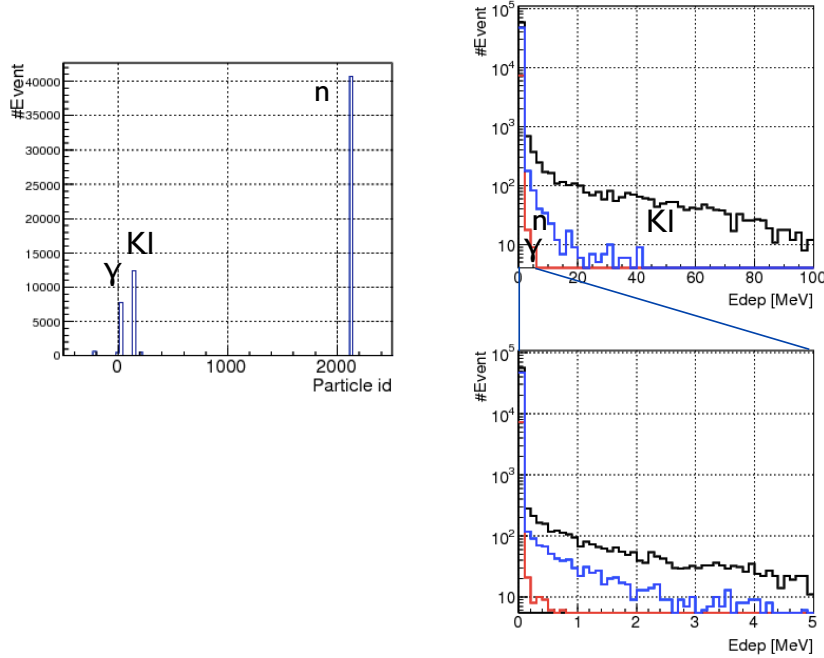


Figure 8.3: Generated particle id (left) and deposit energy on the Main Barrel for each source particle (right).

Table 8.1: Accidental event rate (n_{acd}) estimated from beam MC for the flux $F_{KL Full}$.

Threshold	Accidental Rate [evt/ K_L]	
	$E_{dep} >$ Threshold	$5 > E_{dep} >$ Threshold
2 MeV	0.323	0.072
1 MeV	0.374	0.123
0.5 MeV	0.418	0.167

If the veto window is narrowed to w_{new} , the signal acceptance A_{sig} is changed to:

$$A_{sig} = \text{Poisson}(0, N_{acd} \times \frac{w_{new}}{w_{veto}}). \quad (8.6)$$

Veto width dependence of the A_{sig} is shown in Fig. 8.4. The figure also shows the case if

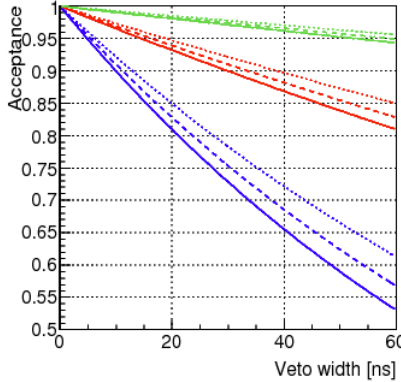


Figure 8.4: A_{sig} as a function of width of veto window for 24 kW 6-second beam cycle (green), 100 kW 4-second beam cycle (red), and a factor 3 higher accidental hit rate in 100 kW 4-second beam cycle (blue). Each line style shows the acceptance for thresholds at 2 MeV (dotted line), 1 MeV (dashed line), and 0.5 (solid line), respectively.

the beam line condition is not improved and the accidental hit rate was 3 times higher.

8.3 MC method for background estimation

In the $K_L \rightarrow \pi^0\pi^0$ background study, we tried a new method different from Full and Fast MC. In the method, to reduce the statistical fluctuation, deposit energy of an event is reproduced by a probability distribution as a function of the incident gamma energy and angle. Timing is reproduced by interaction timings and the spread from it. The timing spread is calculated by a convolution of the timing resolution and the probability distribution of the deposit energy because the timing resolution is a function of the deposit energy. The timing spread is thus a probability distribution. The z-position are reproduced in the same way to the timing.

In this section, we describe the merit of the method, its approach, and evaluation of the method.

8.3.1 Feature and merit of mapping method

In the May 2013 data analysis, the number of the $K_L \rightarrow \pi^0\pi^0$ background events was estimated with Full MC. This analysis also used this Full MC, and the statistics was equivalent to generating K_L 's which would give 5.2×10^{-11} S.E.S for signal events. However, a few events depositing less than 5 MeV in the Main Barrel remained. To study further reduction, higher statistics was required.

On the other hand, we wanted smaller MC size per event for future analysis. The simulated events of all studied decay modes for the May 2013 data analysis already

occupied 14 TB of disk space (only for raw level format). We are going to collect 10^3 times more experimental data, and the MC size will increase in proportion to the data size. Current MC event size is too large to analyze speedy due to the limitation of CPU power and disk access speed.

With Fast MC, we could generate the events with small event size. The $K_L \rightarrow \pi^0\pi^0\pi^0$ decay mode which had larger branching ratio than the $K_L \rightarrow \pi^0\pi^0$ decay mode was generated with Fast MC. The $K_L \rightarrow \pi^0\pi^0$ decay mode was also generated in Fast MC as the reference. The number of the $K_L \rightarrow \pi^0\pi^0$ background events estimated with Fast MC was twice smaller than that with Full MC.

For these reasons, I developed another method to estimate the number of background events accurately with small event size.

The new method, named mapping method, is similar to Fast MC but can evaluate the deposit energy distribution. In Fast MC, we defined only one energy threshold and only judged whether the energy deposit was larger than the threshold or not. The merit of seeing the deposit energy distribution is that we can compare the distributions between MC and data, and can understand systematically the difference of the event properties between them.

In addition, we can also reproduce timing distribution by obtaining energy distribution as follows. To obtain timing distribution including detector response, we smeared the timing according to detector timing resolution. Because the detector timing resolution is a function of deposit energy, we need deposit energy. This is the reason why the timing could not be smeared in Fast MC but could be in the mapping method.

In the followings, we explain energy, timing, and z-position calculation in the mapping method. After that, we compare the energy deposit obtained with the mapping method and with Full MC to confirm the accuracy of the method itself. This confirmation was done under loose cut condition to increase statistics. Finally, we apply all the cuts to the mapping method and evaluate the number of background events.

8.3.2 approach of mapping method

In the mapping method, we treated energy, timing, and z-position information differently from Fast and Full MC.

For energy, we used only the K_L decay kinematics in the same way as the Fast MC. The result of monochromatic gamma MC used to make inefficiency function was reused to obtain energy deposit distribution. In the Fast MC, the inefficiency function I was a function of incident angle θ_{in} and incident energy E_{in} ; $I = I(\theta_{in}, E_{in})$. Instead of inefficiency function, we prepared a gamma response function $F[E_{dep}] = F(\theta_{in}, E_{in}, E_{dep})$ for the mapping method. Gamma response function is a function (array) of the probability of energy deposit between E_{dep} and $E_{dep} + \Delta E$ for a gamma with the incident energy E_{in} entering a detector with angle θ . The function can also be interpreted as the difference of inefficiencies between two near thresholds as:

$$F(\theta, E_{in}, E_{dep})\Delta E = I_{(thre=E_{dep}+\Delta E)}(\theta, E_{in}) - I_{(threshold=E_{dep})}(\theta, E_{in}). \quad (8.7)$$

The function is also normalized:

$$\int_{x=0}^{\infty} F(\theta, E_{in}, x)dx = 1. \quad (8.8)$$

If two particles hit the detector, we used the maximum deposit energy in one module to make a veto decision. We neglected the effect that two gammas hit the same module because the effect was only 3 %. The distribution of maximum deposit energy is then:

$$\begin{aligned} F_{total}(E_{dep}) &= \int_{x=0}^{E_{dep}} F_1(\theta, E_{in}, x) dx \ F_2(\theta, E_{in}, E_{dep}) \\ &\quad + F_1(\theta, E_{in}, E_{dep}) \int_{x=0}^{E_{dep}} F_2(\theta, E_{in}, x) dx \\ &\quad + F_1(\theta, E_{in}, E_{dep}) F_2(\theta, E_{in}, E_{dep}) \end{aligned} \quad (8.9)$$

$$= I_1 F_2 + F_1 I_2 + F_1 F_2 \quad (8.10)$$

Similarly, if three particles hit the detector, the distribution of maximum energy deposit is described as:

$$F_{total}(E_{dep}) = I_1 I_2 F_3 + I_1 F_2 I_3 + F_1 I_2 I_3 + I_1 F_2 F_3 + F_1 I_2 F_3 + F_1 F_2 I_3 + F_1 F_2 F_3 \quad (8.11)$$

The timing and z-position were smeared with the timing and z-position resolution, respectively. As already shown in Chapter 7, the z-position resolution is described by timing resolution. In following, we omit description of z-position.

The timing resolution of the barrel detectors, σ_{vetoT} , measured in real data is expressed as:

$$\sigma_{vetoT} = \sigma_{CsI} \oplus \sigma_{int} \oplus \sigma_{det}, \quad (8.12)$$

where σ_{CsI} is the resolution caused by the CsI calorimeter, σ_{int} is the resolution caused by particle interaction in the barrel detectors, and σ_{det} is the resolution coming from detector response in the barrel detectors estimated in Chapter 6. In Full MC, the resolution σ_{CsI} and σ_{int} were already included. In the mapping method, we added σ_{det} as follows.

In this method, each hit at time t_{dep} and z-position z_{dep} in the barrel detectors makes a probability density function:

$$\begin{aligned} P(t_{dep} + \Delta t, z_{dep} + \Delta z) &= \sum_{E_{dep}=0}^{\infty} \left[\text{Gaussian}(t_{dep} + \Delta t, t_{dep}, \sigma_t(E_{dep})) \right. \\ &\quad \times \text{Gaussian}(z_{dep} + \Delta z, z_{dep}, v\sigma_t(E_{dep})) \times F(E_{dep}) \left. \right] \end{aligned} \quad (8.13)$$

where $\text{Gaussian}(x, a, \sigma)$ is a gaussian function of x at mean a and width σ . The $F(E_{dep})$ is the gamma response function for incident energy E_{in} . The t_{det} and z_{det} are the detected timing and z-position in original Full MC, and we use these values to reproduce the resolution caused by particle interaction σ_{int} in Eq.(8.12). The σ_t is timing resolution, and v is propagating velocity in the detector. The Δt and Δz are the difference from the detected timing and z-position.

8.3.3 Evaluation of inefficiency in mapping method

To confirm the accuracy of the mapping method, we compared the mapping method with Full MC about the energy distribution in two decay modes in different analysis schemes.

The first mode was the $K_L \rightarrow \pi^0\pi^0\pi^0$ mode with 5-cluster event analysis. As shown in Fig. 8.5 (left), the deposit energy distribution agreed well with Full MC by including the effect of back splash. By using the back splash hit with the maximum deposit energy as a hit of an incident particle, we calculated the deposit energy distribution according to the 2-particle-incident formula shown in Eq. (8.10). The total response function is calculated from the energy deposit in the 6th gamma and back splash as:

$$F_{total}(E_{dep}) = I_{6th}F_{bksp} + F_{6th}I_{bksp} + F_{6th}F_{bksp}. \quad (8.14)$$

The response function for back splash F_{bksp} was defined for each number of clusters in the CsI calorimeter because the number of clusters was closely related to the number and energy of backsplash. The defined function F_{bksp} does not depend on the incident energy and angle of gamma hitting the CsI calorimeter. Sometimes there were multiple back splash hits, but the function F_{bksp} was defined by using the largest energy deposit in one module. The probability that backsplash is not observed, that is integration of the response function, is shown in Fig. 8.5 (right).

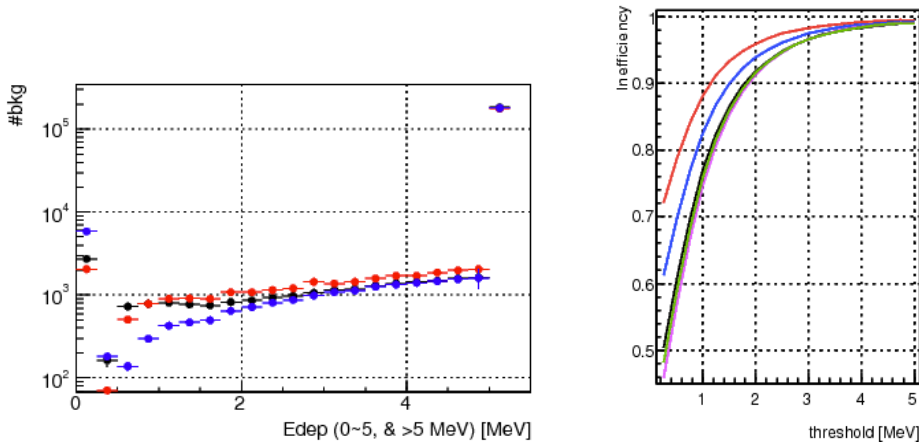


Figure 8.5: Left: The deposit energy distribution in the Main Barrel estimated with loose kinematic cuts. Red points show the result of Full MC. Blue points show the mapping method result assuming that only the 6th gamma hit the Main Barrel. Black points show the mapping method result assuming not only 6th gamma but also back splash of 5 gammas in the calorimeter hit the Main Barrel. Right: The probability of not observing backsplash in the Main Barrel when 2 (red), 4 (black), and 6 (magenta) gammas entered the calorimeter from the $K_L \rightarrow \pi^0\nu\bar{\nu}$, $K_L \rightarrow \pi^0\pi^0$ and $K_L \rightarrow \pi^0\pi^0\pi^0$ modes, respectively. Inefficiency thus includes events which do not have backsplash particle hitting the Main Barrel. In addition, 3 (blue) (5 (green)) gamma incident in the calorimeter was approximated as the mean of 2 and 4 (4 and 6) gamma incidence.

The following background analysis also uses this correction of the deposit energy distribution caused by back-splash.

The second mode was the $K_L \rightarrow \pi^0\pi^0$ decay mode with a set of loose cut conditions. This cut set applied only the cut on the hit region on the calorimeter called fiducial cut, and the cut on z-vertex position to obtain large statistics. The energy deposit caused by the combination of back-splash and one (two) decay gamma(s) hitting the Main Barrel

was defined as a function for energy deposit distribution as expressed in Eq. (8.10) (Eq. (8.11)).

The calculated energy deposit distributions in limited hit z-position regions are shown in Fig. 8.6. At most z , Full MC and the mapping method agreed. On the other hand,

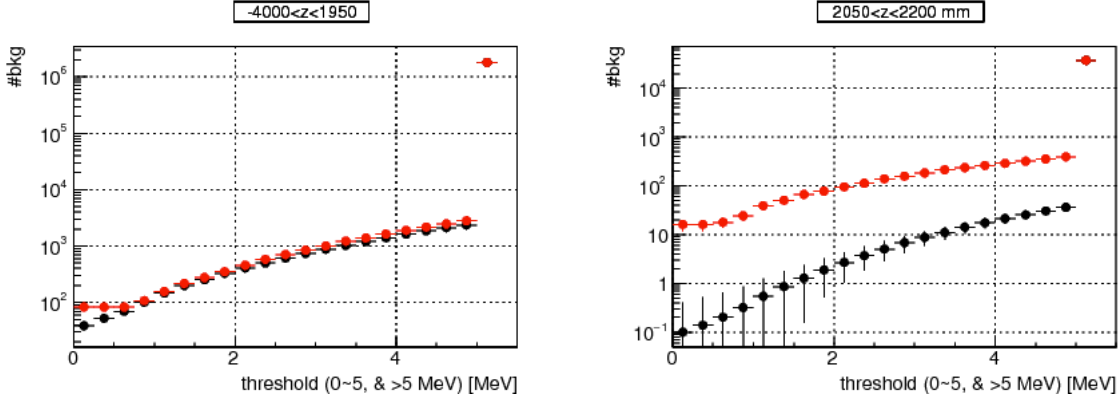


Figure 8.6: The number of the $K_L \rightarrow \pi^0\pi^0$ background events as a function of threshold at limited hitting z-position $-4000 < z < 1800$ (left) and $2050 < z < 2200$ mm (right) with loose cuts (only fiducial and z-vertex position cuts). The position of the center of the Main Barrel is $z = 0$, and that of the surface of the CsI calorimeter is $z = 2048$ mm. The numbers of background events were estimated by mapping method (black) and Full MC (red).

there was a discrepancy for deposit energy in the Main Barrel around the CsI edge. It was the effect of other detectors and dead materials of support structures sharing a gamma shower. The response function of gamma hitting the CsI edge region had a large radial position dependence. If we estimate the deposit energy distribution of this region with the mapping method, we need to prepare minute parameterization in the response function with an additional parameter such as hitting radius. In the following estimation, we thus used Full MC instead of mapping method for the CsI edge region.

8.4 $K_L \rightarrow \pi^0\pi^0$ background

The $K_L \rightarrow \pi^0\pi^0$ mode was the major background caused by the barrel detectors. We regard only this decay mode as the background in significance estimation.

In this $K_L \rightarrow \pi^0\pi^0$ background study, we tried the mapping method except for the CsI edge region.

8.4.1 Timing, z position distribution

We separated the region for two different methods, the mapping method and Full MC, depending on the trajectory of gamma. We traced the trajectory to the CsI surface and the Main Barrel surface, and calculated its distance R_{CsI} from the center on the CsI and z-position z_{MB} on the Main Barrel.

Before the Inner Barrel was installed, if the trajectory satisfied the condition $R_{CsI} > 850$ mm and $z_{MB} > 6100$, the trajectory was recognized that it passed the CsI edge

region. After the Inner Barrel was installed, the condition was changed to $R_{CsI} > 850$ mm and $z_{MB} > 5600$ mm. We defined this region large enough to cover the events affected by other detectors and structures around the CsI edge.

Events except those hitting the CsI edge region were estimated in the mapping method by applying all the kinematic cuts. Timing and z-position distributions of those events are shown in Fig. 8.7. These distribution are made by summing up of the probability density function for each event expressed in Eq. (8.13).

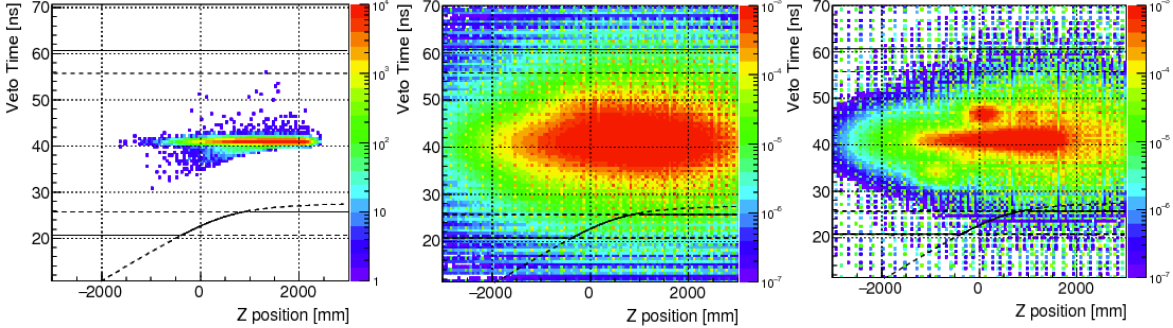


Figure 8.7: Timing and z-position distribution of the $K_L \rightarrow \pi^0 \pi^0$ decay mode generated in original full simulation (left), and events hitting the region excluding CsI edge region after applying energy deposit probability, and timing and z position resolution based on the mapping method for the Main Barrel (middle) and the middle-stream Barrel detectors (right). The x-axis is defined as $z = 0$ to be the center of the Main Barrel. The events in the left plot were generated with the number of K_L decays which would give a signal S.E.S of 5.2×10^{-11} . The region between a solid black line and a solid black curve shows an example of veto window.

For the CsI edge region, the timing and hit position distributions and the number of background events were estimated with Full MC. We increased the statistics by reusing the tracks of decay particles generated in Full MC and recreating a gamma shower every time. Timing and z-position distributions after applying all the cuts are shown in Fig. 8.8. The timing and z-position of each hit was smeared according to the energy deposit.

These figures also show an example of veto window. Decision on the borders of the veto window is described in the following.

8.4.2 Vertex mis-reconstruction

As shown in the timing and z-position distribution, there were earlier timing events in relatively upstream side of the barrel detectors around $t < 38$ ns and $z < 800$ mm. These events were caused by mis-reconstruction of the K_L decay vertex. If the energy of a gamma was mis-measured low, the decay vertex was mis-reconstructed downstream of real vertex position. In this case, the path of the particles hitting the barrel detectors was mis-calculated, and the reconstructed timing of the particles hitting relatively upstream side became earlier.

As understood from Eq.(7.15), the true veto timing t_{tr} is expressed as the constant timing $t_{tr} = t_0$. The largest timing difference between the true veto timing and the

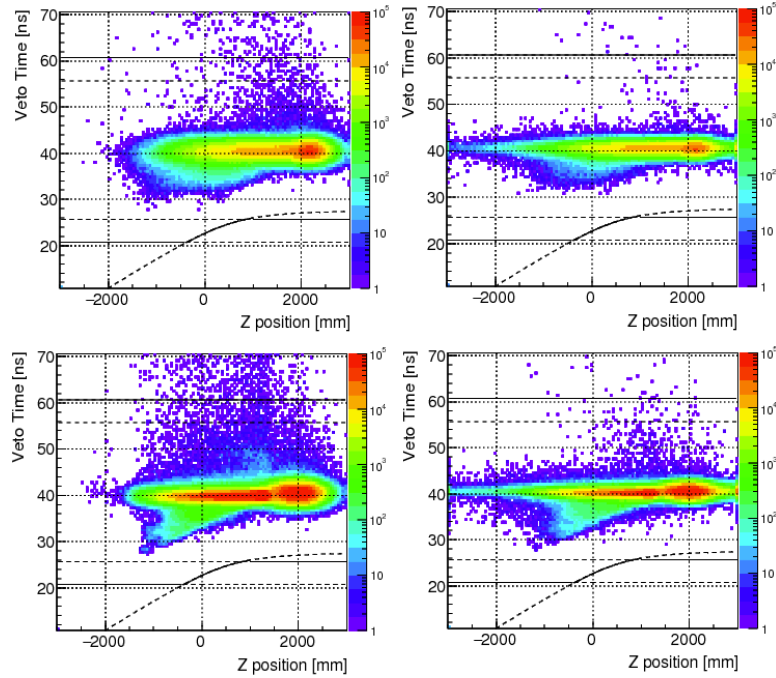


Figure 8.8: Timing and z-position distribution of the $K_L \rightarrow \pi^0\pi^0$ events which have gammas hitting the CsI edge region. Top two figures show the case with the Main Barrel, and the bottom two figures show the case with the middle-stream Barrel detectors. The plots on the left show hits with the maximum energy, and the plots on the right show the hits with the timing nearest to the veto timing. The number of generated events for the middle-stream Barrel detectors was 3.8 times that of the Main Barrel. Distributions were created by recycling original full simulation events 100 times, which was equivalent to generating the number of the K_L that would give S.E.S = 5.2×10^{-13} for the signal. The $z = 0$ in these plots corresponds to the center of the Main Barrel. The region between a solid black line and a solid black curve shows an example of veto window.

reconstructed timing t_{rec} occur if a gamma hits the barrel detectors perpendicularly as shown in Fig. 8.9. In this case, the timing difference is calculated as:

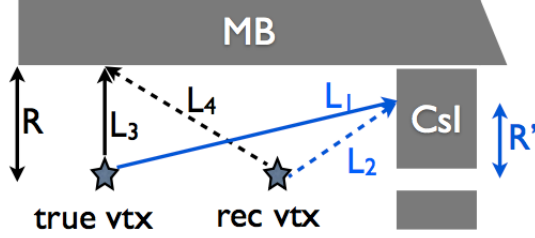


Figure 8.9: The fastest limit of the mis-reconstructed timing is shown at the largest difference of the length L_3 and L_4 . If the CsI calorimeter mis-measures the gamma energy lower, the vertex is reconstructed downstream rather than the true vertex.

$$t_{rec} - t_{tr} = \frac{1}{c} \{ (L_2 - L_1) - (L_4 - L_3) \}, \quad (8.15)$$

$$t_{rec} \gtrsim t_0 + \frac{1}{c} \{ z_{diff} - \sqrt{z_{diff}^2 + R^2} + R \}, \quad (8.16)$$

where the z_{diff} is the z-position difference between the reconstructed vertex and the true vertex. The geometrical limitation is thus expressed as:

$$t(z) = t_0 - \Delta t + \frac{1}{c} \{ (z - \Delta z) - \sqrt{(z - \Delta z)^2 + R^2} + R \}, \quad (8.17)$$

where Δz and Δt is the offset assuming the resolution. The curve shown in Fig. 8.7 and Fig. 8.8 set $(\Delta z, \Delta t) = (500, 16)$. Although the following study on veto window is independent of z-position, the window inside $t(z)$ limit is effective under the condition of high accidental rate such as May 2013 run.

8.4.3 Late shower events

As also shown in the timing and z-position distribution in Fig. 8.8, there were events with more than 10 ns later than the veto timing. These events were caused by photo-nuclear interactions. A typical event display is shown in Fig 8.10. Most events have a lower energy deposit at an earlier timing in other modules. When we use such modules for vetoing, the veto timing spread is reduced as shown in Fig. 8.8 (right).

8.4.4 Veto window dependence

By combining two estimations of the t-z distribution in the CsI edge region and the region calculated with the mapping method, the number of the $K_L \rightarrow \pi^0 \pi^0$ background events was calculated as a function of veto width. The veto width dependence is shown in Fig. 8.11. Hits closest to the veto timing with the energy higher than the energy threshed was used. The number of the $K_L \rightarrow \pi^0 \pi^0$ background events rapidly decrease by detecting events creating shower on veto timing for veto width < 30 ns, and slowly decrease by detecting late shower events for veto width > 30 ns. Background events around 30 ns were mainly caused by vertex mis-reconstruction.

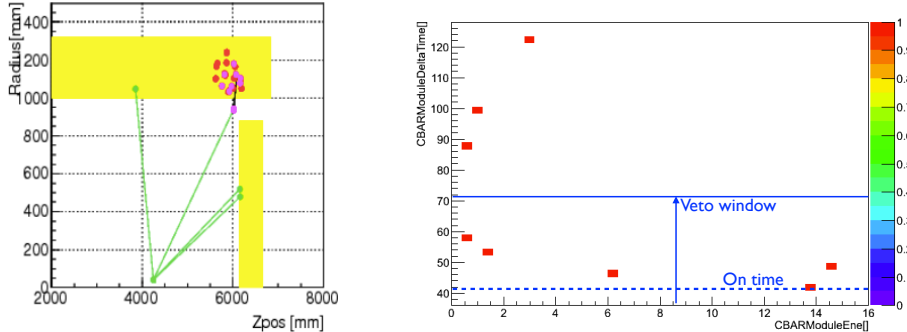


Figure 8.10: Event display (left) and deposit energy and timing of the Main Barrel (right) for a $K_L \rightarrow \pi^0\pi^0$ event which created a late shower. Another module has an energy deposit near the veto timing.

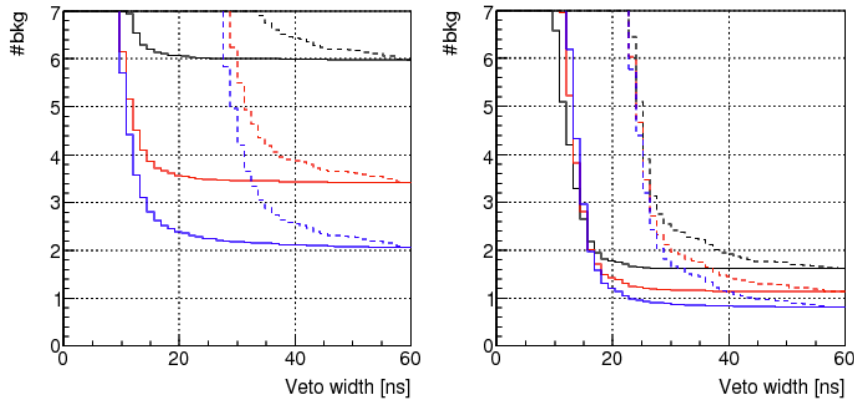


Figure 8.11: The number of the $K_L \rightarrow \pi^0\pi^0$ background events is shown as a function of the veto window width for the Main Barrel (left) and the middle-stream Barrel detectors (right). Each line shows the events with the energy threshold 2 MeV (black), 1 MeV (red), and 0.5 MeV (blue). Veto window was moved for all events (dashed line) and for only < 5 MeV deposit events (solid line). The veto window for > 5 MeV deposit events in solid line was fixed at 60 ns width to detect late shower events caused by photo-nuclear interaction.

8.5 S/B ratio related with back splash loss

As described in Chapter 4 and Section 8.1, back splash on the Main Barrel caused a 28 % signal loss. In this section, we discuss a veto window to maximize S/B between the $K_L \rightarrow \pi^0 \nu \bar{\nu}$ signal and the $K_L \rightarrow \pi^0 \pi^0$ background by recovering acceptance loss due to back-splash without increasing backgrounds.

Both the $K_L \rightarrow \pi^0 \nu \bar{\nu}$ and the $K_L \rightarrow \pi^0 \pi^0$ modes were estimated without overlaying accidental events in the previous sections. In this section, we will compare the timing and z-position distribution between back splash and $K_L \rightarrow \pi^0 \pi^0$ background without accidental overlay.

A figure of merit as a ratio of the number of signal events with back-splash and the $K_L \rightarrow \pi^0 \pi^0$ background is shown in Fig. 8.12. There is only small z-position dependence

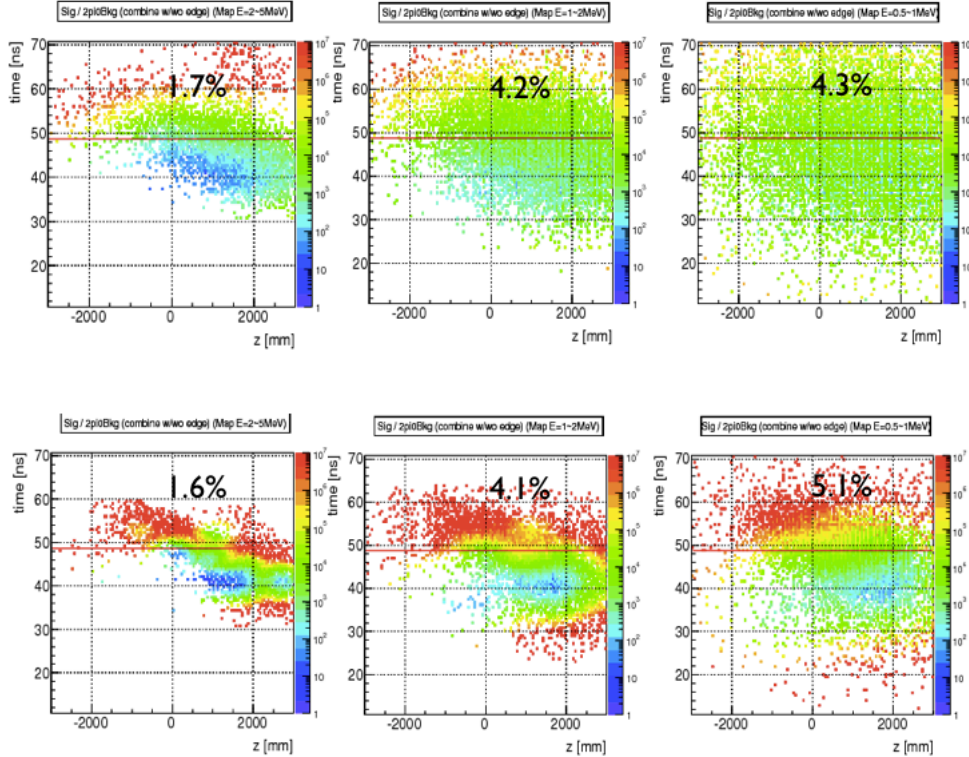


Figure 8.12: A S/B ratio but scaled with 5×10^7 over S/B for 100×100 bins plotting points based on the signal shown in Fig. 8.1 and the background events shown in Fig. 8.7 and Fig. 8.8. The z-axis thus gives better S/B with the value $> 5 \times 10^3$ for each point. Upper three figures show the case of the Main Barrel, and lower three figures show the case of the middle-stream Barrel detectors for subdivided energy deposits $2 < E_{dep} < 5$ MeV (left), $1 < E_{dep} < 2$ MeV (center) and $0.5 < E_{dep} < 1$ MeV (right). The number drawn in the plots are the recovered signal ratio if the narrower “on time +8 ns” veto window (red line) is applied. The recoveries are 10.2 % for the Main Barrel, and 10.8 % for the Inner Barrel.

for all energy region. We thus consider a veto window only in time, and no dependence in z-position. By selecting “on time +8 ns” timing window, both before and after the

Inner Barrel installation show the same 10 % recovery from the 28 % loss in original detector condition. With the Inner Barrel, we can select a narrower veto window “on time +6 ns”, and recover the loss by 16 %.

8.6 Decision on veto window and threshold and estimation of significance

In this section we include the effect of accidentals. The number of both $K_L \rightarrow \pi^0 \nu \bar{\nu}$ signal and $K_L \rightarrow \pi^0 \pi^0$ background events without beam accidental loss are scaled with the function expressed in Eq. (8.6).

We defined a figure of merit as a significance S/\sqrt{B} , where S is the number of observed $K_L \rightarrow \pi^0 \nu \bar{\nu}$ events and B is the number of the $K_L \rightarrow \pi^0 \pi^0$ background events.

The significance before and after the Inner Barrel installation is shown in Figure 8.13. The maximum significance was obtained with a 60-ns-wide veto window for $E_{dep} > 5$

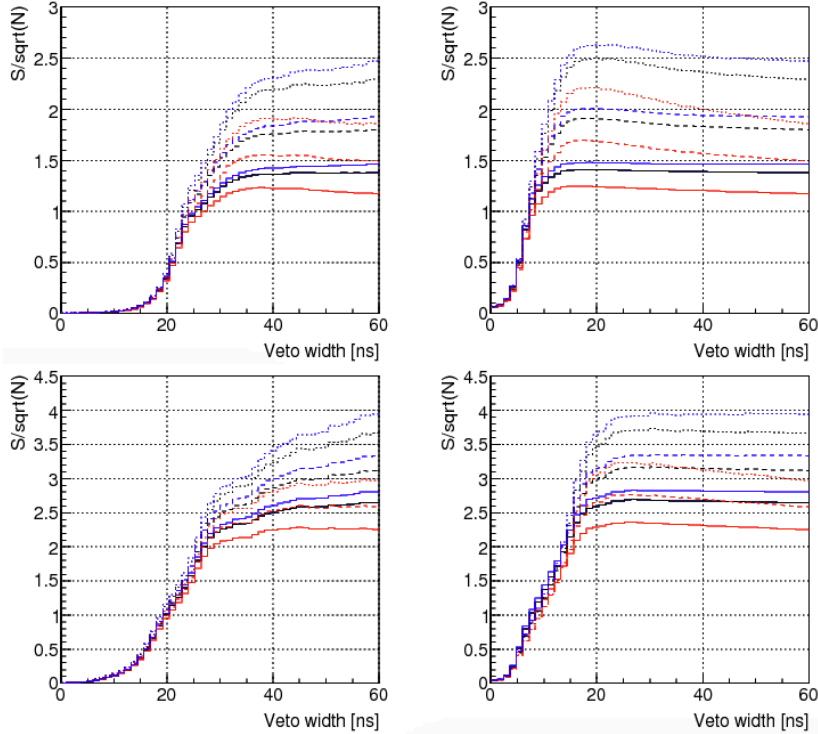


Figure 8.13: The significance S/\sqrt{B} as a function of the veto window for all events with the Main Barrel (top left) and with the middle-stream Barrel detectors (bottom left), and the fixed ± 30 ns veto window for > 5 MeV deposit events and the changed veto window for other events about the Main Barrel (top right) and the middle-stream Barrel detectors (bottom right). Each color shows the beam condition: 24 kW 6 seconds cycle (blue), 100 kW 4 seconds cycle (black), and assuming a 3 times higher accidental event rate at 100 kW 4 seconds cycle (red). The line styles represent the veto energy threshold: 2 MeV (solid line), 1 MeV (dashed line), and 0.5 MeV (dotted line).

MeV deposit hits and 20-ns-wide for $5 > E_{dep} > 0.5$ MeV hits. This veto window and threshold utilize the difference between the energy distributions of accidental hits and background events. Most of beam accidental hits and back-splash hits deposit low energy ($E_{dep} < 5$ MeV), whereas, most of the $K_L \rightarrow \pi^0\pi^0$ background events deposit > 5 MeV in broad timing.

The highest significance for the expected future beam structure was 2.5 without the Inner Barrel, and 3.7 with the Inner Barrel.

Chapter 9

Discussion

9.1 Improvement of sensitivity

We evaluated the significance S/\sqrt{B} against the $K_L \rightarrow \pi^0\pi^0$ background in Chapter 8. In this section, we consider the 3σ sensitivity by including other backgrounds. We discuss the sensitivity to observe the signal events as a function of the amount of collected data. In the following, we assume 100 kW and 4 second cycle beam. We also assume that neutron background expected in May 2013 run will be rejected by several cuts with a 50 % acceptance reduction.

We compare the sensitivity for two cases: with and without the Inner Barrel. First, the number of signal and $K_L \rightarrow \pi^0\pi^0$ background events estimated in previous chapter were used. With the final amount of data, the expected number of Standard Model signal events is $S = 3.5$, and the number of $K_L \rightarrow \pi^0\pi^0$ background events is $B_{\pi^0\pi^0} = 3.0$ without the Inner Barrel. In case with the Inner Barrel, the number of the $K_L \rightarrow \pi^0\pi^0$ background events became $B_{\pi^0\pi^0} = 0.8$. Next, the number of other K_L background events was calculated from the estimation of the final detector configuration but without the Inner Barrel [37]. From the K_L background except the $K_L \rightarrow \pi^0\pi^0$ background events (2.75 ± 0.31) normalized with the number of signal events (6.50 ± 0.05), the number of other K_L background events is calculated as $B_{K_{LO}} = 1.5$.

The above number of signal and background events are scaled with the amount of collected data. The $K_L \rightarrow \pi^0\nu\bar{\nu}$ observation with the 3σ evidence is distinguished by the expectation P as:

$$P = \sum_{i=n}^{\infty} \text{Poisson}(i, \alpha(B_{K_{LO}} + B_{\pi^0\pi^0})) \quad (9.1)$$

$$< 2.7 \times 10^{-3}, \quad (9.2)$$

where n is the number of observed events, and α is a scale factor for the amount of collected data expressed in the fraction of final amount of data. If we replace the number of expected background events $B_{K_{LO}} + B_{\pi^0\pi^0}$ in Eq.(9.3) with that of the total number of expected events $S + B_{K_{LO}} + B_{\pi^0\pi^0}$, we can evaluate the sensitivity to observe a New Physics with the 3σ evidence. The branching ratio that we can claim the 3σ evidence is:

$$BR = (n - \alpha N_{exp}) \times S.E.S. \quad (9.3)$$

where N_{exp} is the number of the expected events with the final amount of data: $N_{exp} = B_{K_L O} + B_{\pi^0 \pi^0}$ for the Standard Model, and $N_{exp} = S + B_{K_L O} + B_{\pi^0 \pi^0}$ for New Physics.

The sensitivity with and without the Inner Barrel installation is shown in Fig. 9.1. The Inner Barrel improves the sensitivity by 10 % for > 0.2 times the total amount of

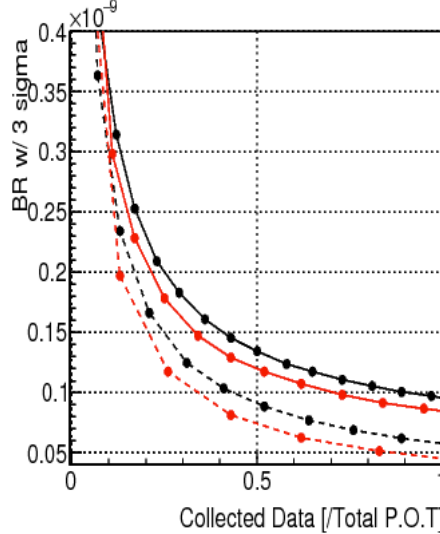


Figure 9.1: The branching ratio sensitive to a New Physics with 3σ evidence (solid line) and the $K_L \rightarrow \pi^0 \nu \bar{\nu}$ observation in the Standard Model branching ratio with 3σ evidence (dashed line) without the Inner Barrel (red) and with the Inner Barrel (black). Each point shows the branching ratio at a scale factor α satisfying the expectation $P = 2.7 \times 10^3$ for each observed number of events n in Eq. (9.2).

data.

9.2 Advices for module production in further

We finished the construction of all the Inner Barrel modules, and installed the detector inside the Main Barrel in April 2016.

We experienced several problems during construction.

After glueing fibers on the scintillator, cracks grew in the scintillator, and un-cured glue was remaining in the groove. This phenomena did not occur in the stage of the prototype production. From several features of the cracks and the difference between the prototype and mass production, we suspected that the cracks were caused by the reaction between un-cured glue and the extrusion-molding scintillator.

Most of the cracks existed near the edge of the scintillator and other cracks existed randomly. At the edge of the scintillator, plastic tubes made of PEEK resin were glued in the grooves to protect fibers. We carved the grooves to insert the tube, and the surface of the grooves was rough. The groove surface in other region was not as smooth as the surface of the prototype due to the difference in machining process. We found small holes in the grooves of the mass production. The largest difference was the kind of the scintillator between extrusion-molding scintillator for the mass production and casting

scintillator for the prototype.

On the other hand, we did not find any fibers damaged by un-cured glue. About the fibers, the difference from the prototype production was only that we found partially thick fibers in the mass production process.

An assumption that the cracks were caused by a reaction between un-cured glue and the extrusion-molding scintillator is supported by the followings. The edge position tended to leave un-cured glue because UV light cannot penetrate to behind the PEEK tube. Other positions sometimes left un-cured glue due to partially thick fibers or holes in the scintillator.

Finally, by the effort of Prof. Togawa and other people, cracks stopped growing after annealing the scintillator and placing the scintillator in vacuum after glueing.

If we construct a similar detector in future, we should consider using casting scintillator. For the Inner Barrel, we selected extrusion-molding method to make long scintillators at low cost. However, scintillator are supported by the Back Plate and the Front Plate, so structure-wise, a few short scintillators should work. In addition, with casting scintillators, the light yield can be 30 ~ 40 % higher.

Chapter 10

Conclusion

We developed the Inner Barrel to improve the overall gamma veto efficiency to suppress the major $K_L \rightarrow \pi^0\pi^0$ background. We also aimed at obtaining a good timing resolution by the Inner Barrel to recover acceptance loss due to back-splash hits and beam accidental hits. To realize the Inner Barrel, we studied the performance and the structure of the detector based on Geant4 MC and mechanical calculations. As a result, we decided to construct 5- X_0 sampling detector made of lead and scintillator. The signal is read out by WLS fiber with a shorter decay time than that for the Main Barrel, and 500-MHz FADCs.

We also studied the Main Barrel because the performance of the Main Barrel was not proven enough. We evaluated the timing resolution for both the Inner Barrel and the Main Barrel, and improved analysis methods to reduce the acceptance loss caused by beam accidental hits and back-splash hits. By including this timing resolution in the MC for the Main Barrel, the timing distribution of data and MC agreed well.

By installing the Inner Barrel and improving the analysis for both the Inner Barrel and the Main Barrel, the $K_L \rightarrow \pi^0\pi^0$ background was estimated to be suppressed by a factor of three, and the total number of background events was estimated to be reduced to less than the number of signal events predicted by the Standard Model.

Appendix A

Cut conditions

A.1 Cut conditions for 5 gamma analysis

Kinematic cuts for selecting 5-gamma event are listed as follows.

Shape χ^2 : The value evaluating the cluster shape whether it is created by a gamma or not [46]. This selection rejects multiple gamma fusion and hadronic incident particles.

$Z_{vtx}^{K_L}$: The K_L decay vertex defined from Eq. (7.13).

$\Delta Z_{vtx}^{\pi^0}$: Difference of z-vertex between the first π^0 and the second π^0 .

ΔK_L Mass: Difference between the nominal K_L mass and reconstructed K_L mass.

$\Delta \pi^0$ Mass: Difference between the nominal π^0 mass and the first (second) π^0 mass.

$\Delta \pi_{3rd}^0$ Mass: Difference between the nominal π^0 mass and the third π^0 mass at minimum χ_{Rec}^2 .

$Z_{vtx}^{K_L} \chi^2$: The minimum χ^2 of the decay vertex defined in Eq. (7.14).

Second $Z_{vtx}^{K_L} \chi^2$: Difference of the first to second minimum χ^2 of the decay vertex as $\chi_{2nd}^2 - \chi_{1st}^2$. The first (second) minimum χ^2 is defined in Eq. (7.14). This cut is to ensure the gamma pairs at the minimum χ^2 is the best combination.

K_L Mass χ^2 : The minimum χ^2 of the K_L mass defined in Eq. (7.21).

Second K_L Mass χ^2 : Difference of the first to second minimum χ^2 of the K_L mass as $\chi_{2nd}^2 - \chi_{1st}^2$. The first (second) minimum χ^2 is defined in Eq. (7.21). This cut is to ensure the gamma pairs at the minimum χ^2 is the best combination.

γ_{6th} hit Z: Reconstructed hit z-position on the Main Barrel defined in Eq. (7.23).

$\gamma_{6th} \Delta\phi$: Difference between hit and reconstructed ϕ -direction on the Main Barrel.

Cut conditions to select 5-gamma event are summarized in Table A.1.

Table A.1: Cut values for 5-gamma analysis.

Cut conditions	Cut values
E_γ	$100 < E_\gamma < 2000$ MeV
Fiducial	$x, y > 100, R < 880$ mm
Cluster distance	> 150 mm
Shape χ^2	< 10
Dead channel	> 53 mm
$Z_{vtx}^{K_L}$	$2000 < z < 5200$ mm
$\Delta Z_{vtx}^{\pi^0}$ (for 2 π^0 s)	< 100 mm
ΔK_L mass	± 15 MeV
$\Delta \pi^0$ Mass (for 2 π^0 s)	$\pm 5.125 \times 0.5$ MeV
$\Delta \pi_{3rd}^0$ Mass	± 5.125 MeV
$Z_{vtx}^{K_L} \chi^2$	< 3.0
Second $Z_{vtx}^{K_L} \chi^2$ ($\chi_{2nd}^2 - \chi_{1st}^2$)	> 0.5
K_L Mass χ^2	< 3
Second K_L Mass χ^2 ($\chi_{2nd}^2 - \chi_{1st}^2$)	> 0.5
γ_{6th} Hit Z	$2000 < z < 5800$ mm
$\gamma_{6th} \Delta\phi$	± 0.2 rad
Vetos	Standard of May2013 [44] except the Main Barrel

A.2 Cut conditions for 2 gamma analysis

$K_L P_T$: Transverse momentum of reconstructed K_L .

E_{tot} : Total energy of two gammas.

$E\theta$: The product of each gamma energy and incident angle. Perpendicular hit is defined as $\theta = 0$.

E ratio: Energy ratio of two gammas to exclude wrong pair of π^0 decay gammas.

COE: Energy weighted mean hit position called Center Of Energy.

T difference: Timing difference between two gammas.

π^0 kinetic: Correlation between P_T and the z-position of π^0 decay to reject $\eta \rightarrow \gamma\gamma$ events.

Cluster size: Number of crystals in a cluster.

Cluster RMS: Energy weighted mean square of hit radius. The radius is defined as the distance from center of energy of the cluster to i -th crystal.

Dead channel: Distance from dead channels to a crystal included in a cluster. This cut required because there were two dead channels in May 2013.

These cut conditions were the default of May 2013 analysis but without Neural Net cuts to exclude neutron cluster. Kinematic cuts and veto conditions summarized in Table A.2.

Table A.2: Cut values for signal mode.

Cut conditions	Cut values
E_γ	$100 < E_\gamma < 2000$ MeV
Fiducial	$x, y > 130, R < 850$ mm
Cluster distance	> 300 mm
Shape χ^2	< 4.6
Dead channel	> 53 mm
$Z_{vtx}^{K_L}$	$3000 < z < 5000$ mm
$K_L P_T$	$130 < P_T < 125$ MeV
E_{tot}	> 650 MeV
$E\theta$	> 2500 MeV deg
E ratio	> 0.2
COE	> 200 mm
T difference	< 2 ns
π^0 kinetic	default
Cluster size	> 4
Cluster RMS	> 10 mm
Vetos	Standard of May2013 [44] except the Main Barrel

Bibliography

- [1] J.H. Christenson *et al.*, Phys. Rev. Lett. **13**, 138 (1964).
- [2] M. Kobayashi and T. Maskawa, Prog. Theor. Phys. **49**, 652 (1973).
- [3] L. Wolfenstein, Phys. Rev. Lett. **51**, 1945 (1983).
- [4] G. Buchalla and A. J. Buras, Phys. Rev. D **54**, 6782 (1996).
- [5] T. Inami and C. S. Lim, Prog. Theor. Phys. **65**, 297 (1981).
- [6] J. Brod, M. Gorbahn, and E. Stamou, Phys. Rev. D **83**, 034030 (2011).
- [7] Y. Grossman and Y. Nir, Phys. Lett. B, **398**, 163 (1997).
- [8] A. V. Artamonov *et al.*, Phys. Rev. D **79**, 092004 (2009).
- [9] D. M. Straub, in Proceedings of the 6th International Workshop on the CKM Unitarity Triangle, UK, 2010, edited by Tim Gershon, eConf C100906, (2010), arXiv:1012.3893 [hep-ph].
- [10] K. Shiomi, PhD thesis, Kyoto University, (2012).
- [11] T. Masuda, PhD thesis, Kyoto University, (2014).
- [12] L. S. Littenberg, Phys. Rev. D **39**, 3322 (1989).
- [13] A. Alavi-Harati *et al.*, Phys. Rev. D **61**, 072006 (2000).
- [14] J. K. Ahn *et al.*, Phys. Rev. D **81**, 072004 (2010).
- [15] J-PARC E14 Collaboration, *Technical Design Report of KL Beamline at the J-PARC Hadron Hall*, (2009).
- [16] K. Shiomi *et al.*, Nucl. Instrum. Meth. A **664**, 264 (2012).
- [17] S. Ajimura *et al.*, Nucl. Instrum. Meth. A **552**, 263 (2005).
- [18] Chinese Physics C, **38**, 9 (2014) 090001.
- [19] D. Naito *et al.*, Prog. Theor. Exp. Phys. **2016**, 023C01 (2016).
- [20] S. Nagamiya, Prog. Theor. Exp. Phys. **2012**, 02B001 (2012).
- [21] T. Shimogawa, Nucl. Instrum. Meth. A **623**, 585 (2010).

- [22] Y. Tajima *et al.*, Nucl. Instrum. Meth. A **592**, 261 (2008).
- [23] Y. Maeda *et al.*, Prog. Theor. Exp. Phys. 2015, 063H01(2015).
- [24] T. Matsumura *et al.*, Nucl. Instrum. Methods A795, 19-31 (2015)
- [25] T. Inagaki *et al.*, High energy news (2004).
- [26] Y. Yoshimura *et al.*, KEK E391a Technote TN157, 2004.
- [27] Ciai Kogyo, Manufacturing inspection report, 5th May 2000.
- [28] Kuraray Co., Ltd. <http://www.kuraray.co.jp>.
- [29] M. Itaya *et al.*, Nucl. Instrum. Meth. A **522**, 477 (2004).
- [30] Hamamatsu Photonics K.K. <http://jp.hamamatsu.com>.
- [31] Y. Sugiyama, *et al.*, Nucl. Sci., 62, 1115-1121 (2015).
- [32] E. Iwai *et al.*, Nucl. Instrum. Meth. A **786**, 135 (2015).
- [33] D. Wright *et al.*, Nucl. Instrum. Meth. A **804**, 21 (2015).
- [34] N. Bianchi *et al.*, Phys. Rev. C **54**, 1688 (1996).
- [35] Leo, “Techniques for Nuclear and Particle Physics Experiments”, Springer-Verlag.
- [36] F. Mescia and C. Smith, <http://www.lng.infn.it/wg/vus/content/Krare.html>.
- [37] E. Iwai. PhD thesis, Osaka University, 10 2012.
- [38] V. Brekhovskih *et al.*, The WLSF Fiber Properties Study (2000), <http://cds.cern.ch/record/ 691514>.
- [39] Bicrons, Saint-Gobain Ceramics Plastics, Inc. <http://www.detectors.saint-gobain.com>.
- [40] ELJEN Technology, Plastic Scintillators, http://www.eljentechnology.com/index.php?option=com_content&view=article&id=47&Itemid=34
- [41] Norland Products Inc. <http://www.norlandprod.com>.
- [42] Y. Yanagida, Master thesis, Osaka University (2012).
- [43] T. Toyoda, Master thesis, Osaka University (2014).
- [44] Y. Maeda, PhD thesis, Kyoto University, (2016).
- [45] T. Masuda, Collaboration meeting 22nd Feb. 2013.
- [46] K. Sato, PhD thesis, Osaka University, 1 2015
- [47] T. Masuda *et al.*, Prog. Theor. Exp. Phys. **2016**, 013C03 (2016).

- [48] H. Hotchi, HINT2016, December 5-8 2016 at J-PARC, “Recent progress and future prospect of J-PARC accelerator”, <https://kds.kek.jp/indico/event/22193/other-view?view=standard>.
- [49] Andrzej *et al.*, JHEP **11**, (2015) 033.
- [50] arXiv:nucl-th/0306008v1. ?? CHEP 2003, La Jolla, California, USA, March 24-28 2003.
- [51] Saint-Gobain Crystals, Scintillation Products Scintillating Optical Fiber, <http://www.crystals.saint-gobain.com/uploadedFiles/SG-Crystals/Documents/SGC%20Fibers%20Brochure.pdf>.